



**CALIFORNIA
ENERGY COMMISSION**



Energy Research and Development Division

PROJECT REPORT

Performance-Based Earthquake Engineering Assessment Tool for Natural Gas Storage and Pipeline Systems

Task 4E Final Report – Sensory and Monitoring Technologies

**Gavin Newsom, Governor
July 2022**



PREPARED BY:

Primary Authors:

Chien-Chih Wang
Peter Hubbard
Tianchen Xu
Kenichi Soga

UC Berkeley
760 Davis Hall, Berkeley, CA 94720
(510) 642-3261
<https://ce.berkeley.edu>

Contract Number: PIR-18-003

PREPARED FOR:

California Energy Commission

Yahui Yang

Project Manager

Laurie ten Hope

Deputy Director

ENERGY RESEARCH AND DEVELOPMENT DIVISION

Drew Bohan

Executive Director

DISCLAIMER

This report was prepared as the result of work sponsored by the California Energy Commission. It does not necessarily represent the views of the Energy Commission, its employees or the State of California. The Energy Commission, the State of California, its employees, contractors and subcontractors make no warranty, express or implied, and assume no legal liability for the information in this report; nor does any party represent that the uses of this information will not infringe upon privately owned rights. This report has not been approved or disapproved by the California Energy Commission nor has the California Energy Commission passed upon the accuracy or adequacy of the information in this report.

ACKNOWLEDGEMENTS

This research study was funded by the California Energy Commission, under Contract No. PIR 18-003. The opinions, findings, conclusions, and recommendations expressed in this publication are those of the authors and do not necessarily reflect the view of California Energy Commission and its employees, the State of California, the Pacific Earthquake Engineering Research (PEER) Center, and the Regents of the University of California.

We would like to acknowledge the California Energy Commission (CEC) for funding this project. Prof. Jonathan Bray of University of California Berkeley is the PI of the project, whereas Yahui Yang is the CEC coordinator. Dr. Jennie Watson-Lamprey, Micaela Largent and Dr. Barry Zheng of Slate Geotechnical Consultants helped us organize our collaborations with different Task teams. These included Task 4b members (Prof. Jon Bray, Chris Bain, Dr. Daniel Hutabarat, Prof. Tom O'Rourke, and Scott Lindvall), Task 4c members (Dr. Jonny Rutqvist, Dr. Keurfon Luu, Preston Jordan, Dr. Tsubasa Sasaki, Dr. William Foxall and Dr. Yingqi Zhang) and Task 4d members (Prof. Tara Hutchinson, Prof. David McCallen, Prof. Sherif Elfass, Dr. Elide Pantoli and Dr. Suiwen Wu). Dr. Amarnath Kasalanati and Dr. Arpit Nema of the Pacific Earthquake Engineering Research Center (PEER) supported the experiments described in Appendix A. Shakhzod Takhirov, Llyr Griffiths and Matt Cataleta of UC Berkeley's Civil Engineering laboratories also supported the demonstration testing. Pacific Gas and Electric Company and the East Bay Municipal Utility District donated testing samples. Dr. Linqing Luo of the Lawrence Berkeley National Laboratory provided crucial technical support.

PREFACE

The California Energy Commission's (CEC) Energy Research and Development Division manages the Natural Gas Research and Development Program, which supports energy-related research, development, and demonstration not adequately provided by competitive and regulated markets. These natural gas research investments spur innovation in energy efficiency, renewable energy and advanced clean generation, energy-related environmental protection, energy transmission and distribution and transportation.

The Energy Research and Development Division conducts this public interest natural gas-related energy research by partnering with RD&D entities, including individuals, businesses, utilities and public and private research institutions. This program promotes greater natural gas reliability, lower costs and increases safety for Californians and is focused in these areas:

- Buildings End-Use Energy Efficiency.
- Industrial, Agriculture and Water Efficiency
- Renewable Energy and Advanced Generation
- Natural Gas Infrastructure Safety and Integrity.
- Energy-Related Environmental Research
- Natural Gas-Related Transportation.

Task 4E Final Report - Smart Gas Infrastructure Sensing of Wells and Pipeline Connections Performance is an interim report for the Performance-Based Earthquake Engineering Assessment Tool for Natural Gas Storage and Pipeline Systems project conducted by University of California, Berkeley. The information from this project contributes to the Energy Research and Development Division's Natural Gas Research and Development Program.

For more information about the Energy Research and Development Division, please visit the [CEC's research website](http://www.energy.ca.gov/research/) (www.energy.ca.gov/research/) or contact the CEC at 916-327-1551.

ABSTRACT

This report is one of a series of reports documenting the methods and findings of a multi-year, multi-disciplinary project conducted by the Pacific Earthquake Engineering Research Center (PEER) with the Lawrence Berkeley National Laboratory (LBNL), and funded by the California Energy Commission (CEC). The overall project is titled “Performance-based Earthquake Engineering Assessment Tool for Natural Gas Storage and Pipeline Systems” henceforth referred to as the “*OpenSRA* Project.”

The overall goal of the *OpenSRA* project is to create an open-source research-based seismic risk assessment tool for natural gas infrastructure that can be used by utility stakeholders to understand better state-wide risks, prioritize mitigation, plan new gas infrastructure, and help focus post-earthquake repair work.

The project team includes researchers from LBNL, UC Berkeley, UC San Diego, University of Nevada Reno, the NHERI SimCenter at UC Berkeley, and Slate Geotechnical Consultants and its subcontractors Lettis Consultants International (LCI) and T.D. O’Rourke of Cornell University. Focused research to advance the seismic risk assessment tool was conducted by Task Groups, each addressing a particular area of study and expertise, and collaborating with the other Task Groups.

This report is the product of Task Group E: Smart gas infrastructure sensing of wells and pipeline connections performance. The scope of this report is a guide to natural gas infrastructure owners on the latest monitoring technologies in the context of the model variables that *OpenSRA* will use to make its assessment of natural gas infrastructure in California subject to seismic hazards.

The adoption of new technologies has been slowed by up-front costs and operational changes resulting from implementation. Monitoring technologies have also changed rapidly, making it challenging to adapt to the opportunities of new technologies. Data and operational information from sensors, however, can be leveraged to inform the models, such as *OpenSRA*. Assessment tools for natural gas storage and pipeline systems both reduce uncertainty and verify predictions.

Keywords: Sensor systems, Remote Sensing, Distributed Fiber Optic Sensors (DFOS), Wireless Sensor Network (WSN), In-line Inspection (ILI), Leak Detection

Please use the following citation for this report:

Wang, Chien-Chih; Peter Hubbard; Tianchen Xu; Kenichi Soga. 2022. *Performance-Based Earthquake Engineering Assessment Tool for Natural Gas Storage and Pipeline Systems, Task 4E Final Report – Sensor and Monitoring Technologies*. California Energy Commission. July 2022.

TABLE OF CONTENTS

Page

| | |
|---|------|
| ACKNOWLEDGEMENTS | iii |
| PREFACE | iv |
| ABSTRACT | v |
| TABLE OF CONTENTS | vi |
| LIST OF FIGURES | viii |
| LIST OF TABLES | xii |
| EXECUTIVE SUMMARY | 1 |
| Introduction | 1 |
| Project Purpose | 2 |
| Project Approach | 2 |
| Project Results | 3 |
| CHAPTER 1: Introduction | 4 |
| Background | 5 |
| Outcomes | 6 |
| CHAPTER 2: Project Approach | 7 |
| Sensing Technology Categories | 7 |
| Remote Sensing Technologies | 7 |
| Continuous Monitoring Technologies | 7 |
| In-line Inspection Technologies | 8 |
| Leakage Detection Technologies | 8 |
| OpenSRA Informing Technologies Guidance | 8 |
| Gas Pipelines | 9 |
| Gas Storage Wells | 12 |
| Gas Facilities | 13 |
| CHAPTER 3: Project Results | 17 |
| Remote Sensing Technologies | 17 |
| Introduction to Remote Sensing Technologies | 17 |
| Light Detection and Ranging | 21 |

| | |
|---|------|
| Interferometric Synthetic Aperture Radar | 24 |
| Structure from Motion..... | 27 |
| Continuous Monitoring Technologies | 32 |
| Distributed Fiber Optic Sensors..... | 32 |
| Wireless Sensor Networks | 45 |
| In-line Inspection Technologies | 65 |
| Introduction to Inspection Technologies..... | 65 |
| Smart PIG | 65 |
| Magnetic Flux Leakage..... | 68 |
| Ultrasonic Testing..... | 75 |
| Leakage Detection Technologies..... | 84 |
| Gas Sensing Technologies | 84 |
| Flow Monitoring Technologies..... | 87 |
| CHAPTER 4: Conclusions..... | 97 |
| GLOSSARY or LIST OF ACRONYMS | 98 |
| REFERENCES | 102 |
| APPENDIX A: Technology demonstrations | A-1 |
| Sensing of High-density Polyethylene Pipeline Deformation using Distributed Strain Sensing | A-1 |
| High Pressure Test of Corroded Gas Well Tubing | A-10 |
| Detection of Water Table Depth using P-Wave Refraction with Geophones and Distributed Acoustic Sensing | A-14 |
| Sensing of Steel Pipeline Deformation using Distributed Strain Sensing..... | A-23 |
| Pipeline Component Laboratory Cyclic Bending Test using Distributed Fiber Optic Sensing | A-27 |
| Pipeline Subsystem Laboratory Shaking Table Test using Distributed Fiber Optic Sensing | A-33 |

LIST OF FIGURES

| | Page |
|--|------|
| Figure 1: Data-Driven Model Updating | 9 |
| Figure 2: The Coverage and Error Range of the Commonly Used Remote Sensing Technologies (Greenwood et al., 2019) | 20 |
| Figure 3: Leica BLK360 Pulse-based Short-range LIDAR | 23 |
| Figure 4: Surphaser 100HSX Phase-based Short-range LIDAR..... | 23 |
| Figure 5: Riegl VZ-400i Phase-based Long-range LIDAR | 23 |
| Figure 6: Using Multiple Scenes for SfM 3D Model Reconstruction | 29 |
| Figure 7: Variable Definitions for Camera Imaging | 30 |
| Figure 8: Variable Definitions for Camera Imaging | 31 |
| Figure 9: Schematic of Distributed Fiber Optic Sensing System | 32 |
| Figure 10: Total Internal Reflection Scattering of Incident Light (Soga & Luo, 2018) .. | 34 |
| Figure 11: Total Internal Reflection Scattering of Incident Light (Soga & Luo, 2018) .. | 34 |
| Figure 12: Strain Transfer Mechanism from Infrastructure to the Core of Fiber (Soga & Luo, 2018) | 35 |
| Figure 13: Total Internal Reflection Scattering of Incident Light (Soga & Luo, 2018) .. | 37 |
| Figure 14: Three Scattering Modes of Backscattered Lights (Soga & Luo, 2018)..... | 37 |
| Figure 15: Distributed Fiber Optic Sensing Classification Based On Scattering Techniques (Soga & Luo, 2018) | 37 |
| Figure 16: Luna Odisi 6100 High-Definition Fiber Optic Sensing Interrogators | 39 |
| Figure 17: SensorNet Halo DTS Distributed Temperature Sensing System | 42 |
| Figure 18: Optasense ODH-4 Distributed Acoustic Sensing Interrogator..... | 45 |
| Figure 19: WSN Instrumentations..... | 48 |
| Figure 20: Typical WSN System Architecture..... | 48 |
| Figure 21: Data Rate and Range of Related Radio Technologies (Mekki et al., 2019) .. | 49 |
| Figure 22: FDR Soil Moisture Sensor – METER Environment EC-5 (METER Environment)54 | |
| Figure 23: Capacitive Accelerometer – Analog Devices EVAL-ADXL335 (Analog Devices)56 | |
| Figure 24: Piezoresistive Accelerometer – Endevco 35B-2 (Endevco) | 56 |
| Figure 25: Piezoelectric Accelerometer – PCB Piezotronics 350B43 (PCB Piezotronics). 58 | |
| Figure 26: Embedment Semiconductor Strain Gauge – GEOKON Model 3900 (GEOKON)60 | |

| | |
|---|----|
| Figure 27: Vibrating Wire Strain Gauge – GEOKON Model 4000 (GEOKON) | 60 |
| Figure 28: LVDT – GEOKON Model 1450 (GEOKON) | 61 |
| Figure 29: Linear Potentiometer– GEOKON Model 1500 (GEOKON) | 61 |
| Figure 30: Draw-wire Sensor – TE Connectivity Measurement Specialties SP1-50 (Digi-Key) | 62 |
| Figure 31: Ultrasonic Range Finder – MaxBotix XL-MaxSonar-WR/WRC (MaxBotix) | 63 |
| Figure 32: Infrared Proximity Sensor – Sharp GP2Y0A41SK0F (Sparkfun) | 63 |
| Figure 33: Lite LiDAR Module – Benewake TF03 (Sparkfun) | 64 |
| Figure 34: VCSEL sensor – STMicroelectronics VL53L1X (STMicroelectronics) | 64 |
| Figure 35: PIG Launcher & Receiver (Sagebrush)..... | 67 |
| Figure 36: T.D. Williamson Multiple Dataset (MDS) system (T.D. Williamson)..... | 67 |
| Figure 37: Different ILI tool capabilities in determining corrosion features (Vanaei et al., 2017) | 68 |
| Figure 38: Magnetic Fields Generated by MFL-A (ROSEN Group) | 70 |
| Figure 39: Direction of Defects with Respect to MFL-A and MFL-C (Ho et al., 2010).... | 70 |
| Figure 40: Magnetic Fields Generated by MFL-C (ROSEN Group) | 71 |
| Figure 41: Parameters Describing Dimension of Metal Loss Feature (Pipeline Operators, 2021) | 71 |
| Figure 42: MFL-A Pig (Enduro Pipeline Services) | 73 |
| Figure 43: SMFL Pig (T.D. Williamson) | 73 |
| Figure 44: High-resolution Tri-axial MFL Pig (ROSEN Group)..... | 75 |
| Figure 45: Ultrasound Principle for Wall Thickness Measurement (Barbian et al., 2011)77 | |
| Figure 46: Illustration (top view and cross section) of Parameters Describing Location and Dimension of Crack and Crack-like Features (Pipeline Operators, 2021) | 78 |
| Figure 47: High resolution piezoelectric ultrasonic tool (ROSEN Group)..... | 83 |
| Figure 48: EMAT tool (Baker Hughes) | 83 |
| Figure 49: Figaro Catalytic Bead Sensor TGS6812-D00 (Figaro) | 85 |
| Figure 50: Infrared ethane detector (SENSIT)..... | 86 |
| Figure 51 Fixed-point Open-path Laser Methane Emissions Monitor FPL (SENSIT) | 87 |
| Figure 52: Micro Motion ELITE CMF350P Coriolis flowmeter (Micro Motion)..... | 90 |
| Figure 53: Magnetrol Thermoel TA2 Thermal Mass Flowmeter (Magnetrol) | 91 |
| Figure 54: Honeywell Elster TRZ2 Turbine Gas Flowmeter (Honeywell)..... | 92 |

| | |
|--|------|
| Figure 55: Honeywell (RMG) USM GT400 ultrasonic gas flowmeter (Honeywell) | 94 |
| Figure 56: Rosemount 8800DF040 Flanged Vortex Flowmeter (Rosemount)..... | 94 |
| Figure 57: Max Machinery G004 gear flowmeter (Max Machinery) | 95 |
| Figure A-1: Cross-section of NZS-DSS-C02 Sensing Cable (Hubbard et al., 2021) | A-2 |
| Figure A-2: Application of Tapecoat H35 and 3M DP8010 to an HDPE Pipeline for Initial Evaluation | A-2 |
| Figure A-3: Sensing Cable Attached to an HDPE Pipe | A-3 |
| Figure A-4: Strain Measurements Made During the First Bending Test | A-3 |
| Figure A-5: Test Configuration and Attachment Method Tested | A-4 |
| Figure A-6: Raw Strain Measurements During the Second Bending Test. The cable locations are denoted relative the NA position (Hubbard et al., 2021)..... | A-6 |
| Figure A-7: Bending and axial strain in the pipe during bending as determined by the NA, NA – 45° and NA + 45° cable positions (Hubbard et al., 2021). | A-7 |
| Figure A-8: Deflection of the pipe calculated from the strain measurements made by the NA, NA – 45° and NA + 45° cable positions (Hubbard et al., 2021). | A-8 |
| Figure A-9: test setup overview | A-11 |
| Figure A-10: Cable layout..... | A-11 |
| Figure A-11: Axial Strain of Tubing at 4 Locations under High Pressure | A-13 |
| Figure A-12: Schematic of p-wave refraction reciprocal method (Geometrics, 2021) | A-14 |
| Figure A-13: P-wave Refraction Test Configuration | A-17 |
| Figure A-14: Atom Seismograph Data and First Arrival Picks | A-20 |
| Figure A-15: Travel Time Curves from the 3m, 47m and 95m Shot Locations..... | A-21 |
| Figure A-16: Two-layer P-wave Velocity Model of the Test Site Using the Reciprocal P-wave Refraction Technique | A-21 |
| Figure A-17: DAS Data Plotted with the Travel Time Curves of the Arrivals Determined from the Seismograph Data | A-22 |
| Figure A-18: Pressurized steel pipe specimen before four-point bending at ADV Integrity in Waller, TX | A-23 |
| Figure A-19: Strain Measurements Made by DSS During the Pipeline Pressurization Test..... | A-24 |
| Figure A-20: Strain Measurements Made by DSS During the Pipeline Bending Test.. | A-26 |
| Figure A-21: Experiment setup | A-27 |
| Figure A-22: The instrumentation of the DSS sensors (modified from Task D)..... | A-28 |
| Figure A-23: Close-up photo of attachments..... | A-29 |

Figure A-24: Luna Odisi 6100 High-Definition Fiber Optic Sensing Interrogator..... A-30

Figure A-25: Strain distribution profile on north and south sides of the horizontal Tee joint outlet at 1st maximum magnitude of 13th load cycle A-31

Figure A-26: Maximal and minimal strain measured on north and south sides of horizontal section A-32

Figure A-27: Maximal and minimal strain versus actuator’s displacement A-32

Figure A-28: Experiment setup A-33

Figure A-29: The instrumentation of the DSS sensor (modified from Task D) A-35

Figure A-30: Close-up photo of attachments..... A-35

Figure A-31: Strain measurement after each load at section 1 A-36

Figure A-32: Measured bending of the tank on north-south direction (positive to south)A-37

LIST OF TABLES

Page

| | |
|---|----|
| Table 1: Gas Pipeline Simulation Tool Parameters | 11 |
| Table 2: Gas Storage Wells Simulation Tool Parameters | 12 |
| Table 3: Gas Facilities Components Simulation Tool Parameters | 13 |
| Table 4: Comparisons of Remote Sensing Technologies..... | 19 |
| Table 5: Common Terms of Remote Sensing Technologies | 20 |
| Table 6: Comparison of LIDAR Types (Kayen, 2021) | 22 |
| Table 7: Typical Specifications of TLS LIDAR | 22 |
| Table 8: Comparison of Different Wavelength SAR Systems (Kayen, 2021) | 26 |
| Table 9: Example Cost for Private Data of Japan PASCO ALOS-1 (Kayen, 2021) | 27 |
| Table 10: Typical Specifications of InSAR (Kayen, 2021)..... | 27 |
| Table 11: Typical Cost of Commercial Software for SfM 3D Model Reconstruction..... | 29 |
| Table 12: Typical Cost and Performance of Some Commercially Available Satellite-Based Imaging Services..... | 29 |
| Table 13: Common Terms of Distributed Fiber Optic Sensing Technologies and Specification | 33 |
| Table 14: Selected Commercially Available Fiber Optic Sensing Cables..... | 35 |
| Table 15: The Specification of Selected Commercial Distributed Strain and Temperature Sensing Systems (Soga & Luo, 2018)..... | 39 |
| Table 16: Specification of Selected Commercial DTS Systems (Soga & Luo, 2018)..... | 42 |
| Table 17: Specification of Selected Commercial DAS Systems (Soga & Luo, 2018)..... | 44 |
| Table 18: Current Comparison in TX, RX, Idle and Sleep Modes (Gaddam & Rai, 2018)..... | 49 |
| Table 19: Overview of the Several Commercial Low-power Wide-area Networks Technologies (Mekki et al., 2019) | 50 |
| Table 20: Wireless Sensor Network Based Sensing Technologies and the Corresponding Events and Occasions | 53 |
| Table 21: Associable Sensing Technologies for Smart PIG..... | 66 |
| Table 22: Typical Operating Specification of Smart PIG | 66 |
| Table 23: Inspection Technologies and Related Anomalies (T.D. Williamson) | 68 |
| Table 24: Typical specification of magnetic flux leakage (ROSEN Group) | 72 |
| Table 25: Comparisons of different types of ultrasonic inspection..... | 81 |

| | |
|--|------|
| Table 26: Typical specification of ultrasonic inspection (ROSEN Group)..... | 82 |
| Table 27: Comparison of Combustible Gases Sensing Technologies..... | 84 |
| Table 28: Comparison of Natural Gas Flow Monitoring Technologies..... | 88 |
| Table 29: Common Terms of Natural Gas Flowmeters | 89 |
| Table 30: Typical Specifications of Coriolis Flowmeters..... | 90 |
| Table 31: Typical specifications of thermal mass flowmeters..... | 90 |
| Table 32: Typical Specifications of Turbine Gas Flowmeters..... | 91 |
| Table 33: Typical Specifications of Ultrasonic Gas Flowmeters..... | 93 |
| Table 34: Typical Specifications of Vortex Flowmeters | 94 |
| Table 35: Typical Specifications of Positive Displacement Flowmeters..... | 96 |
| Table A-1: Different testing cases for the experiment..... | A-11 |
| Table A-2: Schematic illustration of the selected strain sensing fibers structures (Wu et al., 2015) | A-30 |
| Table A-3: Specification of the demonstrated BOTDR..... | A-34 |
| Table A-4: Schematic illustration of the selected strain sensor cable (Wu et al., 2015)A-34 | |

EXECUTIVE SUMMARY

Introduction

This report is one of a series of reports documenting the methods and findings of a multi-year, multi-disciplinary project conducted by the Pacific Earthquake Engineering Research Center (PEER) with the Lawrence Berkeley National Laboratory (LBNL), and funded by the California Energy Commission (CEC). The overall project is titled "Performance-based Earthquake Engineering Assessment Tool for Natural Gas Storage and Pipeline Systems" henceforth referred to as the "OpenSRA Project."

The overall goal of the OpenSRA project is to create an open-source research-based seismic risk assessment tool for natural gas infrastructure that can be used by utility stakeholders to better understand state-wide risks, prioritize mitigation, plan new gas infrastructure, and help focus post-earthquake repair work.

The project team includes researchers from LBNL, UC Berkeley, UC San Diego, University of Nevada Reno, the NHERI SimCenter at UC Berkeley, and Slate Geotechnical Consultants and its subcontractors Lettis Consultants International (LCI) and T.D. O'Rourke of Cornell University. Focused research to advance the seismic risk assessment tool was conducted by Task Groups, each addressing a particular area of study and expertise, and collaborating with the other Task Groups.

This report is the product of the Task Group E: Smart gas infrastructure sensing of wells and pipeline connections performance. The scope of this report is to present the state-of-the-art for sensing and monitoring technologies that apply to natural gas infrastructure and present a framework for incorporating sensed information into predictive risk models. Monitoring technologies have changed rapidly, making it challenging for gas companies to respond to the opportunities they provide. This research is supported by California ratepayers because technologies, which can help keep natural gas contained, are in the best interest to the state's climate goals, and should be presented to infrastructure owners with strong arguments for their implementation.

California's natural gas infrastructure must deal with a unique set of seismic hazards across varying terrain and an extensive land mass. Earthquakes can cause subsurface ground movements, landslides, soil liquefaction, and lateral spreading of the ground. These hazards may damage natural gas infrastructure. The purpose of the current project is to provide the Open Seismic Risk Assessment (*OpenSRA*) tool with which infrastructure owners and operators can quantify the risks from the different seismically induced hazards. Those risks are quantified using models that predict infrastructure performance when an earthquake occurs. The models are based on knowledge learned from laboratory tests, case studies and numerical simulations.

With monitoring technologies it is possible to make ground-truth observations about gas infrastructure performance that both grows trust in the predictive models and adds more information into decision making. Monitoring technologies can be widely implemented to compliment modeled behavior with actual performance.

Project Purpose

As part of the larger *OpenSRA* project, this research task aims inform the California infrastructure owners about the rapidly growing state-of-the-art instrumentation and monitoring, who can then implement them to make natural gas infrastructure safer for both the environment and consumers. In the last two decades, the fields of electrical engineering and computer science have produced many new sensing technologies that can be applied to monitoring natural gas infrastructure. Many of the new technologies can make a meaningful change to the way these systems are operated and maintained.

In addition to the obvious reason for monitoring infrastructure to detect damage, the future of risk quantification lies in leveraging measured data to update current risk models. Similarly to the advancement in sensing technologies, prediction models for estimating events such as liquefaction and landslides have also progressed. These models take in information about site conditions and possible earthquakes to predict the likelihood of a hazardous event. That information is then coupled with the response of the system to quantify the risk to natural gas infrastructure. The outputs of *OpenSRA* are predicted deformation of the natural gas subsystems and the likelihood that they will experience a loss of containment (LOC).

The models are broken down into categories for buried pipelines (Task B), storage wells (Task C) and surface facilities (Task D). Each set of models have their own inputs, intermediate variables and outputs. Fusing monitoring with these models means that the measured data must interact at all stages. First, the input data can be measured and verified to estimate starting conditions with minimized uncertainty. Next, the intermediate variables can be compared with measured data to ensure that the models are capturing the real behavior. Finally, the outputs of the models need to be verified with real measurable data to quantify their uncertainty for implementations when measurements may not be possible due to budget constraints.

This project's goal is to identify the technologies that can inform the risk models at the input, intermediate and final output stages, while providing a guide to the state-of-the-art monitoring technologies that natural gas infrastructure owners can understand and implement quickly.

Project Approach

The task of identifying monitoring technologies that can inform the *OpenSRA* models was conducted. The research team received technical guidance in the form of a technical advisory committee (TAC) with members from Pacific Gas and Electric (PG&E) and Southern California Gas Company (SoCalGas).

The steps to complete a comprehensive review of natural gas monitoring technologies involved (1) reviewing an extensive list of available technologies, (2) getting feedback from technical advisors on the most relevant technologies, (3) coordinating with other task groups to understand their risk models, and (4) demonstration testing a select subset of technologies with large impact potential.

This report presents tabulated results of commercially available sensing and monitoring technologies that can be adopted by stakeholders to provide the same parameters used by the *OpenSRA* models. The research team compiled a list of relevant monitoring technologies for natural gas infrastructure, and then produce a framework to incorporate their measurements into the *OpenSRA* risk models.

The report is separated into remote sensing, continuous monitoring, inspection technologies, and leak detection technologies. The remote sensing technologies encompass techniques where no contact needs to be made with the infrastructure. The continuous monitoring technologies includes technologies that are installed on or in the infrastructure to collect information about it for an extended period. Inspection technologies are used at specific times to collect information about the condition of the infrastructure. Finally, leak detection technologies are of particular importance to monitoring natural gas infrastructure and warrant a discussion of their own.

Project Results

The research outcomes that have been performed under this subtask include guidance on selected technologies and metrics for evaluating the value of sensing within the *OpenSRA* framework. Selected methods that can be used to estimate the most probable parameters for the *OpenSRA* models are also introduced.

Sensor and monitoring technologies appropriate for buried pipelines, storage wells and surface facilities are presented. The capabilities, limitations, and costs of new emerging and existing technologies are introduced and compared. The emerging technologies examined include: (a) distributed fiber optic sensing of temperature, strain and vibration for real-time structural health monitoring, (b) long-range wireless sensor network for remote monitoring, (c) LiDAR, InSAR and computer vision with satellite images for ground and structure movement monitoring, (d) high performance gas sensors, (e) flow monitoring at smart meters level for large-scale system-level operational monitoring, and (f) in-line inspection using smart PIG.

Selected sensor and monitoring technologies were tested in the laboratory and in the field to assess their system accuracy and resolution. Different types of distributed fiber optic sensors (DFOS) were trialed in collaboration with the work conducted in other tasks. The accuracy and resolution of these sensors were verified and compared to those of conventional sensors.

CHAPTER 1:

Introduction

This report is one of a series of reports documenting the methods and findings of a multi-year, multi-disciplinary project conducted by the Pacific Earthquake Engineering Research Center (PEER) with the Lawrence Berkeley National Laboratory (LBNL), and funded by the California Energy Commission (CEC). The overall project is titled "*Performance-based Earthquake Engineering Assessment Tool for Natural Gas Storage and Pipeline Systems*" henceforth referred to as the "OpenSRA Project."

The overall goal of the OpenSRA project is to create an open-source research-based seismic risk assessment tool for natural gas infrastructure that can be used by utility stakeholders to better understand state-wide risks, prioritize mitigation, plan new gas infrastructure, and help focus post-earthquake repair work.

The probabilistic seismic risk tool developed in this project follows the widely-accepted risk methodology of Dr. A. Cornell (Cornell, 1968). A seismic source characterization is used to develop a suite of earthquake scenarios with associated rates of occurrence to represent the seismic hazard. Fault ruptures and the resulting ground deformation are generated for each earthquake scenario to represent the seismic loading, which includes a map of ground motion parameters. This scenario-based seismic parameter map is overlaid on the infrastructure system and the seismic loading combined with the capacities of the infrastructure to calculate the seismic performance of the natural gas system for the scenario. By repeating the process for all the scenarios in the suite, the tool can evaluate the seismic risk to the system.

A user-driven research approach was used to develop OpenSRA to be easily usable by regulators and utilities, and to include updated models and methods for the seismic demands and capacities that control the seismic risk for natural gas systems. The project includes several innovative approaches that improve the basic methodology. These approaches distinguish this project from standard methods currently used. Risk studies developed by utilities use risk scoring that is highly subjective and qualitative. They do not properly incorporate the uncertainties in the seismic demand and in the fragility of the system and its components. Targeted research was conducted in this project to improve the characterization of uncertainty of key inputs to the seismic risk assessment tool. The seismic risk methodology employed in this project provides quantitative estimates of the probabilistic seismic risk. For risk-informed decision-making processes, the reliability of the risk estimates needs to be considered because this can be significant, particularly for large rare earthquakes.

The project team includes researchers from LBNL, UC Berkeley, UC San Diego, University of Nevada Reno, the NHERI SimCenter at UC Berkeley, and Slate Geotechnical Consultants and its subcontractors Lettis Consultants International (LCI) and T.D. O'Rourke of Cornell University. Focused research to advance the seismic risk assessment tool was conducted by Task Groups, each addressing a particular area of study and expertise, and collaborating with the other Task Groups. The Task Groups are as follows:

- Task A: Fault Displacement
- Task B: Liquefaction-induced deformation and seismically induced slope displacement
- Task C: Performance of natural gas storage well casings and caprock
- Task D: Performance of gas storage and pipeline system surface infrastructure
- **Task E: Smart gas infrastructure sensing of wells and pipeline connections performance**
- Task F: Synthesis of component fragilities into a system performance model

This report is the product of the Task Group denoted in bolded text above. This report is a guide to help readers with selecting and adapting the emerging sensing technologies and their measurements to *OpenSRA* risk tools developed by other task groups

Background

As California strives for carbon neutrality, energy demand is currently met through a combination of renewables and fossil fuels. As of 2020, natural gas was responsible for 42.97% of the energy generated within the state (California Energy Commission, 2021). This demand is not expected to decrease by 2025. Natural gas is primarily methane, which has 25 times more warming potential if released into the atmosphere than carbon dioxide. Keeping natural gas contained within the transmission, storage, processing, and distribution systems is a critical part of California's efforts to reduce global warming. At the same time, California is situated in an area of high seismicity where earthquakes pose a serious threat. Damage to natural gas infrastructure from earthquakes can cause components to break and uncontrollably release methane-rich natural gas into the atmosphere.

California's natural gas infrastructure must deal with a unique set of seismic hazards across varying terrain and expansive land mass. Earthquakes can cause both surface and subsurface ground movements, including landslides, soil liquefaction, and lateral spreading of the ground. These hazards may damage natural gas infrastructure. The purpose of this project is to provide the Open Seismic Risk Assessment (*OpenSRA*) tool that infrastructure owners and operators can use to quantify the risks from the different seismically induced hazards. Those risks are quantified to predict infrastructure performance when an earthquake occurs. The models are based on knowledge learned from laboratory tests, case studies and numerical simulations.

With monitoring technologies, it is possible to make ground-truth observations about infrastructure performance to both grow trust in the predictive models as well as add valuable information into the decision making process. Monitoring technologies can be widely implemented to compliment modeled behavior with actual performance. However, many of the best monitoring capabilities are unknown to natural gas infrastructure owners.

Recent advances in sensor and communication technologies are making significant impacts on the monitoring methods for infrastructure assessment. The purpose of this report is to present the state-of-the-art for sensing and monitoring technologies that apply to natural gas

infrastructure and present a framework for incorporating sensed information into the predictive risk models. This research is supported by California ratepayers because technologies that can help keep natural gas contained are in the best interest to the state's climate goals and should be presented to infrastructure owners with strong arguments for their implementation.

This report introduces selected emerging sensing and monitoring technologies suitable for monitoring gas storage wells and pipeline systems. These include (a) distributed fiber optic sensing of temperature, strain and vibration for real-time structural health monitoring, (b) long-range wireless sensor network for remote monitoring, (c) remote sensing technologies including LiDAR, InSAR and computer vision with satellite images for ground and structure movement monitoring, (d) high performance gas sensors, (e) flow monitoring at smart meters level for large-scale system-level operational monitoring, and (f) in-line inspection using smart PIG.

Sensor systems can provide data of high resolution at relatively low cost. Some of them have broad spatial coverage. Combined with other conventional monitoring technologies and inspection techniques, there is potential to improve detection of physical measurements, including facility characteristics, ground movement, and leakage events. Smart sensing of the newly replaced well and pipeline systems in the next few decades will provide opportunities to evaluate the structural health from the beginning of its lifetime so that proactive performance-based monitoring and maintenance can be conducted.

Outcomes

This report evaluates sensor and monitoring systems in buried pipelines, storage wells and surface facilities for real-time health assessments and alerts so that appropriate mitigation measures against failures can be applied. The evaluation includes technical principles, capabilities, limitations, cost and the comparison between different technologies. Some of the most promising sensors and monitoring technologies are tested either in the laboratory or in the field to assess their system accuracy and resolution. These demonstration reports are presented in Appendix A.

To accelerate the adaptation of new sensor technologies in practice, it is also necessary to make all stages of sensing monitoring and data analysis processes tightly coupled. In this project, it is proposed that these advanced measurements are used for inputs of the *OpenSRA* simulation models of gas pipelines and wells. The new dataset obtained from these sensors can also verify *OpenSRA* simulation results to enhance confidence. For example, the data from long-term monitoring can be compared to the outputs of the simulations to reduce the uncertainty in the *OpenSRA* assessment.

This report provides guidelines for selecting suitable sensing technologies that can be used to evaluate various input, intermediate and final output parameters required by the *OpenSRA* simulation tools. By demonstrating this approach, the value of sensing becomes more evident to the stakeholders. With better data in hand, the ultimate goal is to make a step-change in the way natural gas infrastructure is constructed and maintained for improved safety, more enhanced reliability, and a better economy.

CHAPTER 2:

Project Approach

Sensing Technology Categories

The sensing technologies introduced in this report are selected depending on the requirement of *OpenSRA* simulation tool parameters, which include geologic information and characteristics of the facilities. The selected sensing technologies can be categorized into four main categories:

1. Remote sensing technologies
2. Continuous monitoring technologies
3. Inspection technologies
4. Leakage Detection Technologies

Remote Sensing Technologies

The natural gas infrastructure in California is impacted by seismic issues. It is necessary to characterize the seismic risk of natural gas infrastructure. Ground deformations become an important input of the *OpenSRA* tool at each level of analysis. Remote sensing technologies have been used widely to detect and classify objects due to its good-resolution and wide-coverage. This report will introduce the most emerging remote sensing including LiDAR, InSAR and computer vision-based satellite images processing.

Continuous Monitoring Technologies

The continuous monitoring technology category includes the technologies that can be deployed on site and operate automatically with a stand-alone power supply and cellular communication. Unlike the conventional measuring methods that are frequently performed manually, continuous monitoring technologies allow measurements to be taken automatically with a preset measuring interval at any time, which not only significantly reduces manpower cost, but also increases the measuring frequency. These advantages make it possible to capture real-time measurements during some unexpected and extreme events, such as earthquakes. The measuring interval is limited by the equipment measuring rate (usually less than a minute). Although it can also be limited by power needs, it can be optimized by presetting multiple measuring modes with pre-defined triggering methods. For example, a continuous monitoring system running at deep sleep power saving mode can be triggered by seismic sensors within its network and switch to emergency mode to run at maximum measuring rate during an earthquake. Therefore, continuous monitoring technologies can offer real-time information about critical infrastructure (e.g., pipeline system components) of the gas pipeline and well utilities for early warning or helping with mitigating the damage during the hazard. These measurements can also be used to verify the intermediate and final outputs of the *OpenSRA* simulation tool and reduce uncertainty. The selected continuous monitoring technologies include distributed fiber optic sensors (DFOS) and wireless sensor network (WSN).

In-line Inspection Technologies

The inspection technology category includes the techniques that can be used to inspect the pipeline characteristics (e.g., wall thickness and diameter) from the inside of the pipeline. The characteristics of the gas pipeline can be determined precisely even for the underground and underwater pipeline. These characteristics can be used as the reference of the inputs and to verify the intermediate and final outputs of the *OpenSRA* simulation tool therefore increase user's confidence. This report will focus on the In-line Inspection (ILI) techniques which can be done at the same time with the periodically pigging progress. The selected associated sensing technologies for ILI including magnetic flux leakage (MFL) and ultrasonic test (UT).

Leakage Detection Technologies

In addition to the sensing technology mentioned above that are used to inform the *OpenSRA* tool, leakage measurements are also important. Gas and flow sensing can not only characterize leakage events, but also provide information on the amount of the leakage, which is an important reference for helping pipeline management agencies to make decisions during hazards. This report introduces different types of gas and flow sensors, including their mechanisms, abilities, limitations and comparisons as a reference for helping users to select the sensors that suit their applications best.

OpenSRA Informing Technologies Guidance

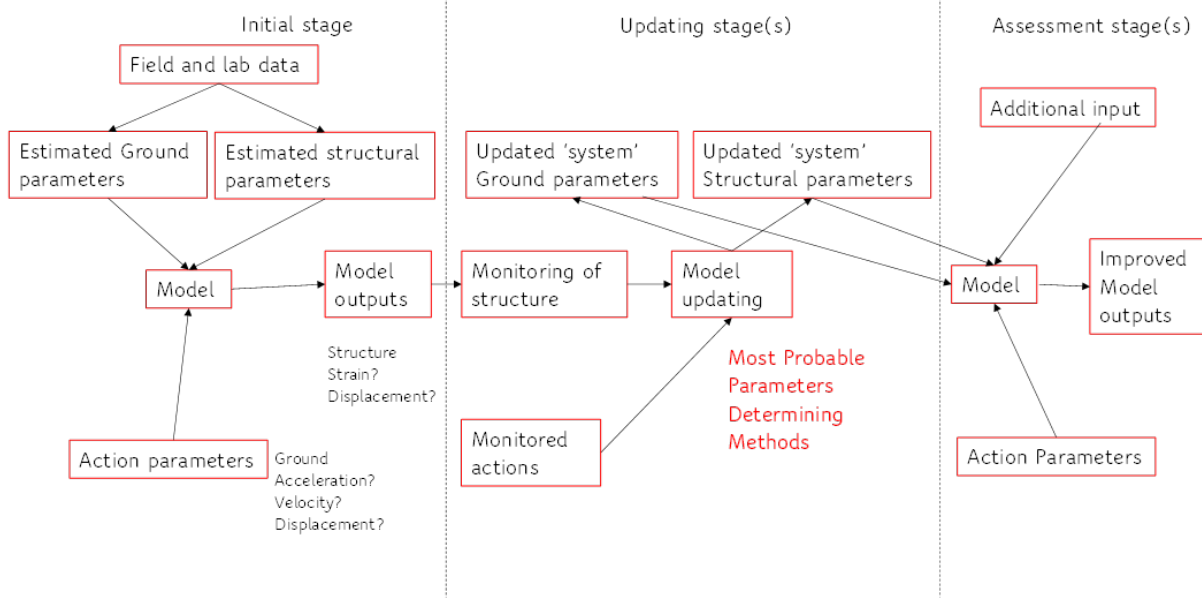
In addition to the obvious reason for monitoring infrastructure to detect damage, the future of risk quantification lies in leveraging measured data to update current risk models. Similarly, to the advancement in sensing technologies, prediction models for estimating events such as liquefaction and landslides have also progressed. These models take in information about site conditions and possible earthquakes to predict the likelihood of a hazardous event. That information is then combined with information regarding the response of the system to quantify the risk to natural gas infrastructure. The output of *OpenSRA* is predicted deformation of the natural gas subsystems and the likelihood that they will experience a loss of containment (LOC). This project's goal is to identify the technologies that can inform the risk models at the input, intermediate and final output stages, while providing a guide to the state-of-the-art monitoring technologies that natural gas infrastructure owners can understand and implement quickly.

To allow users of the *OpenSRA* simulation tool to find the sensing and monitoring technologies they need to improve their analysis, this chapter provides descriptions of available sensing technologies that can give measurements of *OpenSRA* parameters. The models are broken down into categories for buried pipelines (Task B), storage wells and caprocks (Task C) and surface facilities (Task D). Each set of models have their own input, intermediate and output parameters. Fusing monitoring with these models means that the measured data must interact at all stages. First, the input data can be measured and verified to estimate starting conditions with reduced uncertainty. Next, the intermediate parameters can be compared with measured data to ensure that the models are capturing real behavior. Finally, the outputs of the models need to be verified with real measurable data to quantify their uncertainty for implementation when measurements may not be possible due to budget constraints.

The measurements can be used as suggestions for the input parameters or verifications of the intermediate and output parameters. As shown in the following pages, a guidance sheet is given for each infrastructure type (pipelines, storage wells, and gas facilities). The sheet contains information on the parameters utilized by the *OpenSRA* tool and a description of the potential sensing technologies that can be used to measure the parameters.

When an *OpenSRA* analysis is performed, there is uncertainty due to the highly complex nature of describing the distributions of model parameters. One example is the inherent variability of soil. Uncertainties also originate from error in the measured data. Despite these uncertainties, structural performance must be evaluated to make engineering decisions. In future, we propose that the observed data be used to estimate the distribution of parameters for a given model. The data-driven model parameter updating concept is shown in Figure 1.

Figure 1: Data-Driven Model Updating



Gas Pipelines

The *OpenSRA Task B. Liquefaction-Induced Deformation and Seismically-Induced Slope Displacement* is focusing on the estimation of damage to underground pipelines caused by permanent ground deformation resulting from liquefaction, fault rupture, and landslides during an earthquake. The pipeline response estimate requires both infrastructure and geotechnical characteristics.

Table 1 shows examples of the required input as well as intermediate and final output parameters used with this tool. The brief description, typical units and available measurement approaches of each parameter are introduced in the table.

Table 1: Gas Pipeline Simulation Tool Parameters

| VARIABLES | | DESCRIPTION | UNIT | AVAILABLE TECH | |
|--------------|--------------|---|--|-------------------------|--|
| INPUT | STRUCTURAL | D | Pipe outside diameter | mm | Ultrasonic, Magnetic Flux Leakage with caliper |
| | | t | Pipe wall thickness | mm | Ultrasonic, Magnetic Flux Leakage |
| | | σ_y | Pipe yield stress | kPa | - |
| | | n | Ramberg-Osgood parameter | UNITLESS | - |
| | | r | Ramberg-Osgood parameter | UNITLESS | - |
| | GEOTECHNICAL | γ_t | Total unit weight of backfill soil | kN/m ³ | - |
| | | H | Soil cover to centerline of pipeline | m | - |
| | | L | Length of ground deformation zone | m | LIDAR |
| | | ϕ' | Backfill friction angle | Degree ° | - |
| | | δ | Sand/pipe interface friction angle ratio | UNITLESS | - |
| | | PGD | Permanent ground deformation | m | LIDAR, InSAR, Structure from Motion |
| INTERMEDIATE | t_u | Force per unit length of pipeline | kN | DSS, WSN (Strain gauge) | |
| | β_p | Pipe burial parameter | kPa | - | |
| | L_e | Embedment length | m | - | |
| | $L_e \sigma$ | Standard deviation of L_e estimate (ln units) | - | - | |
| | L^* | Value of L to use in pipe strain equation | - | - | |
| OUTPUT | γ | Pipe strain | % | DSS, WSN (Strain gauge) | |
| | σ | Standard deviation of pipe strain estimate (ln units) | - | - | |
| | τ | Epistemic uncertainty | - | - | |

All variables and references used for description in this table correspond to Task B report

Gas Storage Wells

The *OpenSRA Task C. Performance of Natural Gas Storage Well Casings and Caprock* is focusing on the estimation of damage to caprock and well integrity caused by permanent shear displacement across a well. Both the well characteristics and ground conditions are required by the gas storage wells response estimate. The brief description, typical units and available measurement approaches of each parameter are introduced in the table.

Table 2 shows examples of the required input, generated intermediate and final output parameters used in this tool. The brief description, typical units and available measurement approaches of each parameter are introduced in the table.

Table 2: Gas Storage Wells Simulation Tool Parameters

| VARIABLES | | DESCRIPTION | UNIT | AVAILABLE TECH | |
|-----------|-----------------|------------------|--|-------------------|--|
| INPUT | CASING & TUBING | μ | Casing-tubing interface friction coefficient | - | - |
| | | P_{csg} | Casing Pressure | MPa | WSN (pressure sensor) |
| | | E | Young's modulus of casing/tubing | GPa | - |
| | | ρ | Density of casing/tubing | kg/m ³ | - |
| | | | Poisson's ratio of casing/tubing | - | |
| | | ϕ_{cmt} | Internal friction angle of cement | Degree ° | - |
| | | UCS_{cmt} | Uniaxial compressive strength of cement | MPa | - |
| | | $\sigma_{t,cmt}$ | Tensile strength of cement | MPa | - |
| | | | Yield strength of casing/tubing | Ksi | - |
| | | | Yield/Tensile strength ratio of casing/ tubing | - | - |
| | WELLHEAD | | Wellhead mass per length | kg/m [lb/in] | - |
| | | | Wellhead height | m [ft] | LIDAR, Structure from Motion, WSN (displacement) |
| | GEOTECHNICAL | θ | Fault angle | Degree ° | - |
| w_{fc} | | Fault core width | m | - | |

| | | | | | |
|--------------|--|--------------------|---|-------------------|-------------------------------------|
| | | W_{dz} | Damage zone width | m | - |
| | | z | Depth of fault-well intersection | m | - |
| | | K_0 | Maximum horizontal-to-vertical effective stress ratio | - | - |
| | | E_{rck} | Young's modulus of rock | GPa | - |
| | | ρ_{rck} | Density of rock | kN/m ³ | - |
| | | PGD | Permanent ground deformation | m | LIDAR, InSAR, Structure from Motion |
| INTERMEDIATE | | Fault Displacement | | m | LIDAR, InSAR, Structure from Motion |
| OUTPUT | | Y | Pipe strain | % | DSS, WSN (Strain gauge) |
| | | M | Pipe bending moment | kN-m [lbs-ft] | DSS, DAS |
| | | σ | Standard deviation of pipe strain estimate (In units) | - | - |
| | | T | Epistemic uncertainty | - | - |

All variables and references used for description in this table correspond to Task C report

Gas Facilities

The *OpenSRA Task D. Performance of Gas Storage and Pipeline System Surface Infrastructure* is focusing on to quantify the fragilities of the interconnected components of gas storage and piping systems surface infrastructure. The infrastructure response estimate requires the characteristics of the target infrastructural components, which include pipes, elbows, tee joints, vessels, outlet and inlet pipes. Table 3 shows examples of the required input and generated final output parameters used in this tool. The brief description, typical units and available measurement approaches of each parameter are introduced in the table.

Table 3: Gas Facilities Components Simulation Tool Parameters

| VARIABLES | | DESCRIPTION | UNIT | AVAILABLE TECH | |
|-----------|-------|-------------|-----------------------------------|----------------|---|
| INPUT | . | σ_y | Pipe yield stress | MPa [psi] | - |
| | PIPES | D | Outside diameter of the pipeline. | mm [inch] | LIDAR, Ultrasonic, Magnetic Flux Leakage with caliper |

| | | | | | |
|--|-------------|-----------------|---|-----------|---|
| | | t | Wall thickness of the pipeline. | mm [inch] | Ultrasonic, Magnetic Flux Leakage |
| | ELBOWS | D | Outside diameter of the pipeline. | mm [inch] | LIDAR, Ultrasonic, Magnetic Flux Leakage with caliper |
| | | t | Wall thickness of the elbows. | mm [inch] | Ultrasonic, Magnetic Flux Leakage |
| | TEES | D | Outside diameter of the tees. | mm [inch] | LIDAR, Ultrasonic, Magnetic Flux Leakage with caliper |
| | | t | Wall thickness of the tees. | mm [inch] | Ultrasonic, Magnetic Flux Leakage |
| | VESSEL | Hpv | Total height of the pressure vessel. | m [ft] | LIDAR, Structure from Motion, WSN (displacement) |
| | | Dpv | Diameter of the pressure vessel. | - | LIDAR, Structure from Motion |
| | | Design Pressure | Design pressure for the vessel (used to calculate thickness). | - | - |
| | | Thickness | Vessel thickness. | mm [inch] | Ultrasonic, Magnetic Flux Leakage |
| | OUTLET PIPE | Hop_Joint1 | Height of joint 1 of outlet pipe. | % | LIDAR, Structure from Motion, WSN (displacement) |
| | | LO12 | Length of segment LO12. | % | LIDAR, Structure from Motion, WSN (displacement), DSS |
| | | LO23 | Length of segment LO23. | % | LIDAR, Structure from Motion, WSN (displacement), DSS |
| | | Hop_Joint4 | Height of joint 4 of outlet pipe. | m [ft] | LIDAR, Structure from Motion, WSN (displacement) |
| | | LO45 | Length of segment LO45. | m [ft] | LIDAR, Structure from Motion, WSN (displacement), DSS |
| | | Joint 4 type | Type of joint at node 4 for outlet pipe. | - | - |
| | | Joint 5 type | Type of joint at node 5 for outlet pipe. | - | - |

| | | | | | |
|--------|---------------|--------------|--|-----------------|---|
| | INLET PIPE | Hip_Joint1 | Height of joint 1 of inlet pipe (% of Hpv [0-1]) | % | LIDAR, Structure from Motion, WSN (displacement) |
| | | LI12 | Length of segment LO12 (% of Dpv) | % | LIDAR, Structure from Motion, WSN (displacement), DSS |
| | | Joint 2 type | Type of joint at node 5 for inlet pipe | - | - |
| | WELLHEAD TREE | Hwh | Total height of the wellhead above ground | m [ft] | LIDAR, Structure from Motion, WSN (displacement) |
| | | LHwk | Height of the horizontal section | m [ft] | LIDAR, Structure from Motion, WSN (displacement) |
| | | Kwh | Average stiffness of the wellhead | kN/m [kip/inch] | - |
| | | Mwh | Linear mass of the wellhead tree | kg/m [kip/inch] | - |
| | | LP_0-1 | Length of segment LP_0-1 | m [ft] | LIDAR, Structure from Motion, WSN (displacement), DSS |
| | | LP_1-2 | Length of segment LP_1-2 | m [ft] | LIDAR, Structure from Motion, WSN (displacement), DSS |
| | | LP_2-3 | Length of segment LP_2-3 | m [ft] | LIDAR, Structure from Motion, WSN (displacement), DSS |
| | | LP_3-4 | Length of segment LP_3-4 | m [ft] | LIDAR, Structure from Motion, WSN (displacement), DSS |
| | | Joint 1 type | Type of joint at node 1 | - | - |
| | | Joint 2 type | Type of joint at node 2 | - | - |
| | | Joint 3 type | Type of joint at node 3 | - | - |
| | | Joint 4 type | Type of joint at node 4 | - | - |
| OUTPUT | | Y | Strains | % | DSS, WSN (Strain gauge) |
| | | T | Epistemic uncertainty | - | - |

All variables and references used for description in this table correspond to Task D report

CHAPTER 3:

Project Results

Remote Sensing Technologies

Introduction to Remote Sensing Technologies

Remote sensing technologies acquire information about an object without any physical contact. Although numerous technologies meet this definition, the term "remote sensing" generally refers to the use of satellite, aircraft, or terrestrial-based sensor technologies to detect and classify information about the Earth. Remote sensing allows it to collect data in dangerous or inaccessible areas and ensure that areas or objects are not disturbed during the measuring.

The technologies can be divided into two types: active and passive, depending on the source of the signal. Active sensors contain a signal source to emit the signal (e.g., electromagnetic radiation) to the object and detect the reflection to get the information of the object. The most significant advantage of active remote sensing is a high power signal, which results in better resolution and less effect from the weather. Passive sensors capture the natural signal emitted or reflected by the object to gather the information of the object, such as the reflected sunlight. Most are capable of being deployed on a variety of platforms, such as Terrestrial (static and mobile, carried by human or vehicle), airborne (airplane or unmanned aerial vehicle, UAV), and spaceborne (satellite or shuttle).

The most commonly used active remote sensing technologies for ground movement monitoring are light detection and ranging (LiDAR) and Interferometric Synthetic Aperture Radar (InSAR). Both LiDAR and InSAR emit a pulse of energy and record its return to the sensor. Most LiDAR systems use a near-infrared laser. Although they can penetrate low vegetation, it is still challenged when penetrating fog or rain (Fowler, 2001) and heavily vegetated areas. InSAR uses a longer wavelength compared to that of LiDAR. The wavelength allows it to penetrate fog and rain, and thus it can fly higher and faster than most LiDAR systems.

Photography is commonly used as passive remote sensing for ground movement monitoring. The photo set taken by an aircraft or a satellite is processed by 3D reconstruction methods based on computer vision and computer graphics. Structure from Motion (SfM) is the most popular algorithm of the 3D reconstruction methods, which uses consequent aerial or satellite photos to process the object's movement in the photos. Photography, however, cannot penetrate vegetation or fog because passive remote sensing technologies are based on sight.

The output of remote sensing can be processed by 3D reconstruction methods, such as 3D point clouds, digital elevation models (DEM), and orthophotos. The ground movement can be determined by comparing the DEM before and after an event. The position measurement is necessary to reconstruct the 3D model, usually using an associated Real-Time Kinematic (RTK) Global Positioning System (GPS). The error of the outputted 3D model is the combination of

the errors from sensing and positioning. Therefore, the sensor specification with a specific platform and the final outputted 3D model need to be considered when selecting the technology and platform.

This section introduces the most widely used remote sensing technologies, including LiDAR, InSAR, and photography with SfM. All have been used by the gas and oil industry for quick and safe 3D mapping. Some can also identify corrosion, cracks, and surface welding defects associated with fuel storage facilities. Such features help utilities with timely maintenance and business continuity. The introduction in this section includes remote sensing mechanisms, classification, costs, typical sensor specifications, and 3D model specifications. Table 4 compares the three remote sensing technologies. Each technology and platform combination has specific coverage and error. Figure 2 shows the coverage range and error associated with most remote sensing technologies. As shown in the figure, each technology carried by different platform has its specific coverage and error. Therefore, there is no technology is better than the others. It is a tradeoff between the coverage and error. When selecting the remote sensing technology, the acceptable error and coverage of the application should be considered.

Table 5 shows the common terms and their definitions and units of remote sensing technologies.

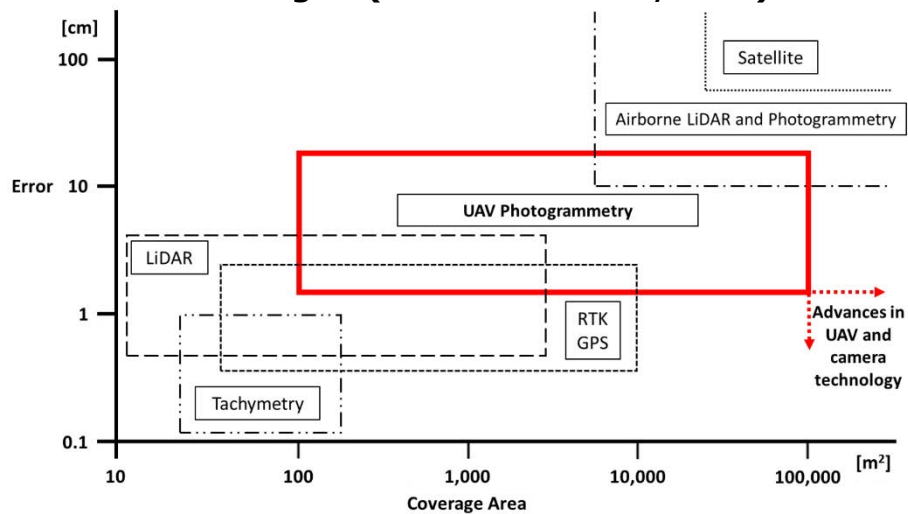
Table 4: Comparisons of Remote Sensing Technologies

| TECHNOLOGY | ADVANTAGES | DISADVANTAGES | OCCASIONS |
|----------------------------------|--|--|--|
| LiDAR | Highest accuracy, able to penetrate vegetation | Cannot penetrate fog and rain, high cost | Most cases except during fog or rain |
| InSAR | Accurate, available for most cases | High cost | Most cases |
| Aerial and satellite photography | Relatively low cost | Need line of sight | Low-vegetation area or vegetation height is considered, and without fog and rain |

Table 5: Common Terms of Remote Sensing Technologies

| TERMS | DEFINITION | UNITS |
|----------------------|--|------------------|
| DEM | Digital Elevation Models | - |
| DSM | Digital Surface Model (includes Terrain, vegetation, structures) | - |
| DTM | Digital Terrain Model | - |
| DDM | Digital Deformation Model | - |
| Range | The greatest measuring distance. | km [mile] |
| Field of view (FoV) | The angle which is covered by the sensor, usually consist of horizontal and vertical angels. | Degree ° |
| Accuracy | The closeness of the measurements to the true value. | m, cm [ft, inch] |
| Error | The difference between the approximation and the exact value, which includes manual and technical effects. The error of remote sensing can be caused by the georeferenced, equipment and registration. | m, cm [ft, inch] |
| Laser classification | Lasers are classified for safety purposes based on their potential for causing injury to humans' eyes and skin. Only class 1 is eyes safe. | - |

Figure 2: The Coverage and Error Range of the Commonly Used Remote Sensing Technologies (Greenwood et al., 2019)



Light Detection and Ranging

LIDAR is a very accurate active remote sensing technology rangefinder (e.g., <0.05% error), which uses near-infrared light mostly to image objects. It can be used either in the day or at the night since it uses its own energy to target a wide range of materials, including non-metallic objects, rocks, rain, chemical compounds, aerosols, clouds, single molecules, etc. LIDAR for three-dimensional structures, produces very accurate and precise data (e.g., typically 30cm for airborne LIDAR and 3cm for terrestrial LIDAR). It also filters reflections from vegetation to create a digital terrain model, although the ground surface is concealed by trees. LIDAR cannot penetrate clouds, fog, and rain, and thus its operation is confined to fair weather conditions.

LIDAR uses a laser to generate a stream of high energy photons in a narrow range of wavelengths, the near-infrared portion of the spectrum, to strike and reflect off objects. It utilizes two different scanners to measure the reflected laser beam: Pulse-based Scanner and Phase-based Scanner.

Pulse-based laser rangefinder has a typical error of 1-20mm at full range, which is the most common design for Terrestrial Laser Scanning (TLS) units. It measures the two-way travel time of a laser beam that backscatters off an object. The distance between the LIDAR and the object can then be estimated by using the time of flight method (ToF) based on the formula:

Equation 1

$$D = ct/2$$

where D is the estimated distance between LIDAR and object, c is the speed of light (3×10^8 m/s), and t is the measured time for the light pulse to return.

Phase-based LIDAR is the most common design of Airborne Laser Scanning (ALS) and other long-range measuring due to its very high precision (e.g. 1mm). It measures the sub-wavelength range via interferometry. The distance can be determined by the sum of the received wavelength using the formula:

Equation 2

$$D = \lambda N + \lambda \phi / 2\pi$$

where D is the estimated distance between LIDAR and object, λ is the wavelength of the source light, N is the received full-cycle wavelength number, and ϕ is the phase angle of the rest of the phase.

LIDAR can be classified based on (i) Platform – airborne, static terrestrial and mobile terrestrial, (ii) Range – short, long, and water penetrating, and (iii) Technology – pulse-based and phase-based. Table 6 compares different LIDAR types (Kayen, 2021). The selection of the platform and the range depends on the data's purpose, size of the area to be scanned, range of measurement desired and the budget of the application, e.g., *OpenSRA* analysis. Generally, TLS is more commonly used than ALS. Table 7 shows the specifications of some market available products, as an example for each type of LiDAR. Their photos are shown in Figure 3, Figure 4 and Figure 5.

When using LiDAR measurement for 3D reconstruction, the minimum total error of the generated 3D model is a function of GPS error, laser error, and registration error. The total error can be expressed by the formula as below (Kayen, 2021):

Equation 3

$$\epsilon_{total} = \sqrt{\epsilon_{georeferenced}^2 + \epsilon_{laser}^2 + \epsilon_{registration}^2}$$

where ϵ_{total} is the minimum total error of the delivered 3D model, $\epsilon_{georeferenced}$ is the georeferenced error, depends on the specification of the associated GPS, ϵ_{laser} is the rangefinder error, the specification of LiDAR, and $\epsilon_{registration}$ is the error of the multiple scans registration.

R. Kayen (Kayen, 2021) delivered an $\epsilon_{total} = 26\text{mm}$ when using a LiDAR unit with $\epsilon_{laser} = 1\text{-}4\text{mm}$, which is governed by $\epsilon_{georeferenced}$ (typically 25mm) and $\epsilon_{registration}$ (typically 7.5mm). The error listed in LiDAR’s specification can only be achieved when looking at the relative movement between fixed georeferenced points with a single scan.

Table 6: Comparison of LIDAR Types (Kayen, 2021)

| Platform | Static Terrestrial Laser Scanning, (S)TLS | | Mobile Terrestrial Laser Scanning, (M)TLS | Airborne Laser Scanning, ALS | |
|------------------------|---|---------------------|---|------------------------------|-------------|
| | Short <100m | Long 0.25-2km+ | Short <100m | Topographic | Bathymetric |
| Range | Short <100m | Long 0.25-2km+ | Short <100m | Topographic | Bathymetric |
| Cost | \$50k | \$50k-\$200k | \$100k-\$500k | \$400k-\$1M | >\$1M |
| Precision | High-Extremely High | High-Extremely High | Moderate | Moderate | Moderate |
| Available Technologies | Pulse & Phase-based | Pulse & Phase-based | Pulse-based | Phase-based | |

Table 7: Typical Specifications of TLS LIDAR

| Types | Brand & Model | Range (m) | Field of View (°) | Accuracy (mm/m) | Scan Speed (points/sec) | Cost (\$) |
|-------------------------|------------------|----------------|-------------------|-----------------|-------------------------|-----------|
| Terrestrial Pulse-based | LEICA BLK360 | Short (0.6-60) | 360*300 | 4/10 or 7/20 | 0.36M | 19,077 |
| Terrestrial Phase-based | Surphaser 100HSX | Short (1-50) | 360*270 | 0.7/15 | 0.8M | 90,000 |
| Terrestrial Phase-based | Riegl VZ-400i | Long (1.5-800) | 360*100 | 5/800 | 0.5M | 120,000 |

Figure 3: Leica BLK360 Pulse-based Short-range LIDAR



Figure 4: Surphaser 100HSX Phase-based Short-range LIDAR



Figure 5: Riegl VZ-400i Phase-based Long-range LIDAR



Interferometric Synthetic Aperture Radar

Synthetic Aperture Radar (SAR) is a form of radar in which sophisticated radar data processing is used to produce a very narrow effective beam. The amplitude and the absolute phase of the return signal data can be used for imaging relatively immobile targets such as the Earth's surface. It is an active remote sensing technology that uses radar images (microwave) collected mainly from orbiting satellites instead of light pulses. With using different frequencies microwave signal, SAR can penetrate the moist, rain and even vegetation, and are equally effective in darkness. SAR imagery is generated by sending and catching the reflected radar signals off a target area and measuring the two-way travel time back to the satellite. The distance to the ground or an object can be calculated using either pulse-based or phase-based methods introduced in the LiDAR section.

Interferometric SAR (InSAR) is a geodesy and remote sensing technique which uses two or more SAR images to generate maps of surface deformation or digital elevation of ground deformation that covers a vast spatial area with centimeter-scale accuracy. The same area SAR images taken by the same sensors from the same location (same orbit) at different times can be compared against each other. Then, an interferometric image can be compiled by using the formula:

Equation 4

$$\phi_{int} = \frac{4\pi}{\lambda}(\rho_1 - \rho_0) + \frac{4\pi}{\lambda}(\rho_2 - \rho_1) + a + \omega$$

where ϕ_{int} is the interferometric phase, λ is the Radar wavelength, ρ is the measured ranges at different times (ρ_0 : baseline, ρ_1 : first measurement, ρ_2 : second measurement), ω is the White noise term (Refraction effect), and a is the Phase term due to atmospheric inhomogeneities (Refraction effect).

The first term in the formula is the interference between the baseline and the first measurement. The second term in the formula is the interference between the last and the previous measurements due to the deformation during the time between measurements. The rest are the nuisance terms. The outputted interferometric phases can then be processed and produce the Digital Elevation Models (DEMs), the Digital Displacement Models (DDMs) between different times can also be made by removing the topography baseline, which is the first term in the formula.

There are some limitations of InSAR. The images must be taken as close as possible to the same spatial position where the images are acquired. This means that the images from two satellites with different orbits cannot be compared. Therefore, the alternative datasets are limited, and the revisiting time of the satellite also limits the measurement frequency. InSAR can measure the vertical movement of small incident angles very well but is not sensitive to the horizontal movement perpendicular to the line of sight (for satellite-based InSAR, it is about the north-south direction). This means that vertical motion and horizontal motion components parallel to the line-of-sight plane (approximately east-west for satellite-based InSAR) cannot be resolved separately.

InSAR technique is used for monitoring landscape features such as landslides, displacement from earthquakes, ground subsidence, and volcanoes. It can help assess the stability of built structures, highway and railway settlements, dike stability, etc. Very high resolution InSAR data (such as derived from the TerraSAR-X StripMap mode or COSMO-SkyMed HIMAGE mode) are especially suitable for this task.

SAR can be classified based on (a) Platform – satellites, space shuttle, and aircraft, (b) Geometric configuration of the baseline vector – cross-track and along-track, and (c) Wavelength – L-band, C-band and X-band. Space shuttle and aircraft carried SAR are not commonly used, and the along-track interferometer can only measure the radial motion, which is usually less useful. Therefore, this section will only introduce satellite-based cross-track SAR.

There is a tradeoff between the ability of penetration and the resolution. The longer wavelengths give the potential to penetrate vegetation to the ground but with a lower spatial resolution, e.g., L-band (24cm). The shorter wavelengths provide better spatial resolution but cannot penetrate the vegetation (Ahmed et al., 2001), e.g., X-band (3cm) and C-band (6cm). However, it cannot penetrate the vegetation since light interacts most strongly with objects on the size of the wavelength. Therefore, X-band and C-band are good at mapping in dry soils and ice areas, while the L-band is good at mapping in forest areas and has better coherence. Table 8 shows the comparisons between different wavelength SAR systems.

Table 9 shows the typical performance and the cost of private InSAR data. There are also some limited free InSAR data available from NASA (Shuttle Radar Topography Mission, SRTM) and European Space Agency (ERS and Copernicus). Table 10 shows typical performance for different 3D reconstructed models using InSAR.

Table 8: Comparison of Different Wavelength SAR Systems (Kayen, 2021)

| CLASSES | SATELLITES | REVISITING TIME | WAVE-LENGTH | FREQUENCY | ADVANTAGES | OCCASIONS |
|---------|---------------------|-----------------|-------------|-----------|---|---|
| X-band | TerraSAR-X/TanDEM-X | 11 days | 3 cm | 10 GHz | Best resolution | Dry soils and ice area |
| | PAZ | | | | | |
| | COSMO-SkyMed | 16 days | | | | |
| C-band | Sentinel-1 | 12 days | 6 cm | 5 GHz | Good resolution, penetrate light vegetation | Dry soils, ice and light vegetated area |
| | Radarsat-2 | 24 days | | | | |
| L-band | ALOS-2 | 14 days | 24 cm | 1.2 GHz | Penetrate vegetation, good coherence | Most cases |
| | SAOCOM-1A | 16 days | | | | |

Table 9: Example Cost for Private Data of Japan PASCO ALOS-1 (Kayen, 2021)

| OBSERVATION MODE | DETAIL OF THE OBSERVATION MODE (ABBREVIATION) | COST | |
|------------------|---|---------|--------|
| | | Archive | New |
| Spotlight | Spotlight (SPT) | \$4000 | \$5500 |
| Stripmap | Ultra-Fine (SM1), res. 3m | \$2400 | \$3900 |
| | High-sensit (SM2), res. 6m, 50km | | |
| | Fine (SM3), res. 10m, 70km | | |
| | High-sensitive (SM2) [Full Polarimetry], 50km | | |
| | Fine (SM3) [Full Polarimetry], 70km | | |
| ScanSAR | ScanSAR Nominal [28Mhz] (WD1), 350km | \$800 | \$2300 |
| | ScanSAR Nominal [14Mhz] (WD1), 350km | | |
| | ScanSAR Wide (WD2), 490km | | |

Table 10: Typical Specifications of InSAR (Kayen, 2021)

| APPLICATIONS | ACCURACY | RESOLUTION |
|------------------------------------|----------|------------|
| Digital Elevation Models (DEMs) | 2-5m | 5-10m |
| Digital Displacement Models (DDMs) | 3-10mm | 10-100m |

Structure from Motion

Photography is a passive remote sensing technology that uses optical cameras for collecting the photo sequences of the target objects or area. Cameras can be mounted on various platforms, including people, cars, UAVs, planes, and satellites. The objects must be in the line of sight since an optical camera cannot see through obstructions such as fog, rain, and vegetation. Therefore, UAV becomes more popular because of its 3D mobility, which offers improved and adjustable field of view to image the blocked objects. However, each platform has its specific resolution versus coverage and revisiting time. The selection of the platform should depend on the application, desired spatial extent and resolution, desired data frequency collection, sensor (camera), and the required field of view (Zekkos, 2021).

Structure from motion (SfM) is a digital photogrammetry technique for reconstructing 3D models from 2D photo sequences collected by photography based on computer vision and visual perception, as shown in Figure 6. The objects move in different amounts depending on the distance to each view spot, known as motion parallax. These distances can be used to interpret the geometry or 3D model, considering uncertainty in the camera's location. The locations of the view spots are not necessary when using SfM since they can also be calculated.

The correspondence between images and the reconstruction of the 3D object needs to be found to identify the same object in different images (the dots shown in Figure 6). To find correspondence between images, features of the object, such as corner points or edges with gradients in multiple directions, are tracked from one image to the next. Therefore, the target image's resolution, overlap, and texture will affect the results. Typically, imagery overlap of 70% or higher is recommended. Some feature detectors algorithms can detect the correspondence between images automatically. These include scale-invariant feature transform (SIFT) and speeded-up robust features (SURF).

The generated 3D model can be optimized by adding ground control points and ground checkpoints during surveying, which can be identified throughout the photoset and associated with RTK-GPS. Ground control points are used as the georeferenced of the 3D model in the desired coordinate system, which can optimize solution processing and fix the model distortions. Ground checkpoints are used to estimate model errors by comparing the computed coordination with the equipped RTK-GPS measurement.

The data processing for SfM is complex and time consuming. At the moment, the time spent on data processing is significantly longer than data collection, e.g., 1 field day of collection may need 2-5 days of data processing. High-Performance Computing (HPC) is required for large-area (> few km²) images processing. The minimum processing requirements of HPC are recommended by Zekkos (2021): Modern processors, Minimum RAM of 32 GB (but 64 GB or 124 GB is better), excellent graphics card, 4K screen (to be able to see the details).

The appropriate commercial software as well as a person or subcontract devoted to the project are needed to create a quality model with the proper assessment of errors, limitations etc. Table 11 lists the typical costs for software associated with three commercially available SfM systems. SfM can be classified by its optical imagery platforms: ground-based, airborne and satellite-based. The resolution of optical imagery is a function of the camera and the distance to the target. Therefore, the performance of the satellite-based optical imagery is usually constant for each satellite since they typically fly at a constant height.

Table 12 shows the cost and performance of some commercially available satellite-based imaging services.

Figure 6: Using Multiple Scenes for SfM 3D Model Reconstruction

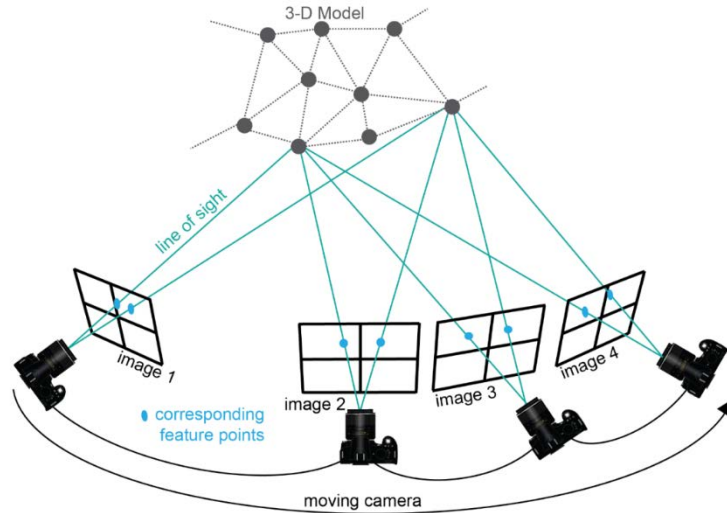


Table 11: Typical Cost of Commercial Software for SfM 3D Model Reconstruction

| SfM 3D Model Reconstruction Software | Cost (starting at) |
|--------------------------------------|---|
| Bentley's ContextCapture | \$3,392+ (/year) |
| Pix4D | \$4,290+ (/year) / \$6,990+ (/one-time) |
| Agisoft Metashape | \$3,499 (/one-time) |

Table 12: Typical Cost and Performance of Some Commercially Available Satellite-Based Imaging Services

| Satellites | WorldView-1 | WorldView-2/3 | QuickBird | GE-1/ WV-4 | IKONOS | Pléiades 1A/1B |
|-------------------------------------|-------------|---------------|-----------|---------------|---------|-------------------|
| Resolution | 50cm | 50cm | 60cm | 50cm | 80cm | 50cm |
| Panchromatic | \$14.00 | \$14.00 | \$14.00 | \$14.00 | \$10.00 | \$12.50 |
| 3-Band Pan-Sharpended | - | \$17.50 | \$17.50 | \$17.50 | \$10.00 | \$12.50 |
| 4-Band Pan-Sharpended | - | \$17.50 | \$17.50 | \$17.50 | \$10.00 | \$12.50 |
| Panchromatic + 4-band Multispectral | - | \$17.50 | \$17.50 | \$17.50 | \$10.00 | \$12.50 |
| 8-band Multispectral | - | \$19 | - | - | - | - |
| 8-band Panchromatic + Multispectral | - | \$19 | - | - | - | - |

When using ground-based and airborne optical imagery, the distance from the sensor to the target can be changed frequently, so the resolution may vary even using the same camera. Therefore, it is typically expressed with Ground Sampling Distance (GSD, cm/pixel) and point cloud density (# or points/m³). From the similarity of triangles (

Figure 7), GSD can be calculated by the formula:

Equation 5

$$GSD = \frac{H \times Sw \times 100}{f \times ImW}$$

where H is the flight height or distance to object in m, Sw is the sensor width in mm, constant for a specific type of camera, f is the Focal length in mm, ImW is the Digital width of the image in pixels, constant for a specific type of camera.

For a given camera, the GSD is controlled by f and H. Therefore, a flight plan needs to consider to generate the desired type/quality of data. Figure 8 shows some examples of the GSD versus flight height. D. Zekkos (Zekkos et al., 2018) also recommended having at least 2-10 pixels per dimension of feature as the desired resolution.

The magnitude and direction of ground deformations as well as the geometries of gas facilities are important inputs of the *OpenSRA* tools. This section introduced emerging remote sensing technologies such as LiDAR, InSAR and computer vision-based satellite images processing for these purposes due to its good-resolution and wide-coverage. Examples of their applications are given in Tables 1-3 in Chapter 2.

Figure 7: Variable Definitions for Camera Imaging

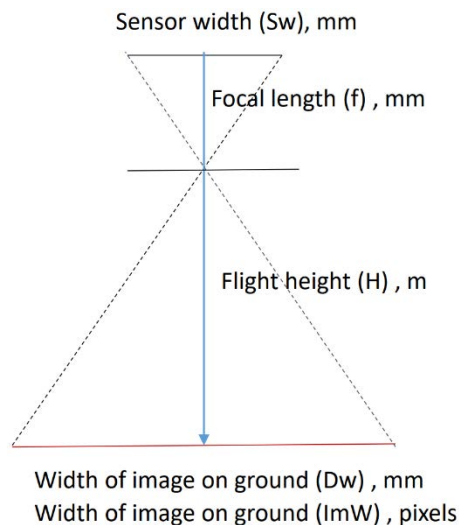
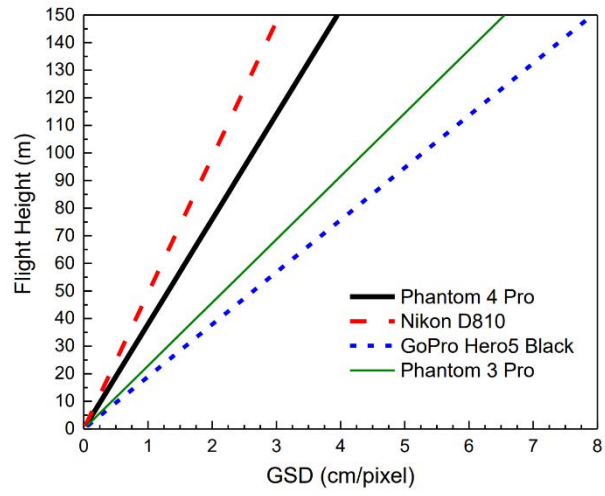


Figure 8: Variable Definitions for Camera Imaging



Continuous Monitoring Technologies

Distributed Fiber Optic Sensors

Introduction to Distributed Fiber Optic Sensing

Distributed Fiber Optic Sensing (DFOS) is a promising family of technologies used in various fields for structure health monitoring (Bao & Chen, 2011). Figure 9 shows the schematic of the DFOS system, an interrogator (also referred to as an analyzer) is used as both the source of light and the data acquisition unit for a fiber optic sensor. When taking the measurement, interrogator will send a series of optical pulses (the big orange arrows shown in Figure 9) into an optical fiber (multi-channels are available for some interrogators) which is used as continuous sensing elements. When optical pulses propagating through the fiber, it will generate some light pulses called back-scattering (the small orange arrows shown in Figure 9) due to the impurities of the fiber. The back-scattered light will be affected by the physical quantities of the fiber (such as temperature, strain, and vibration). The interrogator will measure the back-scattered light pulse and identify their location every measuring interval, which is also known as readout intervals (the interval between each data point shown in Figure 9). Therefore, every measuring interval of the fiber can be considered as an individual strain, thermal, or vibration sensor (depending on the selected technology). These 'virtual' sensors can be distributed continuously along the fiber for long distances (say 10 km) due to their low-loss characteristic. And the measurement interval can be as small as a millimeter for specific DFOS techniques. Which gives DFOS the advantages of high sensitivity over large distances and the ability to interface with a wide range of measurands in a distributed manner. Table 13 shows some common terms of DFOS technologies and specifications.

Figure 9: Schematic of Distributed Fiber Optic Sensing System

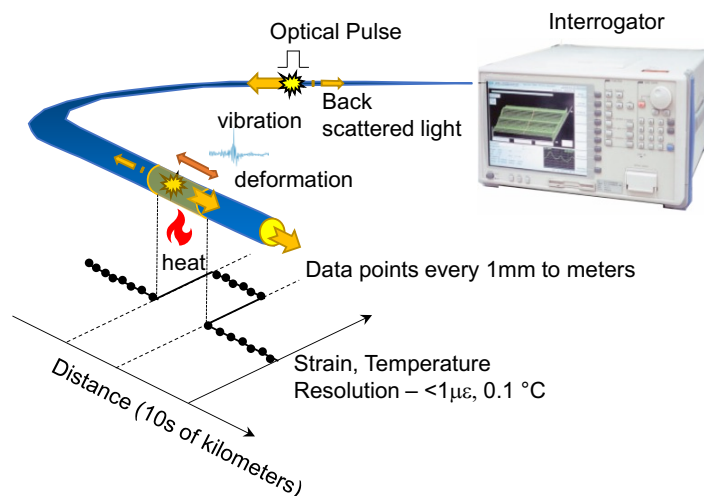


Table 13: Common Terms of Distributed Fiber Optic Sensing Technologies and Specification

| TERMS | DEFINITION | UNITS |
|------------------------|--|---------------------------------------|
| DSS | Distributed strain sensing. | - |
| DTS | Distributed temperature sensing. | - |
| DAS | Distributed acoustic sensing. | - |
| DTSS | Distributed temperature and strain sensing. | - |
| OTDR | Optical time domain reflectometry. | - |
| OFDR | Optical frequency domain reflectometry. | - |
| OCDR | Optical correlation domain reflectometry. | - |
| OTDA | Optical Time domain analysis. | - |
| Spatial resolution | Length of fiber that influences the measurement made at a single virtual sensing point. | mm, cm, m |
| Read-out | Also known as sampling interval; The distance between two virtual sensors. | mm, cm, m |
| Measurement resolution | The smallest difference of measurands that can be observed from measurement output. | nε for DSS °C for DTS g for DAS |
| Measurement time | The time required to obtain one measurement of measurands from every virtual sensor along a fiber (strain, temperature, etc.). | sec |
| Measurement Distance | The maximum length of sensing fiber that can be used with a DFOS system while preserving performance specifications. | m, km |

Measurement Mechanism

Figure 10 shows the cross-section of optical fiber generally separated into three layers: core, cladding and buffer. The core at the center is surrounded by cladding which has a lower refractive index and covered by the protective buffer at the outside. Figure 11 (Soga & Luo, 2018) explains how the light (black arrows in Figure 11) propagates along the optical fiber core. When the incidence angle of the light at the core-cladding interface (θ_i in Figure 11) is smaller than the critical angle, the light will be totally reflected back to the core medium, which is known as total internal reflection. Therefore, the light wave can then propagate along the fiber through multiple reflections as the black arrows shown in Figure 11. Optical fiber takes the advantage of total internal reflection to guide the light transmitted along its longitudinal axis (e.g., Agrawal, 2007), even when the fiber is bent (Soga & Luo, 2018).

Outside of the cladding is covered by a protective jacket (the buffer shown in Figure 10), which helps the fiber from being damaged by the environment. The materials and structures

of the protective jacket may vary depending on the application. Therefore, protective coating plays an important role in DFOS.

Figure 10: Total Internal Reflection Scattering of Incident Light (Soga & Luo, 2018)

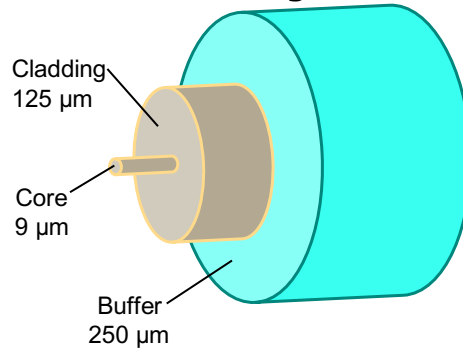
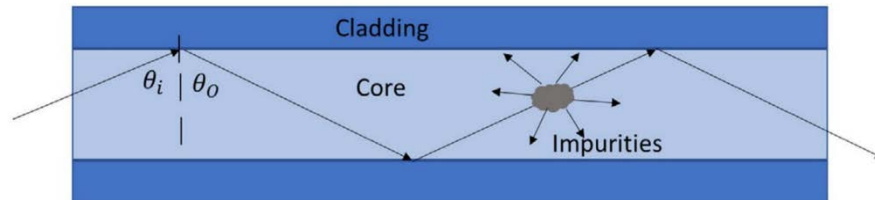


Figure 11: Total Internal Reflection Scattering of Incident Light (Soga & Luo, 2018)



DFOS can only sense the strain of the fiber core, where the back-scattered optical pulse generated. To use it for measuring the strain of other objects, the bondings between each interface are also important. Figure 12 shows what strain does DFOS system really delivered. The transfer of strain from the structure to the fiber core is achieved through shearing along the tightly bonding interfaces between series of materials from the structure, jacket, cladding, and core as shown in Figure 12 (Soga & Luo, 2018). The strain transfer mechanism between the structure and the optical fiber depends on the gauge length as well as on the mechanical properties of the coating material (Ansari, 2007; Culshaw et al., 1996). Therefore, for strain and vibration sensing, the bonding between each layer needs to be as tight as possible. The upper limit of strain measuring range is limited by the lowest value of the bonding shear strength between each layer and the upper strain limit of the optic fiber (approximately 3-5%) (Silva-López et al., 2005). On the other hand, for the optical fiber cables used to measure temperature need to be slippery between each layer, therefore the strain effect can be isolated and only temperature effect will be measured. A proper strain calibration test is required for any cables used for DFOS (Soga & Luo, 2018).

Table 14 shows some selected optical fiber cables and their specification. There are mainly three types of buffers: tight, loose and hybrid. Tightly bonded buffer is the only option for measuring strain. Loosely bonded buffer can prevent the strain transfer to the fiber core and therefore is good for temperature sensing. However, there is a technology can sense the temperature without the strain effect and therefore loosely bonded buffer is not necessary for temperature sensing. Hybrid buffer contains both tightly and loosely bonded fibers and can be used for both applications. Usually these cables are protected by two protections: reinforcement metal wire/tube and waterproof plastic cover.

Figure 12: Strain Transfer Mechanism from Infrastructure to the Core of Fiber (Soga & Luo, 2018)

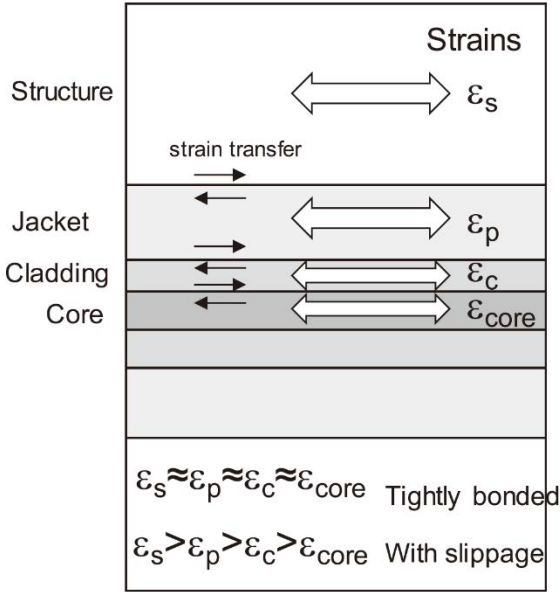


Table 14: Selected Commercially Available Fiber Optic Sensing Cables

| COMPANY | NanZee Sensing | Smartec | Solifos | Smartec |
|-----------|-------------------|----------------------|---------------------|----------------------|
| MODEL | NZS-DSS-C02 | Hydro & Geo | 3_50_1_001 | SMARTProfile II |
| BUFFER | Tight | Tight | Loose | Hybrid |
| TARGETS | Strain | Strain & temperature | Temperature | Strain & temperature |
| DIMENSION | $\phi 5\text{mm}$ | $\phi 6\text{mm}$ | $\phi 3.8\text{mm}$ | 8mm x 4mm |
| DIAGRAM | | | | |
| PHOTO | - | | - | |

NanZee NZS-DSS-C02 only has one single-mode fiber which is protected by six metal reinforcement that spiral around it and tightly bond the fiber, which makes it suitable for strain sensing. Outside of the reinforcement is covered by a polyethylene outer sheath. The buffer design of Smartec Hydro & Geo cables is very similar but with multiple types of fibers. It contains both single-mode and multi-modes fibers. Single-mode fiber is usually used for strain sensing. When using specific technology, multi-modes fibers can be used for temperature

sensing without the strain effect as mentioned previously. Therefore, Smartec Hydro & Geo can be used for both strain and temperature sensing even with a tight buffer design. Solifos 3_50_1_001 has a similar buffer design compared to Smartec Hydro & Geo which also allows multiple fibers but with a loose buffer to isolate the strain for a better temperature sensing. The design of Smartec SMARTProfile II is obvious different from the others. It has both tight and loose buffers, two single-mode fibers located outside of the red tube shown in the diagram are tightly bonded with the buffer, which are designed for strain sensing. Inside of the red tube are two single-mode and two multi-modes fibers with a loose buffer (gel). This allows it can be used for two different ways (single-mode and multi-mode) of temperature sensing. And its shape is a rectangular, which is easier to be attached onto the structure's surfaces in most cases. The details of the sensing technologies mentioned above will be introduced in the following sections.

As light travels through the optical fiber (the blue arrows shown in Figure 13), a small portion is reflected back towards the source at each location (the red arrows shown in Figure 13) due to imperfections in the fiber (as shown in Figure 11). These reflections are called back-scatter. There are three types of back-scatter: Rayleigh, Brillouin, and Raman (Figure 14). Rayleigh back-scatter is at the same frequency of the source light. It is used to assess the integrity of fiber optic cables used for telecommunications because the intensity of the reflected light is related to the intensity of light propagating forward in the cable. Rayleigh back-scatter can be used to sense strain, temperature, and vibration. Brillouin back-scatter is shifted in frequency from the source light. The magnitude of the frequency shift is dependent on the temperature and strain in the fiber, and therefore it is very useful for sensors. Raman back-scatter is also shifted in frequency from the source light, but its frequency does not change. The power of Raman scattering does vary with temperature, which makes Raman back-scatter very useful for temperature sensing.

There are different detection techniques used for finding the location of the measurement, while the back-scatter only tell the information of the strain, temperature, or vibration.

1. Optical time domain reflectometry (OTDR) – A pumping pulse light of known width is transmitted and measures the reflected energy and time of flight.
2. Optical frequency domain reflectometry (OFDR) – A continuous laser source is swept in the frequency domain over a period of time, where the spectrum is spatially related to amplitude and phase of the scattered light.
3. Optical correlation domain reflectometry (OCDR) – Pumping correlation codes of varying levels of sophistication.
4. Optical time domain analysis (OTDA) – Pump and probe lights are transmitted from both ends of the fiber and analyze the power difference related to time delay

Figure 15 shows the common combination between the back-scattered mode and the available detection techniques. The detail of each scattering mode will be introduced in more detail as below.

Figure 13: Total Internal Reflection Scattering of Incident Light (Soga & Luo, 2018)

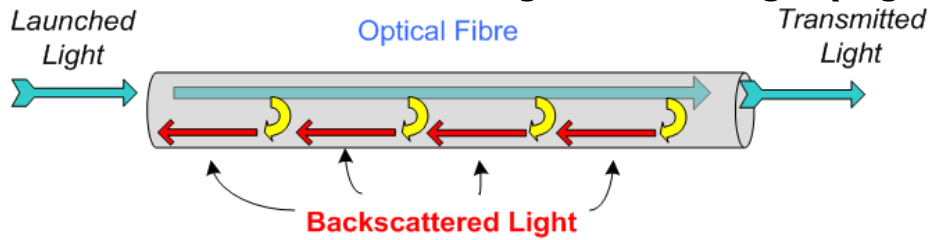


Figure 14: Three Scattering Modes of Backscattered Lights (Soga & Luo, 2018)

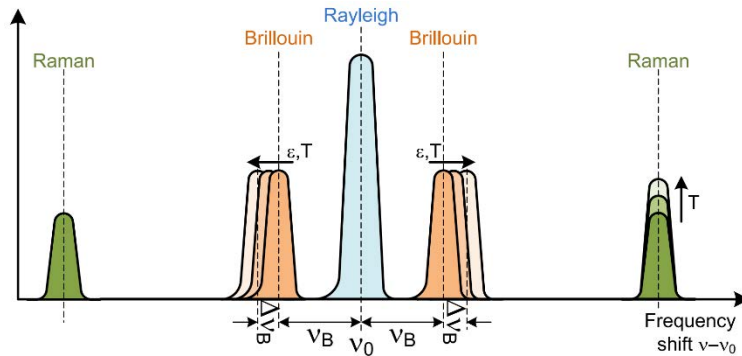
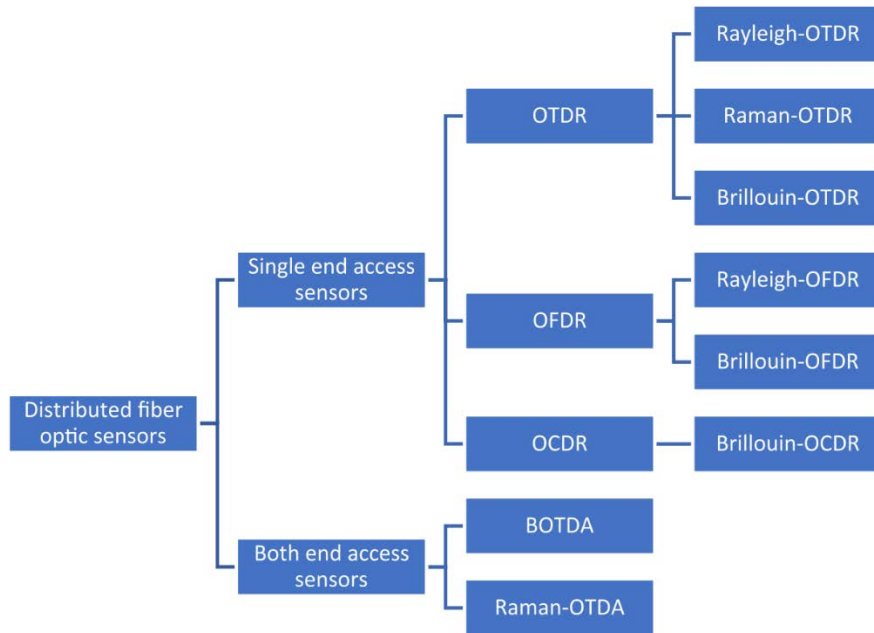


Figure 15: Distributed Fiber Optic Sensing Classification Based On Scattering Techniques (Soga & Luo, 2018)



Classifications

Although DFOS can be categorized depending on the back-scattered modes or the detection techniques, it is more convenient to be categorized by their functionality:

1. Distributed strain and temperature sensing (DSTS)
2. Distributed temperature sensing (DTS)

3. Distributed acoustic sensing (DAS)

Distributed Temperature and Strain Sensing

Distributed strain and temperature sensing (DSTS) is a subset of distributed fiber optic sensing (DFOS) technologies where strain and temperature are measured simultaneously. In DSTS techniques, both strain and temperature affect the measured property of the light. Since both influence the physics, a mechanical technique must be used to separate temperature and strain. This is typically done by having a tightly buffered fiber optic cable that is sensitive to both strain and temperature changes and a loose-tube style cable that does not transfer strain to the core. Both cable structures can also be incorporated in a single cable unit with more than one optical fiber inside. The measurements made by the loose-tube style cable are then subtracted from the tightly buffered cable, so independent measurements of temperature and strain are obtained.

Rayleigh and Brillouin scattering are examined in different DSTS techniques. Since temperature and strain do not physically change the properties of Rayleigh scattering, they cannot be used for absolute measurements. Instead, Rayleigh scattering is used much like a laser distance measuring device common in construction work to observe the geometry of the fiber optic cable. Then, changes to the geometry from mechanical or thermal induced strain can be measured by comparing two or more measurements. This is done by comparing the phase or Rayleigh backscatter spectrum (RBS). The phase of Rayleigh backscatter changes proportionally to strain and temperature induced on the fiber. The RBS also changes linearly with strain and temperature because the spacing of inhomogeneities (reflectors) is related to the RBS. Rayleigh scattering is used commercially for DSTS primarily by LUNA and Neubrex Inc. Measurement distances vary widely for Rayleigh based systems. LUNA offers systems for short distance measurements of less than 50m and spatial resolutions less than 1mm. Neubrex Inc. offers Rayleigh-based DSTS systems with measurement distances up to 27km and a spatial resolution of 2cm. Rayleigh-based systems can have a very high measurement resolution of less than $1\mu\epsilon/0.05^\circ\text{C}$. However, since Rayleigh-based technologies require relative measurements, they can be less suited for long-term monitoring. Typically, a Rayleigh-based interrogator needs to be operated continuously to continue to make measurements, whereas a Brillouin-based system (see next) examines an absolute phenomenon that can be compared over long timeframes at different acquisitions.

Brillouin scattering experiences a frequency shift proportional to the temperature and strain at the scattering location. It is used in Brillouin Optical Time Domain Reflectometry (BODTR) and Brillouin Optical Time Domain Analysis (BODTA). BODTR measures the optical power of the spontaneous Brillouin scattering from a pulse of light passed down a fiber. The frequency components of the backscattered light are analyzed to create a reconstructed Brillouin spectrum. This spectrum is used to determine the strain or temperature at each location in the fiber. BODTA is similar, however, stimulated Brillouin scattering (SBS) is employed. Light pulses are passed down each end of a closed loop of fiber and the light interacts. This interaction causes Brillouin scattering with higher power than the BODTR method, which results in higher measurement resolution and a shorter acquisition time. BODTR can achieve about $\pm 20\mu\epsilon$, while BODTA can typically achieve $\pm 10\mu\epsilon$. The main advantage of Brillouin-

based methods is that measurements do not need to be continuously taken. Measurements can have minutes to years between them to examine the temperature and strain experienced by the sensing fibers, which is advantageous for civil infrastructure long-term monitoring. Table 15 shows some selected commercial DSTS systems' specifications. Figure 16 shows the photo of Luna ODiSI 6100 high resolution DSTS interrogator and its controlling mobile workstation.

Table 15: The Specification of Selected Commercial Distributed Strain and Temperature Sensing Systems (Soga & Luo, 2018)

| TYPES | BRAND & MODEL | MAX. DISTANCE | MIN. READ-OUT | MIN. SPATIAL RESOLUTION | ACCURACY | MIN. SAMPLE FREQUENCY |
|--------------|---------------------|---------------|---------------|-------------------------|------------------|-----------------------|
| OTDR OTDA | Neubrex NBX-7031 | 27km | 10mm | 20mm | 20nε/ 0.001°C | 0.2Hz |
| OFDR | Luna ODiSI 6100 | 50m | 0.65mm | - | <±1με/ - | 10Hz |
| OFDR | Semicon OSI-S | 100m | 1mm | 1mm | ±1με/ ±0.1°C | 4Hz |

Figure 16: Luna Odisi 6100 High-Definition Fiber Optic Sensing Interrogators



All three are widely used for measuring temperature, though Raman scattering is the most common in DTS only systems. Rayleigh scattering requires an interferometric method to measure strain and temperature, meaning that all measurements are relative to a baseline established during data acquisition. Brillouin scatter analysis techniques make it possible to measure strain uncalibrated, meaning that data acquired at separate times can be compared to determine strain and temperature change between data acquisitions.

Distributed Temperature Sensing

Raman-based DTS is currently dominant in distributed photonics sensor technology for temperature measurement, especially for long distances. It is widely employed in the oil and gas industry and for power cable measurement. Raman scattering is generated by the interaction between the photons of the incident light and the material optical phonon (Boyd, 2008). The photon of incident light turned into a lower frequency phonon (Stokes wave). The rest energy and the momentum forms a phonon in the material structure. Inversely, a higher frequency phonon (anti-Stokes wave) is generated as the photon provides energy and momentum to satisfy conservation. Raman scattering generates a lower frequency phonon with lower energy (Stokes wave) and a higher frequency phonon with higher energy (anti-Stokes wave). The ratio of the two wave powers and their wavelengths are related to the temperature at the scattered location (Soga & Luo, 2018).

The ratio of the Stokes and anti-Stokes intensities of backscattered light can be detected by using time-domain reflective (OTDR) technique. However, the attenuation in the Stokes and anti-Stokes wavelengths are different; i.e., the ratio will be changed after the attenuation. There are two-ends and one-end types of Raman-based OTDR (ROTDR) that can be used to solve this issue. Two-ends type ROTDR decodes the two different attenuations by sending pump waves from both ends, while one-end ROTDR compensates the difference in attenuation by sending two light sources with different wavelengths and then evaluating the attenuation coefficients (Soga & Luo, 2018).

Raman scattering has a lower power compared to other back-scatters (approximately three orders of magnitude weaker than Rayleigh scattering). Therefore, high sensitive photodiode and multimode fiber with large scattering coefficients are usually used to generate a large Raman scattering signal due to the higher nonlinear effect (Soga & Luo, 2018). The measuring distance of ROTDR is typically limited to 10km due to the signal loss and fiber intermodal dispersion (Bao & Chen, 2012) with a capability of 1 m to 5 m spatial resolution and 0.1 to 1°C temperature resolution depending on the sensing distance and measurement speed (Yokogawa DTSX200, 2017).

Table 16 shows some selected commercial DTS system specifications. Figure 17 shows the photo of Sensornet HALO-DTS DTS interrogator.

Table 16: Specification of Selected Commercial DTS Systems (Soga & Luo, 2018)

| BRAND & MODEL | MAX. DISTANCE | MIN. READ-OUT | MIN. SPATIAL RESOLUTION | ACCURACY | MIN. SAMPLE RATE |
|---------------------------------|---------------|---------------|-------------------------|----------|------------------|
| Sensornet HALO-DTS | 4km | 2m | - | 0.45°C | 15sec |
| NKT Photonics LIOS EN.SURE OTS4 | 80km | 0.25m | 1m | 2°C | 60sec |
| Sensornet Sentinel DTS-XR SM | 30km | 1m | 1m | - | 10sec |
| OZ Optics ForeSight-BDTS | 10km | - | 1m | 0.3°C | 24sec |

Figure 17: Sensornet Halo DTS Distributed Temperature Sensing System



Distributed Acoustic Sensing

DAS uses Rayleigh scattering to measure dynamic strain in an optical fiber. Three analysis methods are currently used in DAS sensing; (i) Phase Optical Time Domain Reflectometry (ϕ -OTDR), (ii) Coherent Optical Time Domain Reflectometry (COTDR) and (iii) Optical Frequency Domain Reflectometry (OFDR).

ϕ -OTDR is a technology that examines coherent reflections from two different locations in a fiber spaced by a distance called the gauge length and then combines them to form an interference pattern. The interference is used to determine the light phase change over that section of the fiber. This is called a change in optical path length, and it is measured in radians of the light's wavelength. Since the measurements are made on the order of the light's wavelength, ϕ -OTDR systems are extremely sensitive. Commercial systems often report their noise floor in units of pico strain level. ϕ -OTDR is used in seismic monitoring and geophysical applications.

COTDR is an older DAS technology than ϕ -OTDR. In COTDR, the phase of the light is not measured, but the change in amplitude of the interference (similar to ϕ -OTDR) is measured instead. The COTDR output is optical power over time. The optical power is then summed over a fiber length and reported as the measurand. The summed optical power within a range bin is related to strain in the optical fiber, but not a direct measurement of it like ϕ -OTDR. Thus,

COTDR results cannot be correlated to geophone or accelerometer time history data. COTDR is suitable for general vibration monitoring such as pipeline leak detection and perimeter monitoring.

OFDR is the newest generation of DAS sensing techniques. In OFDR, two pulses of light with different wavelengths are injected into the optical fiber at a time spacing equal to the gauge length over the speed of light. The Rayleigh backscatter, therefore, has different wavelengths that are equivalent to the two injected wavelengths. The backscatter interferes at the optical detector, and the phase difference is determined. This phase change is a direct measurement of the strain, much like ϕ -OTDR. This technology creates a phase-coherent time series for each gauge length along the optical fiber. This technology is suited for waveform analysis of seismic waves.

Like other Rayleigh-based techniques, absolute values of strain and temperature are not obtainable using DAS because measurements are relative to previous baselines during data acquisition. Furthermore, DAS has inherent noise at zero frequency, which destroys static strain and temperature measurements. Therefore, DAS can be viewed as a dynamic measurement of strain over a finite period.

Table 17 shows some selected commercial DAS system specifications.

Figure 18 shows the photo of Optasense ODH-4 DAS interrogator.

In DFOS, every measuring interval of the fiber can be considered as an individual strain, thermal, or vibration sensor (depending on the selected technology). These 'virtual' sensors can be distributed continuously along the fiber for long distances (say 10 km) due to their low-loss characteristic and the measurement interval can be as small as a millimeter for specific DFOS techniques. For Open SRA tools, DSTS technology can be used to measure strains of pipelines, storage wells and facilities in continuous manner. Examples of their applications are given in Tables 1-3 in Chapter 2. DTS can be used to measure temperature changes of the monitored structures, whereas DAS can be used for dynamic measurement of strain over a finite period.

Table 17: Specification of Selected Commercial DAS Systems (Soga & Luo, 2018)

| TYPES | BRAND & MODEL | MAX. DISTANCE | READ-OUT | MIN. SPATIAL RESOLUTION | FREQUENCY | |
|--------|-------------------|---------------|----------|-------------------------|-------------------|-------------|
| | | | | | RANGE | MAX. SAMPLE |
| φ-OTDR | Optasense ODH-4 | 10km | - | 1.3m | - | 200kHz |
| φ-OTDR | Silixa iDAS | 40km | >25cm | 1m | 0.01Hz ~ 50kHz | 100kHz |
| OFDR | Neubrex NBX-S4000 | 50km | 20cm | 2.8m | 1Hz ~ 2.5kHz | 5kHz |

Figure 18: Optasense ODH-4 Distributed Acoustic Sensing Interrogator



Wireless Sensor Networks

Introduction to Wireless Sensor Network

The primary purpose of gas infrastructure monitoring is to measure the properties of the fluid, environment, and supply facilities, which will be changed by the leakage. The measured properties will be provided to the operator for further decisions in real-time. The monitored properties depend on the fluid material in the monitored sections (Sun et al., 2011) and the environments such as underground, aboveground, and underwater (Abdelhafidh et al., 2018). For example, temperature sensors can be used to monitor the leakage of hot liquid pipelines (Turner, 1991; Weil, 1993). Hydrocarbon vapor sensors can be used to monitor the leakage of natural gas pipelines (Sperl, 1991). Soil moisture sensors can be used to monitor the leakage of the water pipeline underground (David & Alan, 2001; Zhang, 1996). Soil dielectric property sensors can be used to monitor the crude oil migration from underground pipelines (David & Alan, 2001; Zhang, 1996). For monitoring facility properties, a continuous wave such as noise will be generated after a leak occurs. The waves will propagate through the fluid and pipeline and can be detected by using acoustic vibration sensors such as microphone, accelerometer, or strain gauge (Hough, 1988; Klein, 1993; Kurmer, 1993; Turner, 1991; BenSaleh et al., 2013). These sensors are conventionally associated with data logging equipment for real-time monitoring, which are either prohibitively costly or highly inflexible (Anumalla et al., 2005) due to the power requirement.

However, these drawbacks can potentially be solved by using wireless sensor network (WSN) technology. Plenty of related works and commercial solutions of WSN application for pipeline monitoring can now be found in the literature and market.

Figure 19(a) shows the potential WSN instrumentations for aboveground gas facility monitoring. The differential settlement along the pipeline and facilities can be detected by using inclinometer and positioning sensors such as draw-wire sensor and positioning laser. Flowmeter and pressure transducer can deliver the parameters of the numerical analysis such as volume balance methods and real-time transient model (RTTM) methods. The strain gauge can be used for monitoring the strains of the pipeline. Sensors deployed near potential leakage positions such as joints may be embedded with an accelerometer or gas sensor to monitor the relevant leaking events. The measured data can be directly sent to a cloud platform through a cellular tower nearby by embedding a cellular transceiver within each node. For underground pipelines, a gateway may be deployed at the surface (as shown as

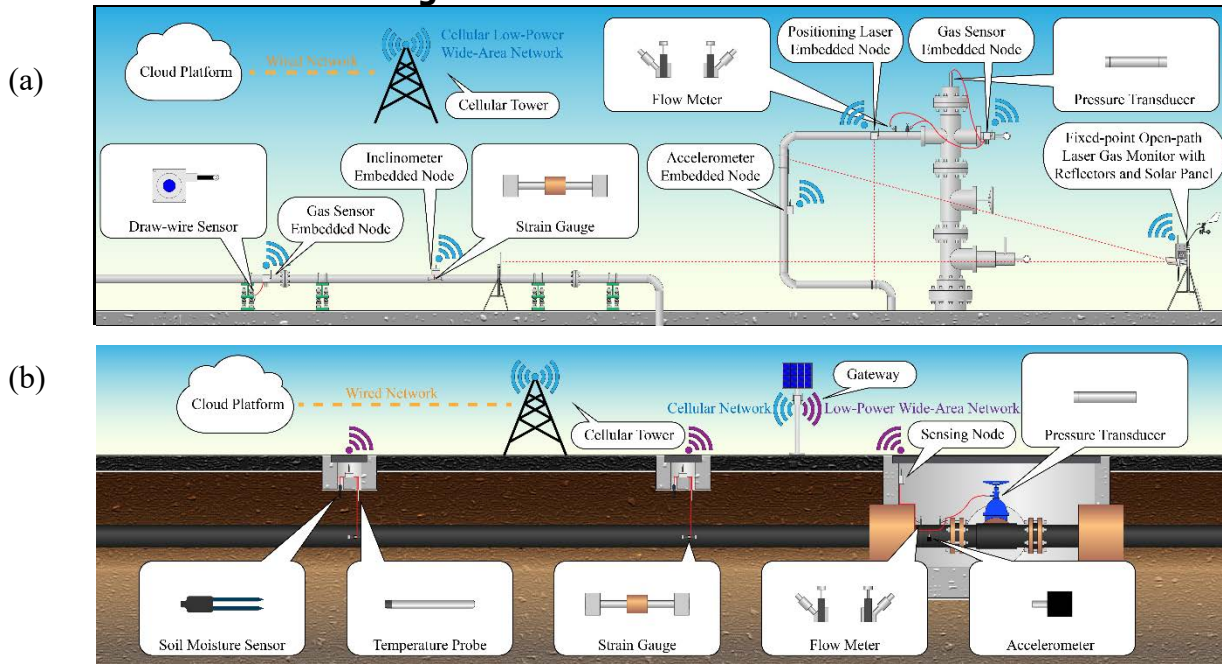
Figure 19 (b)) to offer a better signal coverage and reduce the power consumption of each sensing node.

WSN plays a key role in the Internet of Things (IoT, Aoudia et al., 2018) due to its advantages of being low cost, having low power consumption, and being miniature in size. It has been widely used in many fields, including infrastructure monitoring, during the past decades. These advantages are mainly based on the microelectromechanical systems (MEMS) technology that provides low-power sensors. WSNs typically consist of multiple functional embedded systems, known as nodes and gateways. Most data acquisition and processing can be done by each node and communicated over a local network to a gateway. The network topology of a WSN is flexible and reliable due to alternative routes of data transmission being possible based upon the network configuration and communicating protocol.

A typical WSN node can be divided into four parts (BenSaleh et al., 2013): power supply subsystem, sensing subsystem, communication subsystem, and microcontroller unit (MCU), as shown in Figure 20(a). The power supply subsystem usually includes a power source, storage, and power management unit to control the current flow. The MCU is generally associated with built-in memory to store the operating firmware for data processing, performing tasks, and controlling other components in the node. Therefore, the MCU needs to be compatible with all protocols of each subsystem. When associating with analog sensors, although many MCUs have a built-in high resolution analog-to-digital converter (ADC), it is still common to have an ADC close to the sensors for reducing the noise and the voltage drop due to the wiring between sensors and ADC.

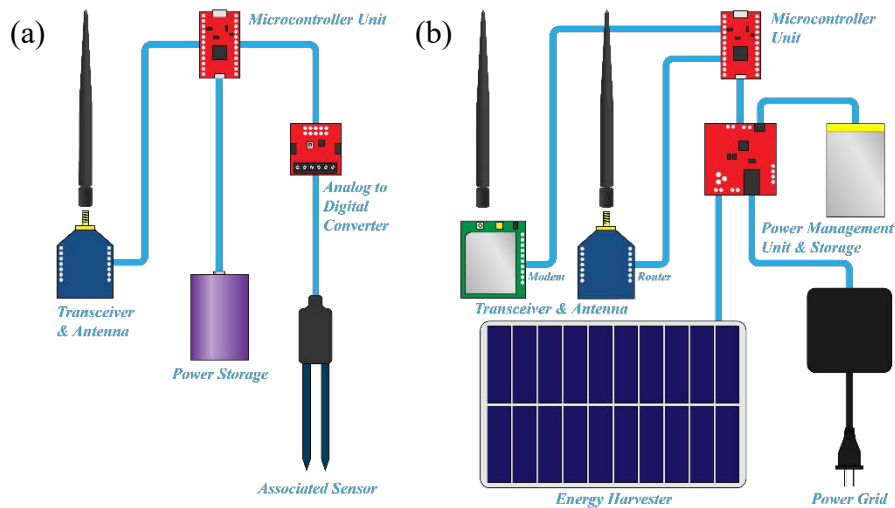
Some non-typical nodes are also commonly used, such as a gateway node, which has no sensing subsystem but with multiple communication subsystems instead, as shown in Figure 20(b). Gateway nodes may be implemented for local data aggregation and sending them to a remote host. It reduces both the power consumption and the fee of the cellular service and extends the coverage of the WSN. The architecture of a WSN node system may vary depending on the related application scenario.

Figure 19: WSN Instrumentations



(a) Aboveground (b) Underground Gas Pipeline Monitoring

Figure 20: Typical WSN System Architecture



(a) sensor node (b) gateway

Communication Protocols

The lifetime of the IoT applications is usually limited by its self-contained power source, which is constrained by the limited physical size (Gungor & Lambert, 2006). Much more power consumption is required by the transceiver compared to other components (Akyildiz et al., 2007). Therefore, low-power consumption becomes a common requirement of IoT communication technology. However, the conventional cellular communication technology (e.g., 2G, 3G, and 4G) tradeoffs the power and range for the high data rate, which is unnecessary for many civil engineering applications. Although the widely used short-range radio technologies (e.g., ZigBee and Bluetooth) operate with low-power consumption, they are

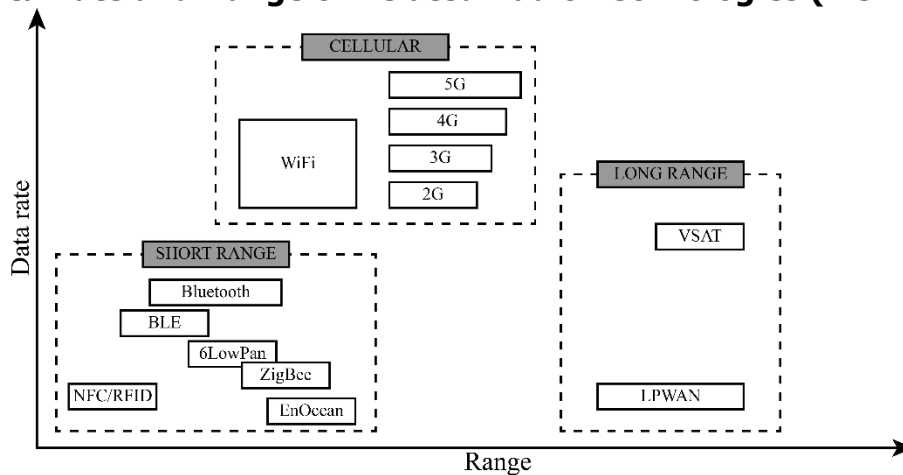
not suitable for scenarios that require long-range transmission. Therefore, the rapid growth of the IoT also significantly increased the research trend of low-power and long-range transmission technologies during the past decades.

Several commercial low-power wide-area networks (LPWAN) technologies are now used (e.g., LoRaWAN, NB-IoT, and Sigfox). Table 18 (Gaddam & Rai, 2018) shows the comparison of the current consumptions (proportional to power consumption) at transmit (TX), receive (RX), idle and sleep modes between cellular LTE, LoRaWAN, and NB-IoT. LPWAN can operate with a lower power consumption compared to cellular technology. However, cellular technology can communicate with a higher data rate which is optimal for applications that need high data rates, such as visual inspection. Figure 21 (Mekki et al., 2019) compares the data rate and transmission range between these technologies.

Table 18: Current Comparison in TX, RX, Idle and Sleep Modes (Gaddam & Rai, 2018)

| Technology | TX | RX | Idle | Sleep |
|------------|------------|---------------|--------|-------------|
| LoRaWAN | 24-44 mA | 12 mA | 1.4 mA | 0.1 μ A |
| NB-IoT | 74-220 mA | 46 mA | 6 mA | 3 μ A |
| LTE cat-M1 | 100-490 mA | Not specified | 9 mA | 8 μ A |

Figure 21: Data Rate and Range of Related Radio Technologies (Mekki et al., 2019)



LoRaWAN, Sigfox, and NB-IoT became the leading LPWAN technologies in the late 2010s (Mekki et al., 2019). Several comparisons among the three LPWAN technologies using different modulations have been reported (Silva et al., 2017; Mekki et al., 2019). Table 19 (Mekki et al., 2019) shows the overview of the three LPWAN technologies. In general, both Sigfox and LoRa have the advantages of better coverage and lower power consumption. Sigfox has the best coverage with the lowest power consumption. LoRa can also provide reliable communication with a higher speed than Sigfox. NB-IoT consumes additional energy because of the frequently synchronous communications and QoS handling, and its OFDM/FDMA access modes require a higher peak current than Sigfox and LoRa (Oh & Shin, 2017). However, NB-IoT has the

advantages of higher data rate and quality. Therefore, each technology is suitable for specific applications.

Table 19: Overview of the Several Commercial Low-power Wide-area Networks Technologies (Mekki et al., 2019)

| | Sigfox | LoRaWAN | NB-IoT |
|-----------------------------|---|---|--|
| Modulation | BPSK | CSS | QPSK |
| Frequency | Unlicensed industrial, scientific and medical (ISM) bands (915MHz in North America) | Unlicensed ISM bands (915 MHz in North America) | Licensed LTE frequency |
| Bandwidth | 100 Hz | 250 kHz & 125 kHz | 200 kHz |
| Max data rate | 100 bps | 50 kbps | 200 kbps |
| Bidirectional | Limited / Half-duplex | Yes / Half-duplex | Yes / Half-duplex |
| Max payload length | 12 bytes (upload), 8 bytes (download) | 243 bytes | 1600 bytes |
| Range (urban/rural) | 10 km / 40 km | 5 km / 20 km | 1 km / 10 km |
| Interference immunity | Very high | Very high | Low |
| Authentication & encryption | Not supported | Yes (Advanced Encryption Standard, AES 128b) | Yes (LTE encryption) |
| Adaptive data rate | No | Yes | No |
| Handover | End-devices do not join a single base station | End-devices do not join a single base station | End-devices join a single base station |
| Localization | Yes (Received Signal Strength Indicator , RSSI) | Yes (Time Difference Of Arrival, TDOA) | No |
| Allow private network | No | Yes | No |
| Standardization | Sigfox & ETSI | LoRa-Alliance | 3GPP |

Cybersecurity of Wireless Sensor Networks

The open communication environment of a wireless network offers a great convenience to reduce the infrastructure costs and give more flexibility of installation plan. However, it makes security a very important issue since anyone can access the wireless environment. Therefore, any communication within it can be easily intercepted, altered, or resent by an attacker (Radmand et al., 2010; Boubiche et al., 2021).

Conventional wireless devices use asymmetric encryption methods to prevent malicious attacks and surveillance. For example, Temporal Key Integrity Protocol (TKIP) and CTR mode with CBC-MAC Protocol (CCMP) encryption protocols of Wi-Fi Protected Access (WPA) under the IEEE 802.11i standard have been widely used for Wi-Fi.

However, asymmetric encryption requires enormous processing and send the public key frequently, which increases the power consumption significantly. Unlike conventional wireless devices, WSN devices are very small in size for easy deployment. As a result, its power and storage are very limited, as are its computational performance and data transfer to extend its battery life, which make asymmetric encryption unsuitable for WSNs.

Additionally, wireless sensor networks are often used in unattended areas, which means it may be physically stolen or damaged. These challenges make cybersecurity of WSN a serious concern, and the oil and gas industry is an attractive target for cyberattacks (Radmand et al., 2010). This section will introduce encryption methods, WSN security mechanisms and the potential cyberattacks.

Encryption

Since wireless network is an open communication environment, all sent messages can be received by everyone within the signal coverage as a broadcast, it is important to encrypt the message before sending it. Encryption can be understood as using a key to lock the message. The locked message is like a gibberish, its meaning cannot be deciphered. A key is required to unlock and access the hidden meaning in the message, and therefore only the desirable receives who own the keys can understand the hidden meaning of the locked message. The commonly used encryption mechanisms can be divided into two types: symmetric and asymmetric:

1. Symmetric encryption

Symmetric encryption is a type of encryption which uses the same secret key to both encrypt and decrypt the electronic information. A simple example is that the same key is required for locking and unlocking a safe, so both the sender who locks the letter into the safe and the recipient who unlocks and gets the letter from the safe must have a same key.

Practically, A (sender) share the secret key to B (recipient) through a safe way previously and use the secret key to encrypt the message and broadcast it through the wireless network. Both B and C received the encrypted message but only B has the secret key and can use it to decrypt the message. However, how A gives its secret key to B remotely and safely becomes a challenge.

2. Asymmetric Encryption

Asymmetric Encryption, also known as Public-Key Cryptography, is another type of encryption that the key used for encryption is different from the key used for decryption. The key used for encryption can not be used for decryption, so it is safe to be broadcasted to public without any encryption and therefore is known as public key. Only the recipient knows the key for decryption and will not share to anyone else even the sender, therefore it is known as private key. Anyone can use the public key published by the recipient to encrypt the message, but only recipient owns the private key and able to decrypt the encrypted message.

Practically, B (recipient) will first generate a set of keys including one public key and one private key, then broadcasts its public key without encryption through the wireless network. A (sender) uses B's public key to encrypt the message and broadcast it. B use its private key for decrypting the encrypted message broadcasted by A. C can only receive B's public key and A's encrypted message, and is unable to decrypt A's encrypted message since it doesn't have B's private key.

However, asymmetric encryption requires a lot of processing, causing communication delays, power consumption, and system resources. Therefore, in practice, asymmetric encryption is used only once at the beginning of a communication to establish a secure communication for sharing the secret key of symmetric encryption. The communication will then use symmetric encryption after the secret key has been safely shared to each other.

Therefore, the biggest contribution of asymmetric encryption is it successfully solved the biggest challenge of symmetric encryption: how to secure a safe remote way for sharing secret key. Most of the communications are using symmetric encryption. With either symmetric or asymmetric encryptions, the encrypted message cannot be cracked within a reasonable time (AES-128 would take about 2.61×10^{12} years to crack with the right quantum computer).

WSN Security Mechanisms

As mentioned above, asymmetric encryption requires a lot of processing and power, which makes it not suitable for WSN. Therefore, WSN usually use symmetric encryption mechanisms and pre-share the secret key before the deployment. The following methods are commonly used to secure the pre-shared key:

1. Backend interfaces that isolate the storage of root keys in the join server
2. Secure element solutions that provide additional hardware physical protection against tampering

The encryptions mechanisms used by the most popular Low-Power Wide-Area Network (LPWAN) wireless communication protocols that introduced in this report are shown as below:

1. LoRaWAN: AES 128 bit
2. NB-IoT/LTE-M: 3GPP 128-256 bit
3. Sigfox: AES 128 bit

Security Attacks in WSN

The potential cyberattacks methods on WSN have been revealed in some research (1,2,3), and can be categorized as:

1. Denial of service attack
2. Confidentiality and authentication attack
3. Data integrity attack

For WSNs that are protected by the above encryption mechanisms and whose keys have not been stolen, are well protected from most of the confidentiality, authentication and data integrity attacks, and some of the denial of service attacks. The rest of the cyberattacks that cannot be protected by encryptions including:

1. Physically stealing or damage – attacker may crack the encryption key
2. Jamming attack – interfere or disrupt the entire network
3. Denial of sleep attacks – waste the power of WSNs

Except the physically stealing may lead to the cracking of encryption key, other attacks only reduce the quality of the performance and the lifetime of the system. Most malicious attacks can be prevented by encryption mechanisms, so it is strongly recommended to select WSN devices with encryption feature.

Wireless Sensor Network Based Sensing Technologies

Although WSN technology is generally compatible with most electrical sensing technologies, it is still limited by the power consumption of the sensors since the nodes are usually deployed with a limited self-contained power source in most scenarios. Therefore, the associated sensors introduced in this section will focus on low-power sensors. Table 20 shows the overview of the WSN associable sensing technologies and the related events.

Table 20: Wireless Sensor Network Based Sensing Technologies and the Corresponding Events and Occasions

| TECHNOLOGIES | EVENTS | OCCASIONS |
|----------------------|-----------------------|----------------------|
| Soil moisture sensor | Leakage | Underground pipeline |
| Accelerometer | Leakage | All |
| Strain gauge | Deformation | All |
| Position sensor | Relative displacement | Aboveground pipeline |
| *Flow sensor | Leakage | All |
| *Gas sensor | Leakage | Mostly aboveground |

*Will be introduced in other sections.

Soil moisture sensor

The commonly used soil moisture sensing methods including: Frequency Domain Reflectometry (FDR), Time Domain Reflectometry (TDR), capacitance and resistance methods.

The resistance method determines soil moisture by measuring the resistance of the soil between two electrodes. The resistance decreases when increasing the amount of the water since the ions in the water can increase the electrical conductivity. However, the number of ions in the water is not constant even when the amount of water has not changed due to the polarized ions, and will be changed according to the soil type. Therefore, although resistance sensors are extremely cheap, the precision error can be large.

FDR, TDR and capacitance sensors are known as dielectric sensors, which measure the charge capacity of the soil. With the proper measurement frequency and circuit design, dielectric sensors can polarize water molecules without polarizing dissolved ions. TDR sensor measures the travel time of the reflected waves of electrical energy along the sensing wire, which is related to the adjacent soil and the volumetric water content. FDR and capacitance sensors are similar technologies; they use soil as a capacitor. Capacitance sensors determine the volumetric water content by measuring the soil charge storing capacity. FDR sensors measure the maximum resonant frequency in the circuit and relate the resonant frequency to the water content. However, the hardware of TDR is more expensive and has high power consumption. Other methods such as neutron probe and COSMOS are also costly and require high power, which are not suitable in most cases. FDR and capacitance sensors have a lower cost compared to other methods except for the resistance methods. Studies show both TDR and capacitance to be equally accurate with calibration. Therefore, FDR and capacitance sensors are most suitable for WSN applications. The industrial FDR (Figure 22) and capacitance sensors typically have an accuracy of $\pm 3\%$, measuring range from 0% to 70% and resolution of 0.1% for volumetric water content measurement with a typical operating temperature range from $-40\text{ }^{\circ}\text{C}$ to $60\text{ }^{\circ}\text{C}$.

Figure 22: FDR Soil Moisture Sensor – METER Environment EC-5 (METER Environment)



Accelerometer

Accelerometer has been used for pipeline monitoring as a leakage detector by measuring the acoustic signal induced by the leakage. It can also offer local ground acceleration measurement, which is known as an important index for assessing pipeline failure due to the ground displacement during the earthquake hazard (Task B). For example, Pacific Gas & Electric (PG&E) intends to replace more than 300,000 electric SmartMeter units across the Bay Area with Next Generation Meters (NGMs) equipped with accelerometers that can detect subtle motions of the ground. With the cooperation of the Energy Geosciences Division of Berkeley Lab, the high-resolution, regionally specific seismic big data captured and collected by NGMs can be used for developing a modern computational framework for quantifying ground motion based on full physics simulations on a regional scale.

Accelerometers can be divided into three main types: Capacitive, Piezoresistive, and Piezoelectric. Capacitive and piezoresistive are DC-response accelerometers and can be fabricated with MEMS technology. MEMS accelerometers are often produced as surface-mount devices (SMDs) to be directly mounted to printed circuit boards (PCB) due to their small size and the DC-response, which also make them more easily to be integrated into the system. DC-response accelerometers can measure down to 0 Hz, making them best suited for measuring low-frequency vibration, motion, and steady-state acceleration.

Capacitive accelerometers (Figure 23) are the least expensive MEMS accelerometers. They convert the acceleration into capacitance changes by utilizing the displacement of a seismic mass between two fixed electrode plates changed due to the acceleration. They also have low power consumption, which makes them popular in mobile devices and other electronic devices such as health monitoring devices. However, capacitive accelerometers typically suffer from poor signal-to-noise ratio and limited dynamic range. Other disadvantages include limited bandwidth (mostly a few hundred Hertz's) and restricted to smaller acceleration (typically <200 g).

Piezoresistive accelerometers (Figure 24) convert the acceleration into the resistance by using a seismic mass hanging by a set of four bridges attached with piezo resistors. Piezoresistive accelerometers generally have an outstanding signal-to-noise performance due to their differential and purely resistive outputs. They also have a wide bandwidth (up to 7,000 Hz) which can be used for measuring short-term high frequency and high g levels (up to 10,000 g) shock events, such as crash testing and weapon testing. They can also be used for calculating the integrated velocity or displacement due to their DC-response. However, piezoresistive accelerometers typically have poor sensitivity makes and are sensitive to temperature (usually comes with build-in temperature compensation). Although piezoresistive accelerometers are also fabricated by using MEMS technology, they are much more expensive compared to the capacitive accelerometers.

Similar to the other types of accelerometers, piezoelectric accelerometers (

Figure 25) act upon a seismic mass that is restrained by a cantilever beam and over a piezoelectric element. The seismic mass loads the piezoelectric element when the sensor senses the vibration, and the piezoelectric element converts the physical force into an electric signal. Two types of electrical signal output are used: charge and voltage. Both are AC-response, which is not suitable for measuring static or very low frequency (<1 Hz) acceleration or integrating for velocity or displacement measurements.

Charge mode piezoelectric accelerometers are the most durable accelerometers due to their high tolerance to environmental conditions, including extreme temperature ranges (from -200 °C to +640 °C). A charge amplifier will be needed for reading the output from the charge mode piezoelectric accelerometers, which makes the system more complicated.

Voltage mode internal electronic piezoelectric (IEPE) accelerometers are the most commonly used accelerometer type for industrial applications. They are basically the charge mode piezoelectric accelerometers integrated with a build-in charge amplifier, making them easily integrated. However, the included circuit for the build-in charge amplifier limits their environment tolerance and can be typically operated from -40 °C to +125 °C.

Figure 23: Capacitive Accelerometer – Analog Devices EVAL-ADXL335 (Analog Devices)

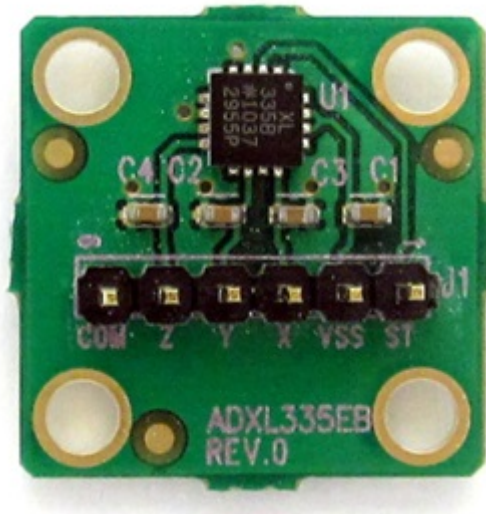


Figure 24: Piezoresistive Accelerometer – Endevco 35B-2 (Endevco)



Figure 25: Piezoelectric Accelerometer – PCB Piezotronics 350B43 (PCB Piezotronics)



Strain gauges

Strain gauges can be divided into many types, such as photoelectric, bonded metallic wire, thin-film, semiconductor (piezoresistive), and vibrating wire. Semiconductor (

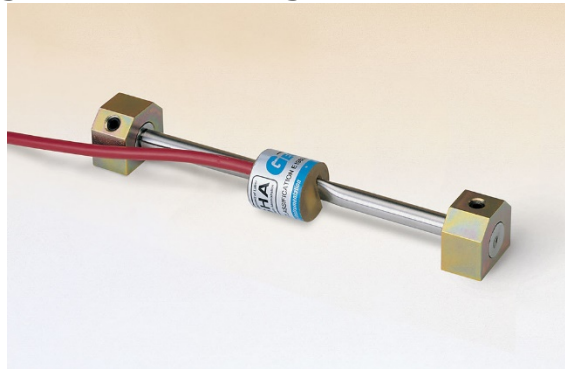
Figure 26) and vibrating wire (Figure 27) are the most commonly used strain gauge for strain measuring. Semiconductor strain gauges measure the change in electrical resistance depending on silicon or germanium's piezoresistive effects. It uses an electrically conductive material that resistance changes with dimensional changes when the conductor is deformed elastically. Usually, a Wheatstone bridge is used to convert this change in resistance to a voltage output and provide self-temperature compensation. Semiconductors typically have a measuring range from -4000 to +5000 $\mu\epsilon$ with a resolution of 0.125 mV/V. In general, semiconductor strain gauges are recommended for dynamic measurements.

Vibrating wire sensor has been widely used by the civil engineering industry due to its long-term stability in adverse environments and can be transmitted over cables as long as 2 km without appreciable degradation of the signal. The advantages mainly lie in its frequency output rather than voltage, which will be varied rapidly due to the resistance of the cable arising from the water penetration, temperature fluctuations, contact resistance, or leakage to the ground. Vibrating wire sensor typically has a resolution of about 0.0001% to 0.00125% FS and an accuracy of about 0.5% FS. However, a vibrating wire sensor typically has a lower measuring frequency (about 2 Hz) than other conventional strain gauges and transducers, which is usually acceptable for most geotechnical engineering applications.

Figure 26: Embedment Semiconductor Strain Gauge – GEOKON Model 3900 (GEOKON)



Figure 27: Vibrating Wire Strain Gauge – GEOKON Model 4000 (GEOKON)



Contact position sensor

Position sensors are used for indicating the absolute or relative mechanical position (displacement) measurements. There are many types of position sensors with different measuring ranges. The commonly used contact position sensors for general measuring range including linear variable differential transformer (LVDT), linear potentiometer and draw-wire sensor.

The LVDT (Figure 28) is well known for its durability, high sensitivity (typically 100 mV/mm), and absolute linear distance measurement. It can be designed to operate at cryogenic temperatures or up to 650 °C, in harsh environments and under high vibration and shock levels (can up to 500g). LVDT measures displacement using three solenoidal coils placed end-to-end around a cylindrical ferromagnetic core attached to the object whose position is to be measured. An AC drives the middle coil with a typical frequency from 1 to 10 kHz. The induced voltage between the other two coils changes due to the movement of the core, which can be converted into displacement of the core. However, the AC input required for the LVDT makes the sensing system much more complicated. It has high power consumption and a limited maximum range (typically from 0.5 to 500 mm).

Linear potentiometer (Figure 29) is another linear displacement transducer similar to LVDT. Both of them measure displacement in a linear fashion with a fast response and high reliability. Potentiometer is a three-terminal resistor with a sliding or rotating contact forming an adjustable voltage divider. It converts the displacement into resistance by using movable

contact. LVDTs use a nickel-iron core surrounded by coils and determine the voltage change inside the coils. The magnitude of the output AC signal, which represents the relative movement between the center nickel-iron core and the outside coils. This contactless design avoids the mechanical wear of the components, which gives LVDTs a very high operational life. However, the AC signal outputs makes LVDTs more difficult to be integrated with data logger, and the price of LVDTs are significantly higher than potentiometers. Therefore, potentiometers are more commonly associated with WSN than LVDTs. Compared to LVDTs, potentiometers generally have a similar measuring range (typically from 10 to 1000 mm) with lower data qualities, including resolution, repeatability, linearity, etc.

Draw-wire sensor (Figure 30) measures distance using a rigid wire connecting the object and the sensor and converts the measured rotary by a built-in encoder. Draw-wire sensors can measure almost linearly across the entire measuring range and are used for distance and position measurements of 50mm up to 50,000mm. It is low cost. It is also robust and has a selectable resolution. However, unlike LVDT, the draw-wire sensors use a relative measurement. It needs to be continuously measured and may result in high power consumption.

Figure 28: LVDT – GEOKON Model 1450 (GEOKON)



Figure 29: Linear Potentiometer– GEOKON Model 1500 (GEOKON)



Figure 30: Draw-wire Sensor – TE Connectivity Measurement Specialties SP1-50 (Digi-Key)



Non-contact position sensors

Non-contact position sensors detect distance or presence of nearby objects without any physical contact by outputting a signal (e.g., laser, IR LED, ultrasonic wave) and reading the change of the returned signal. The four most commonly used technologies for general distance measuring include ultrasonic, infrared light-emitting diode (IR-LED), light detection and ranging (LIDAR), and vertical-cavity surface-emitting laser (VCSEL).

Ultrasonic range finders (Figure 31) measure distance using ultrasonic waves emitted from their head and reflected when the waves reach the object. The distance to the object can then be calculated by measuring the time between the emission and reception. Ultrasonic range finders have the advantages of very low power consumption and multiple interfaces, making them easily integrated. They typically have a low measuring range of 0.3 to 5 m. They have a poor resolution (usually about 10-25 mm, some can lower to 1 mm) and sampling rate (≤ 8 Hz).

IR-LED distance sensors (Figure 32) are the most popular proximity sensor due to their very low cost. Like ultrasonic range finders, they measure the distance using IR light instead of the ultrasonic wave. It has the advantages of high resolution (less than 10 mm), decent sampling rate (typically 100 Hz), multiple interfaces and a small footprint. However, it comes with the disadvantages of high power consumption and a fairly low maximum measuring range (less than 12 m).

LIDAR sensors are well known for their high performance in measuring distance. They measure distance by illuminating the target with laser light and measuring the returning times and wavelength changes from the reflection. They can also be used for making 3-D representations of the target. Several low-power LIDAR sensors (

Figure 33) are in the IoT markets associated with WSN technology. These “lite” LIDAR sensors typically have the advantages of excellent maximum range (typically more than 40 m and can up to 180 m), high resolution (less than 10 mm), and high sampling rate (up to 1 kHz). However, they have the disadvantages of very high power consumption, very high cost, and large footprint area.

VCSEL sensors (Figure 34) have been widely used for applications including computer mouse, fiber optic communication, laser printer, Face ID, and smartglasses. They are low-cost sensors. They use a semiconductor laser diode with laser emission perpendicular to the top surface. The perpendicular laser beam also allows multiple VCSEL units to operate simultaneously to get better efficiency, which reduces the power consumption and increases its bandwidth. VCSEL sensors typically have an excellent resolution (less than 1 mm), a very low maximum range (less than 4 m), and a compact size.

Figure 31: Ultrasonic Range Finder – MaxBotix XL-MaxSonar-WR/WRC (MaxBotix)



Figure 32: Infrared Proximity Sensor – Sharp GP2Y0A41SK0F (Sparkfun)



Figure 33: Lite LiDAR Module – Benewake TF03 (Sparkfun)



Figure 34: VCSEL sensor – STMicroelectronics VL53L1X (STMicroelectronics)



In-line Inspection Technologies

Introduction to Inspection Technologies

Pipeline inspection technologies include external and internal inspection technologies. These technologies are normally carried out through non-destructive testing (NDT) technologies. Magnetic flux leakage (MFL) and ultrasonic testing (UT) are the most popular NDT for internal pipeline inspection. The internal inspection is more likely to be used for underground and offshore pipelines since the pipeline is almost unreachable. The internal inspection is also known as in-line inspection (ILI), typically carried out using different types of inspection tools designed to carry multiple sensors and travel in the pipeline. The equipped sensors will gather the pipeline information during the carrier traveling through the pipeline, such as internal mapping, deformation, etc. The most popular ILI tool is smart (or intelligent) PIG. Since the inspection can be done during pigging, no further effort is required. There are also some commonly used internal inspection technologies, such as robots.

This chapter will introduce the commonly used ILI tools: smart PIG, and the widely used inspection technologies for ILI, including magnetic flux leakage and ultrasonic testing.

Smart PIG

Pigging means the practice of using pigs or scrapers to perform various maintenance operations, including inspecting and cleaning inside of the pipeline, which is done without stopping the flow in the pipeline. The pig will be inserted into a pig launcher (Figure 35), which is a large section in the pipeline and gradually reduces to the normal diameter along the launching direction. The launcher is then closed, and the pressure-driven flow in the pipeline is used to push the pig along down the pipe until it reaches the pig catcher.

Pigs can be equipped with various electronics and sensors for collecting information during it pigging through the pipeline, which are known as intelligent or smart pigs. The associate sensing technologies vary and depend on the intended use and the manufacturer. Table 21 shows the commonly used associate sensing technologies and related applications, also the additional supporting measurements. Some smart pigs may use a combination of these technologies, as shown in Figure 36.

The smart pigs use onboard batteries for powering the associated electronics and use either analog tape, digital tape, or onboard memory for data recording. All electronics are sealed to prevent leakage of the pressured inline liquid. The specific material may be applied against the highly basic or acidic, or extremely high pressure and temperature because the pipeline specifications vary dramatically depending on the specific purpose and fluid material. The available operating specifications play an important role when selecting the smart pig. Table 22 shows the common operating specifications of a smart pig.

Table 21: Associable Sensing Technologies for Smart PIG

| TECHNOLOGY | APPLICATION |
|-----------------------------|--|
| Magnetic Flux Leakage (MFL) | Surface pitting, corrosion, cracks and weld defects detection (for steel/ferrous pipelines only) |
| Ultrasonic | Cracks, coating and lamination defects detection |
| Caliper | Bending and other deformations |
| Temperature Sensor | Providing the indication of the likely type of debris present |
| Odometer | Providing the travel distance of the pig |
| Orientation Sensor | Providing the travel direction of the pig |
| Vibration Sensor | Providing position fixing at each joint |

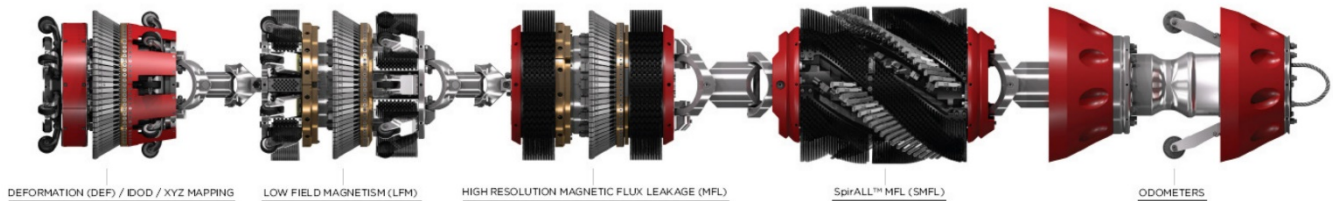
Table 22: Typical Operating Specification of Smart PIG

| TERM | DEFINITION |
|-------------------------|--|
| Tool sizes | The diameter of the available pipeline. |
| Fluid types | The fluid types of the pipeline product. |
| Temperature range | The operating fluid temperature. |
| Pressure range | The operating fluid pressure. |
| Speed range | The operating speed of the tool. |
| Fluid flow range | The operating fluid flow speed. |
| Mini bend radius | Mini available turning radius of the pipeline. Expressed by divide the turning radius by pipe's diameter (D). |
| Wall thickness range | The available pipeline wall thickness. |
| Max working hours | Max operating hour of the tool, which depends on tool's battery & memory |
| Max inspection distance | Max available inspection distance, which depends on max working hours & max operating speed. Needs to be longer than the distance from the launcher to the receiver. |

Figure 35: PIG Launcher & Receiver (Sagebrush)



Figure 36: T.D. Williamson Multiple Dataset (MDS) system (T.D. Williamson)



Some of these technologies have different performances in different direction. Figure 37 (Vanaei et al., 2017) shows the performances of each technology when detecting different geometries of defects, where the

A: Wall thickness or 10 mm (0.39”), whichever value is greater.

L: Wall length (in axial direction)

W: Wall width (in circumferential direction)

For example, axial MFL (as shown as the red dot-line in Figure 37) has a very good sensitivity in circumferential direction but bad sensitivity in axial direction. Therefore, axial MFL can sense the defects with very small L/A (as small as 10mm), e.g. circumferential slotting, but cannot sense the defects with very small W/A, e.g. axial slotting. Also, for the anomalies of pipe itself, different anomalies usually result in different geometries of defects. Table 23 shows the commonly used ILI technologies and their capabilities for determining different types of anomalies, where the symbol

O: Able to detect with a good performance

Δ: Limited detecting ability (such as low sensitivity or limitation applied)

X: Unavailable

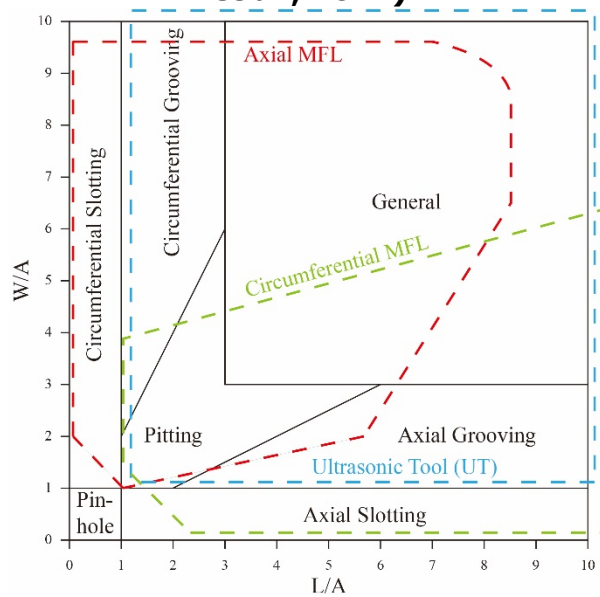
, which according to the most likely geometries of the anomalies and the performances of the technologies in different directions. The details of each technology will be introduced in the following sections.

The outputted data interpretations of smart pigs rely on the operator’s experience. Therefore, directly purchasing the service from ILI company is strongly recommended.

Table 23: Inspection Technologies and Related Anomalies (T.D. Williamson)

| TECHNOLOGY | Coating & lamination | Mill | Construction -weld | Construction | Geological -force | Metal loss | Crack |
|-------------|----------------------|------|--------------------|--------------|-------------------|------------|-------|
| Axial MFL | O | O | Δ | Δ | X | O | Δ |
| Spiral MFL | O | O | O | Δ | X | O | O |
| Ultrasonic | O | Δ | O | X | X | Δ | O |
| Mapping | X | X | X | Δ | O | X | X |
| Deformation | X | X | Δ | O | O | X | X |

Figure 37: Different ILI tool capabilities in determining corrosion features (Vanaei et al., 2017)



Magnetic Flux Leakage

Magnetic flux leakage (MFL) is one of the most popular pipeline inspection methods. It is one of the Non-Destructive Testing (NDT) methods for detecting metal loss caused by corrosion, pitting, etc., in ferrous metal structures, most commonly pipelines and storage tanks. The basic principle of MFL is using a strong magnetic field to magnetize the ferrous metal object to saturation level. The magnetic flux will be disturbed if there is corrosion or missing metal, causing a leakage field. A magnetic sensor is placed between the poles of the MFL to detect this leakage field. The chart record of the leakage field can be used for identifying damaged areas and estimating the depth of missing metal.

One of the limitations of MFL is the poor sensitivity when detecting the material discontinuity on its magnetic flux direction. Therefore, there are mainly two types of MFL with different magnetic field orientations: (a) Axial – MFL-A (also known as the traditional MFL), and (b) Circumferential – MFL-C (also known as transverse field inspection, TFI).

The MFL-A produces a axial magnetic flux field in axial direction of the pipeline (Figure 38, ROSEN Group). The magnetic flux will be disturbed if there is a defect on its path. The magnetic flux will be measured by the receivers and the defects can then be determined. The magnetic flux will only be disturbed when it pass through the defects, which means that the dimension of the defect that perpendicular to the magnetic flux dominates the sensitivity, as shown as Figure 39 (Ho et al., 2010). Therefore, MFL-A is suitable for detecting circumferentially-oriented features and general corrosion, but it has poor sensitivity in the axial direction (see the left side of Figure 39). In contrast to MFL-A, MFL-C produces and detects circumferential magnetic flux (

Figure 40, ROSEN Group), which makes it suitable for detecting axially-oriented features including long seam defect detection and narrow corrosion, channeling, crack-like features, and preferential seam weld corrosion. But it has poor sensitivity in the circumferential direction (see the right side of Figure 39). Figure 41 (Pipeline Operators, 2021) shows the definitions of metal loss feature dimension parameters including width, length and depth, which are often used in ILI sensor specification that related to metal loss detecting ability. The start point (S), end point (E), deepest point and each threshold are used in inspection reports to express the defects and suggest for the maintenance decision.

Figure 38: Magnetic Fields Generated by MFL-A (ROSEN Group)

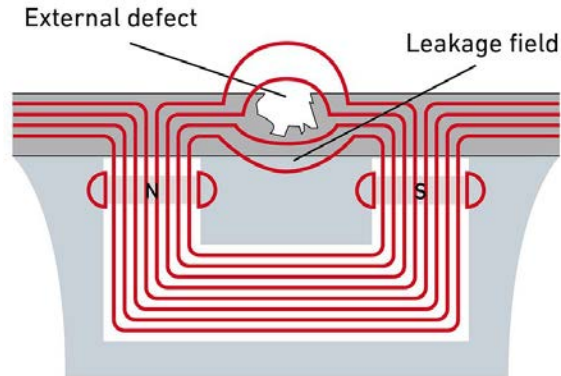


Figure 39: Direction of Defects with Respect to MFL-A and MFL-C (Ho et al., 2010)

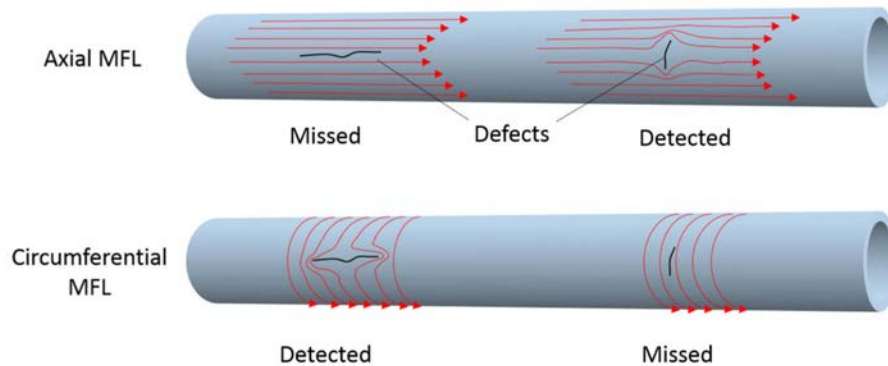


Figure 40: Magnetic Fields Generated by MFL-C (ROSEN Group)

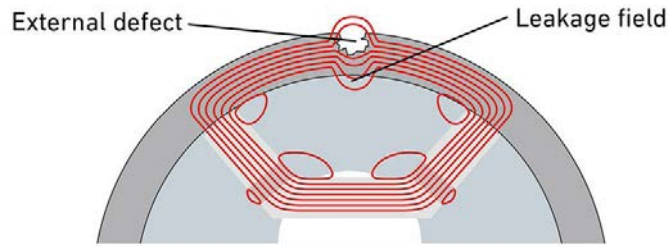
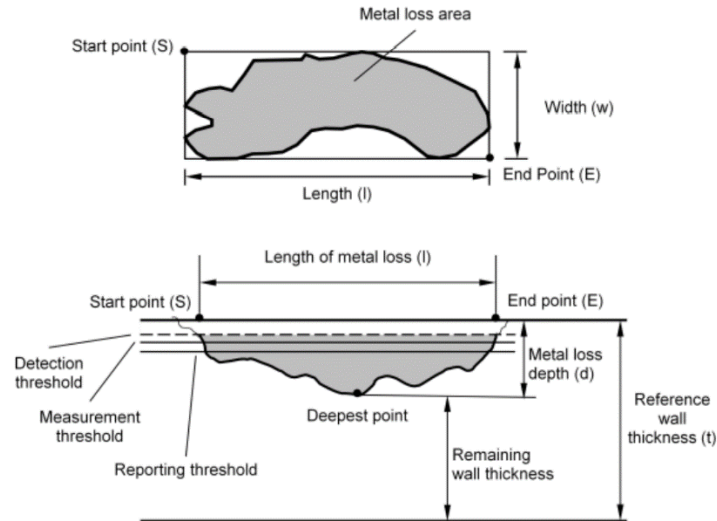


Figure 41: Parameters Describing Dimension of Metal Loss Feature (Pipeline Operators, 2021)



There is also tri-axial MFL, which is very similar to MFL-A. Tri-axial MFL produces axial magnetic flux, and it is capable of accurately detecting flux leakage in the axial, transverse/circumferential and radial directions. With extra sensors, tri-axial MFL is suitable for sizing complex features compared to the other two types of MFLs. However, it still has poor axial sensitivity since it only uses an axial magnetic field. Its operating hours are usually less than the other two types of MFL since more measurements need to be recorded.

Table 24 shows the specifications of commercially available MFL pigs by ROSEN Group. Figure 42 shows a photo of an MFL-A pig manufactured by Enduro Pipeline Services. T.D. Williamson has a SpirALL Magnetic Flux Leakage (SMFL, Figure 43) equipped pig, which generates a magnetic field in spiral directions with the combination of MFL-A and MFL-C.

Figure 44 (ROSEN Group) shows a photo of a tri-axial MFL pig manufactured by ROSEN Group.

Table 24: Typical specification of magnetic flux leakage (ROSEN Group)

| MFL TYPE | MFL-A | MFL-C | TRI-AXIAL | |
|--|------------------------------|------------------------------|------------------------------|-------|
| Operating Specifications | | | | |
| Tool sizes | 3"-56" | 6"-56" | 6"-56" | |
| Fluid types | Gas or liquids | Gas or liquids | Gas or liquids | |
| Temperature range | 0 °C–65 °C (14 °F–149 °F) | 0 °C–65 °C (14 °F–149 °F) | 0 °C–65 °C (14 °F–149 °F) | |
| Pressure range | Up to 25 MPa (3625 psi) | Up to 25 MPa (3625 psi) | Up to 25 MPa (3625 psi) | |
| Speed range | Up to 5.0 m/s (11.2 mph) | Up to 4.0 m/s (8.9 mph) | Up to 3.0 m/s (6.7 mph) | |
| Fluid flow range | Up to 12 m/s (26.8 mph) | Up to 11 m/s (24.6 mph) | - | |
| Mini bend radius | 1.5D | 1.5D | 1.5D | |
| Wall thickness range | 4–32 mm (0.15"–1.26") | 4–25 mm (0.15"–1.00") | 4–25 mm (0.15"–1.00") | |
| Max working hours | 400 hours | 400 hours | 100 hours | |
| Max inspect distance | 800 km (500 miles) | 800 km (500 miles) | 200 km (125 miles) | |
| Location and Orientation Capabilities | | | | |
| Axial position accuracy | 1:1000 | 1:1000 | 1:1000 | |
| Axial position from closest weld | ±0.1 m (±3.9") | ±0.1 m (±3.9") | ±0.1 m (±3.9") | |
| Circumferential position accuracy | ±5° | ±5° | ±5° | |
| Wall Thickness Detection Capabilities | | | | |
| Wall Thickness accuracy (POD=80%) | ±1 mm (±0.04") or ±0.1t | ±1 mm (±0.04") or ±0.1t | ±1 mm (±0.04") or ±0.1t | |
| Sizing Capabilities | | | | |
| Depth accuracy (POD=90%) | General | 0.10t | 0.15t | 0.10t |
| | Pitting | 0.10t | 0.15t | 0.10t |
| | Axial grooving | 0.10t | 0.10t | 0.10t |

| | | | | |
|--|--------------------------|----------------|----------------|----------------|
| | Circumferential grooving | 0.10t | 0.20t | 0.10t |
| Depth sizing accuracy (POD=80%) | General | ±0.10t | ±0.15t | ±0.10t |
| | Pitting | ±0.10t | ±0.19t | ±0.10t |
| | Axial grooving | ±0.15t | ±0.15t | ±0.15t |
| | Circumferential grooving | ±0.10t | ±0.15t | ±0.10t |
| Length sizing accuracy (POD=80%) | General | ±15 mm (0.59") | ±15 mm (0.59") | ±15 mm (0.59") |
| | Pitting | ±10 mm (0.39") | ±12 mm (0.47") | ±10 mm (0.39") |
| | Axial grooving | ±10 mm (0.39") | ±15 mm (0.59") | ±10 mm (0.39") |
| | Circumferential grooving | ±10 mm (0.39") | ±15 mm (0.59") | ±10 mm (0.39") |
| Width sizing accuracy (POD=80%) | General | ±15 mm (0.59") | ±15 mm (0.59") | ±15 mm (0.59") |
| | Pitting | ±12 mm (0.47") | ±15 mm (0.59") | ±12 mm (0.47") |
| | Axial grooving | ±12 mm (0.47") | ±15 mm (0.59") | ±12 mm (0.47") |
| | Circumferential grooving | ±12 mm (0.47") | ±15 mm (0.59") | ±12 mm (0.47") |
| *Abbreviations: POD = Probability of Detection; t = wall thickness | | | | |

Figure 42: MFL-A Pig (Enduro Pipeline Services)

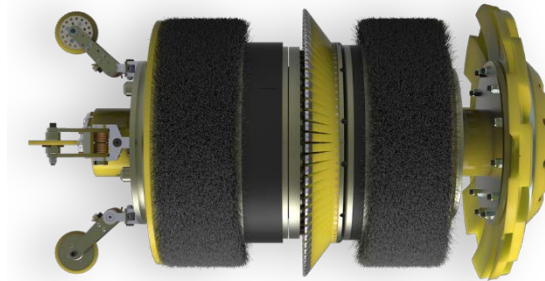


Figure 43: SMFL Pig (T.D. Williamson)

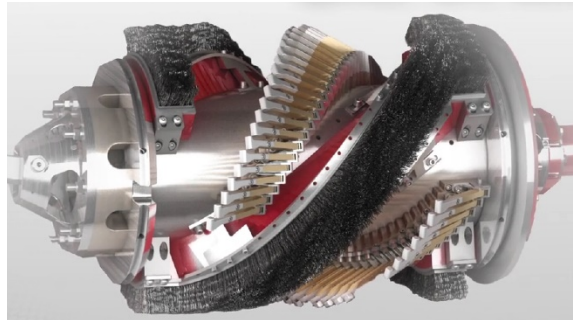
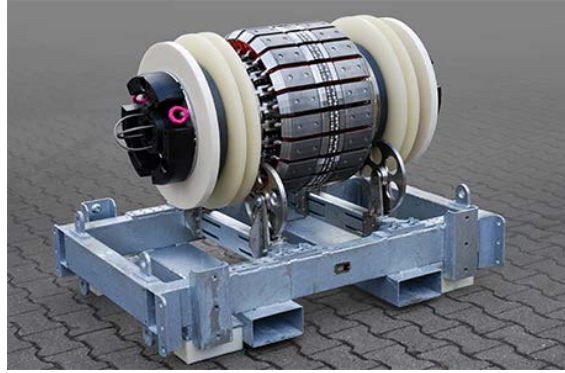


Figure 44: High-resolution Tri-axial MFL Pig (ROSEN Group)



Ultrasonic Testing

Ultrasonic testing (UT) techniques are a family of non-destructive testing (NDT) techniques that are used to detect internal flaws or to characterize materials in engineering components based on the propagation of ultrasonic waves in the object or material tested. Ultrasonic thickness measurement (UTM) is a widely used technique for measuring the thickness of a material from one side. It has a transducer that sends out a short ultrasonic wave pulse. When the wave encounters an interface, a part of the pulse is reflected, while the remainder enters into the interface. Therefore, there may be multiple reflected pulses. These reflected pulses are captured precisely by ultrasonic sensors and converted into the distance by multiplying the flight time with the speed of sound of the medium. The calculated distances divided by two mean the distances from the source to each interface that causes the reflection. For example, Figure 45 (Barbian et al., 2011) shows the principle of the UTM. The ultrasonic probe will send an ultrasonic pulse toward the pipe wall. The distance from probe to inner wall is called stand-off (as shown as t_1 in Figure 45), which can be determined by the following formula:

Equation 6

$$t_1 = \frac{T_1 \times V_m}{2}$$

where the

t_1 : Stand-off, the distance from probe to inner wall

T_1 : The time between sending the pulse to receiving the first reflected pulse

V_m : The speed of the sound in the coupling medium

Every received reflected ultrasonic pulses after the first one mean the interfaces of the defects except the last one, which means the outer wall of the pipe. In the case of Figure 45, there is no defect between the inner and outer walls. Therefore, the wall thickness can be determined by the following formula:

Equation 7

$$t_2 = \frac{(T_2 - T_1) \times V_p}{2}$$

where the

t_2 : Wall thickness

T_2 : The time between sending the pulse to receiving the last (second in this case) reflected pulse

V_p : The speed of the sound in the pipe medium

The anomalies can then be identified by looking for the changes of the calculated t_1 and t_2 as shown as the lower part of Figure 45. The locations of the defects can be told by x-axis, which is the travel distance of the PIG measured by the associated odometer.

Figure 46 (Pipeline Operators, 2021) shows the definitions of crack and crack-like feature dimension parameters including length and depth, which are often used in ILI sensor specification that related to crack and crack-like features detecting ability. The start point (S), end point (E), crack angel between pipe axis, deepest point and each threshold are used in inspection reports to express the defects and suggest for the maintenance decision.

Figure 45: Ultrasound Principle for Wall Thickness Measurement (Barbian et al., 2011)

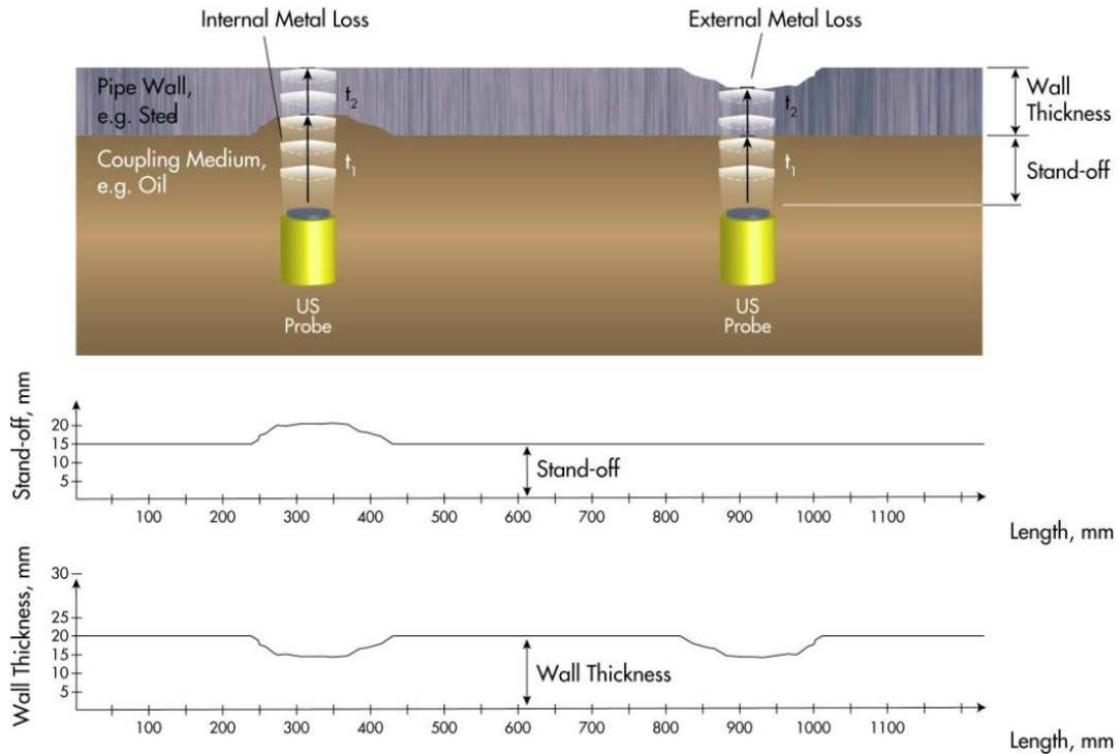
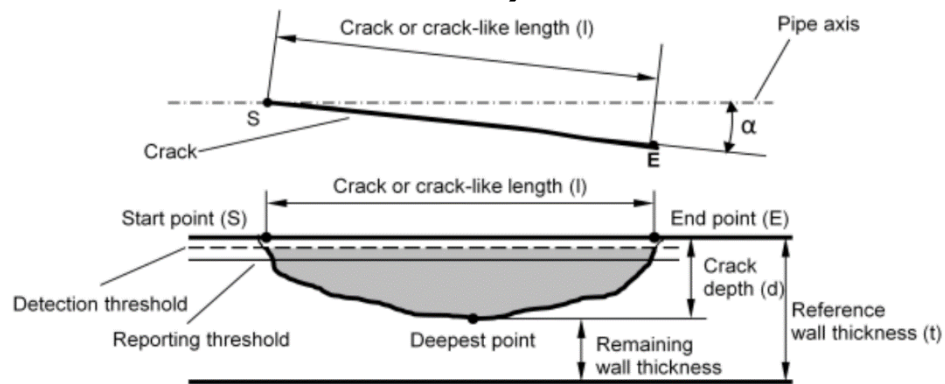


Figure 46: Illustration (top view and cross section) of Parameters Describing Location and Dimension of Crack and Crack-like Features (Pipeline Operators, 2021)



The ultrasonic testing gauges can be divided into two types depending on their built-in ultrasonic wave sources: (a) Piezoelectric (Figure 47, ROSEN Group) and (b) Electromagnetic acoustic transducer (EMAT, shown as the left six pigs in Figure 48, Baker Hughes). A piezoelectric transducer is often used to generate ultrasonic sound sources. An AC voltage input makes them oscillate and produce ultrasonic sound. EMAT is another means of inducing ultrasound waves, which generates all kinds of waves in metallic and/or magnetostrictive materials without any contact based on electromagnetic mechanisms. EMAT use AC current in the electric coil to generate eddy current on the surface of the material and result in a dimensional change which called magnetostriction. The disturbances caused by magnetostriction then propagate in the material as an ultrasound wave.

Both piezoelectric and EMAT need to be calibrated with the speed of sound of the target materials. The difference between them are the ability of performing measurement over rust and the requirement of the coupling materials. When using piezoelectric, the ultrasonic pulse is sent from the probe on the PIG, any gaps will result in the bad propagation of the ultrasonic pulse. Therefore, rust need to be removed before the measurement to make sure there is no gaps between the rust and wall. The coupling material needs to be applied between the probe and the wall to fill the gap between the probe to the wall. These are not required for EMAT since it generates the ultrasonic pulse remotely and directly on the wall. Therefore, EMAT provides more convenience compared to piezoelectric. Although EMAT is very convenient, it has the disadvantages of sophisticated signal processing and bigger in size, and most of all, it can only be used for the pipes that made by metallic or magnetic materials.

Table 25 concludes the above and shows the comparisons between piezoelectric and EMAT.

Table 26 (ROSEN Group) lists some specification examples of market available UT ILI tools. As mentioned above, EMAT has a relative limited size availability compared to piezoelectric.

Table 25: Comparisons of different types of ultrasonic inspection

| TECHNOLOGY | ADVANTAGES | DISADVANTAGES | OCCASIONS |
|-------------------|--|---|---|
| Piezoelectric | Available for most material | Couplant required, cannot measure over rust, sensitive to surface condition | Well surface condition and couplant is available |
| EMAT | Less sensitive to surface condition, easier deployment, dry inspection | Sophisticated signal processing, limited to metallic or magnetic products, size constraints | Metallic or magnetic products with bad surface condition or couplant is unavailable |

Table 26: Typical specification of ultrasonic inspection (ROSEN Group)

| ULTRASONIC TYPE | | PIEZOELECTRIC | EMAT |
|--|-----------------|-------------------------------|------------------------------|
| Operating Specifications | | | |
| Tool sizes | | 6"–56" | 12"–48" |
| Fluid types | | Liquids | Gas or liquids |
| Temperature range | | 0 °C–65 °C (14 °F–149 °F) | 0 °C–65 °C (14 °F–149 °F) |
| Pressure range | | Up to 25 MPa (3625 psi) | Up to 15 MPa (2175 psi) |
| Speed range | | Up to 2.5 m/s (5.59 mph) | Up to 2.5 m/s (5.59 mph) |
| Fluid flow range | | Up to 8 m/s (17.9 mph) | Up to 8 m/s (17.9 mph) |
| Mini bend radius | | 1.5D | 1.5D |
| Wall thickness range | | 5–45 mm (0.19–1.77") | Up to 20 mm (0.79") |
| Max working hours | | - | 50 hours |
| Max inspect distance | | - | 330 km (205 miles) |
| Location and Orientation Capabilities | | | |
| Axial position accuracy | | 1:1000 | 1:1000 |
| Axial position from closest weld | | ±0.1 m (±4") | ±0.1 m (±4") |
| Circumferential position accuracy | | ±10° | ±10° |
| Wall Thickness Detection Capabilities | | | |
| Wall Thickness accuracy (POD=90%) | | ±0.2 mm (±0.008") | - |
| Sizing Capabilities | | | |
| Minimum diameter | | 10 mm (0.39") | - |
| Minimum depth | parent material | 0.8 mm (0.03") | 1 mm (0.04") |
| | long seam | | 2 mm (0.08") |
| Minimum length | | - | 40 mm (1.57") |
| Depth sizing accuracy | | ±0.4 mm (±0.016", POD=90%) | ±0.15t (POD=80%) |
| Length sizing accuracy | | ±7 mm (±0.27", POD=90%) | ±20 mm (±0.78") |
| Width sizing accuracy (POD=90%) | | ±8 mm (±0.31") | - |
| *Abbreviations: POD = Probability of Detection; t = wall thickness | | | |

Figure 47: High resolution piezoelectric ultrasonic tool (ROSEN Group)

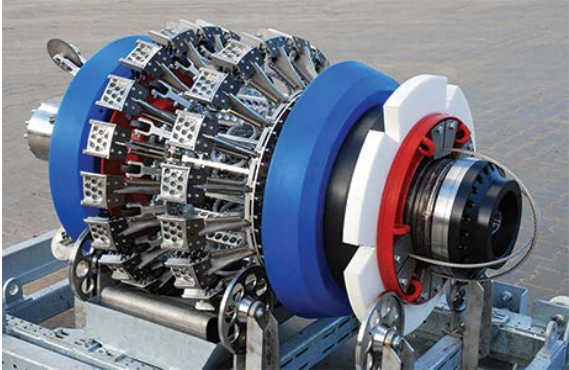


Figure 48: EMAT tool (Baker Hughes)



Leakage Detection Technologies

Gas Sensing Technologies

Introduction to Gas Sensing Technologies

Many different types of gas sensing technology are on the market, and this section only focuses on combustible gas sensing technologies. Table 27 shows the comparison of commonly used combustible gas sensing technologies. Most of these sensors could be associated with WSN technology (some may need energy harvesting due to large power consumption). The units of concentration often used in the datasheets of these sensors include parts-per notation (e.g., ppm, ppb, ppt) and lower explosive limit (LEL), which stands for the lowest concentration of a gas or vapor that could be burned in air. The performance of some gas sensors may be reduced by specific airborne material known as the poison of the sensor. There is no sensor that can sense all gases, and some sensors may have the same response to different gases. Therefore, different sensors are often associated together for a specific application.

Table 27: Comparison of Combustible Gases Sensing Technologies

| TECHNOLOGY | CATALYTIC BEAD | NDIR | TDLAS |
|-------------------|--|---|---|
| Suitable Gases | All combustible gases with molecule smaller than nonane (C ₉ H ₂₀). | Unavailable for diatomic molecules gases. | Unavailable for diatomic molecules gases. |
| Advantages | Inexpensive, reliable, and non-gas-specific. | Low-power, full range measurement. | Low-power, full range measurement, high sensitivity (ppbv). |
| Disadvantages | Need oxygen and maintenance. | Gas-specific, high cost. | Gas-specific, high cost, not be widely implemented yet. |
| Occasions | Multi-combustible gases sensing. | Environment without oxygen, gases with molecule larger than nonane (C ₉ H ₂₀). | Low concentration measuring. |
| Response Time | 35sec | 30sec | 1sec |
| Power consumption | 1.6W | 1.6W | 2W |

Catalytic Bead Sensor (Pellistor)

Catalytic bead sensors have been widely used for combustible gas sensing for more than half a century. It consists of two coiled fine platinum wires, each embedded in a bead of alumina and connected to a Wheatstone bridge circuit. One of them is treated with an oxidation promoted coating, while the other one is treated with oxidation inhibited coating as a reference. The combustible gases oxidized only at the oxidation promoted treated bead, resulting in a higher

temperature and electrical resistance. It leads to a change of the Wheatstone bridge's output due to the imbalance of the resistance on the bridge. At the same time, the reference bead compensates for the temperature and humidity effects. The output is linear and proportional to the combustible gases concentration (0-100% LEL) for most gases. Catalytic bead sensors are produced by numerous manufacturers due to their simple working principles. However, the performance and reliability vary widely among these manufacturers due to the difficulty of the chemical treatment design.

Catalytic bead sensors' sensitivity may be reduced (poisoned) by some airborne substances. Therefore, it is necessary to test the catalytic bead sensors regularly. The beads are protected by a flame arrestor which will block the gases with a larger molecule. The larger the molecule is, the slower it diffuses through the flame arrestor, resulting in a longer response time. Saturated hydrocarbons larger than nonane (C_9H_{20}) are unable to be measured. Therefore, a catalytic bead sensor should not be used to measure hydrocarbon gases larger than nonane in size.

Another disadvantage of catalytic bead sensors is that they are only reliable when the volumetric oxygen concentration in the environment is more than 12%, which is required for oxidation during the measuring. Therefore, catalytic bead sensors are usually coupled with an oxygen sensor to verify its reliability.

In general, catalytic bead sensors have the advantages of being low cost, reliable and non-gas-specific. It is also possible to be associated with WSN technology since it is a low-power device. For example, the catalytic bead sensor shown in Figure 49 has a typical power consumption of 525mW (175mA@3V). However, it has some disadvantages, including being unable to measure hydrocarbon gases larger than nonane in size, needs to be associated with an oxygen sensor, needs oxygen, requires to be tested regularly, and a limited lifetime (typically 5-years). It usually has a response time of a few seconds.

Figure 49: Figaro Catalytic Bead Sensor TGS6812-D00 (Figaro)



Nondispersive Infrared Sensor

Nondispersive infrared (NDIR) sensor is a spectroscopic sensor often used as a gas detector. It measures gas as a function of the absorbance of infrared light. It consists of an infrared (IR) source (lamp), sample or light tube, reference chamber or light tube, light filter, and infrared detector. The IR lights are directed through two chambers toward the detectors. The sample chamber allows environment gas to flow in and causes absorption of specific wavelengths

when IR light passes through it. The attenuation of these wavelengths is measured by the detector to determine the related gas concentration. Reference chamber encloses a known gas (typically nitrogen) is used as a reference.

NDIR sensors have several advantages. They do not need to be equipped with external flame arrestors that will slow or limit the entry of large hydrocarbon molecules into the sensor. They also do not need oxygen for measurements. They will not be poisoned easily compared to catalytic bead sensors, which allow them to have a low life-cycle cost and a precise and stable long-term operation (may up to 15 years). Furthermore, they are also low-power consumption and perform best in higher concentrations (2,000 – 10,000 ppm). Figure 50 shows an ethane NDIR sensor manufactured by SENSIT.

NDIR sensors are less commonly used due to their limitations. It cannot measure diatomic molecule gases that do not absorb infrared light, such as oxygen, nitrogen, and hydrogen. It is gas-specific and can only be used for gases that absorb IR light at the measured wavelengths. For example, NDIR sensors that measure the IR wavelength from 3.33 μm to 3.4 μm cannot measure acetylene (3.01 μm). It also has the disadvantages of warm-up time required for accurate measurement, which may be up to 5 minutes, and 3-4 times more expensive than catalytic bead sensors.

Figure 50: Infrared ethane detector (SENSIT)



Tunable Diode Laser Absorption Spectroscopy (TDLAS)

Tunable diode laser absorption spectroscopy (TDLAS) is one of the most common techniques to analyze the properties and constituents of gases. TDLAS measures the wavelength-dependent absorption of light through a gas medium, similar to NDIR but a tunable-wavelength diode laser as the light source instead. Therefore, the sensitivity of TDLAS is significantly enhanced by modulating the current of the laser. This leads to a modulation of the wavelength and of the light intensity. The absorption response is then recovered by demodulating the signal from the photodetector at the modulating frequency and its second-order harmonic. Figure 51 shows an open-path TDLAS system FPL manufactured by SENSIT with a detection range of 0-10,000ppm-m and a sensitivity of 2.5ppm-m.

TDLAS has many advantages, such as it can be used for measuring not only the concentration but also the temperature, pressure, and flow velocity. It is also the most sensitive gas sensing

technology (of the order of ppb). However, this technology has not been widely implemented yet, and the cost is significantly higher than other technologies introduced above.

IBM's T.J Watson Research Center is working in conjunction with Harvard University and Princeton University to produce a miniaturized, integrated, on-chip version that is less expensive and consumes less power. At a planned cost of about \$300 per sensor, IBM's sensors will be 10 to 100 times cheaper than TDLAS sensors on the market today.

Figure 51 Fixed-point Open-path Laser Methane Emissions Monitor FPL (SENSIT)



Flow Monitoring Technologies

Introduction to Flow Monitoring Technologies

Flow monitoring uses flowmeters to measure the flow rate (volumetric or mass) of fluids passing through a pipe. Numerous flow monitoring technologies are available, depending on the application, the specific fluid, and the construction. The flowmeters commonly used for natural gas flow monitoring can be divided into four types: (a) Mass flowmeters – Coriolis, Thermal mass, (b) Volumetric flowmeters – Turbine, Ultrasonic, Vortex, (c) Differential pressure meters, and (d) Positive displacement flowmeters. Table 28 shows the comparisons between the above flow monitoring technologies.

When selecting a flowmeter, the turndown ratio must be considered. The turndown ratio is calculated by dividing the maximum flow rate by the minimum, indicating the measuring

range. Some limitations may be applied to specific flow meters, such as gas types, required pressure and temperature compensation or correction, and the pipe size. Table 29 shows the common terms and their definition for selecting a flow meter.

Table 28: Comparison of Natural Gas Flow Monitoring Technologies

| TECHNOLOGY | ADVANTAGES | DISADVANTAGES | OCCASIONS |
|-----------------------|--|--|---|
| Coriolis | High accuracy and turndown ratio, independent of fluid properties and entrained gases | Expensive to purchase and install, pressure drop, not suitable for large pipe size | Small pipe sizes, changing conditions |
| Thermal mass | High accuracy and repeatability, easy to install | Very low response time, dry and clean fluids | Dry and clean fluids |
| Turbine | Very high versatility and accuracy, fast response time, high pressure and temperature capabilities | Moving parts can wear or clogged, not suitable for low flow rate | Not for low flow, viscous, dirty and corrosive fluids |
| Ultrasonic | Very high versatility and accuracy, no pressure drop, low maintenance, non-invasive | Expensive, not suitable for low flow rate | Not for low flow |
| Vortex | Low pressure drop, High versatility and pressure capability | Limited by viscosity and minimum flow rate, need temperature and pressure compensation, no entrained solid and gas | Clean gas, high pressure, low viscous fluids |
| Differential pressure | Flexible specification, experienced and reliable, generally low cost | Limited range ability, complex installation | Most occasions |
| Positive displacement | Very high versatility, accuracy and turndown ratio, reliable | Moving parts can wear or clogged, need temperature and pressure compensation, pressure drop | Most occasions (includes viscous, dirty and corrosive fluids) |

Table 29: Common Terms of Natural Gas Flowmeters

| TERMS | DEFINITION | UNITS |
|---------------------------------|--|------------------------|
| Accuracy | The uncertainty or error of the measurement, expressed as a percentage. | % (full scale, FS) |
| Standard feet per minute (SFPM) | The unit of flow rate. To convert from SFPM to standard cubic feet per minute (SCFM), multiply the standard velocity in SFPM by the cross sectional pipe area. | SFPM |
| Lower range limit (LRL) | The lower limit of the measurement range (not analog reading). | L/hr, kg/hr, m/s, SFPM |
| Upper range limit (URL) | The upper limit of the measurement range (not analog reading). | L/hr, kg/hr, m/s, SFPM |
| Turndown ratio | The range in which a flowmeter can accurately measure the fluid, calculated by LRL/URL. | - |
| Overpressure limit | The maximum operating pressure without damaging the meter. | kPa |
| Permanent pressure loss (PPL) | The approximate permanent pressure loss from the flowmeter. | kPa |

Mass Flowmeter

Mass flowmeters do not measure the volume per unit time passing through the device but the mass per unit time.

Coriolis flowmeter

Coriolis flowmeter offers accurate mass flow measurement through two designs: a single tube or two parallel tubes. It operates via an oscillation that is induced in the tube(s) at a reference frequency. Based on Newton's Second Law of Motion, the oscillation frequency will change with changes in mass flow rate.

Coriolis flowmeter has the advantages of high accuracy (typically $\pm 0.25\%$), high turndown capability (typically 60:1), and independent fluid properties, making it suitable for a wide and growing range of gas and liquid applications. The nominal minimum/maximum flow rate can down/up to 35/2400000 L/hr (for nickel alloy), and the maximum operating pressure may be as high as 400 barg. It may provide multiple measurements including mass, density and temperature. Figure 52 shows a Coriolis flowmeter manufactured by Micro Motion. Table 30 shows the typical specifications of Coriolis flowmeters.

Table 30: Typical Specifications of Coriolis Flowmeters

| Accuracy (% FS) | LRL (L/hr) | URL (L/hr) | Turndown | Overpressure (barg) | PPL (barg) |
|--------------------|---------------|---------------|----------|------------------------|---------------|
| ±0.25 | 35 | 2400000 | 60:1 | 400 | 1 |

Figure 52: Micro Motion ELITE CMF350P Coriolis flowmeter (Micro Motion)



Thermal Mass flowmeter

Thermal mass flowmeter usually contains a heating element and temperature sensors. It determines the flow rate by measuring the temperature difference between static and flowing heat transfer to a fluid and the fluid's specific heat and density. It does not need pressure and temperature compensation if the fluid's density and specific heat characteristics are constants.

Thermal mass flowmeter is popular because it features no moving parts, nearly unobstructed straight through flow path, high turndown capability (typically 100:1) and require no temperature or pressure compensation and retain accuracy (typically ±0.5%) over a wide range of flow rates (typically minimum/maximum can down/up to 10/50000 SFPM). It typically has an operating pressure of 100 barg. However, the accuracy highly depends on the actual composition of the fluid since the calibration is for the specific fluid's density and specific heat characteristics. Figure 53 shows a thermal mass flowmeter manufactured by Magnetrol. Table 31 shows the typical specifications of thermal mass flowmeters.

Table 31: Typical specifications of thermal mass flowmeters

| Accuracy | LRL | URL | Turndown | Overpressure | PPL |
|-----------|----------|-------------|----------|--------------|-----|
| ±0.5%, FS | 10, SFPM | 50000, SFPM | 100:1 | 100 barg | - |

Figure 53: Magnetrol ThermoTel TA2 Thermal Mass Flowmeter (Magnetrol)



Volumetric Flowmeter

Volumetric flowmeters directly measure the rate of the medium passing through the meter.

Turbine flowmeter

Turbine flowmeter uses the mechanical energy of the fluid to rotate a bladed rotor positioned along the centerline of the flow stream. Shaft rotation can be sensed mechanically or by detecting the movement of the blades magnetically. When the fluid moves faster, the rotor spins proportionally faster, and more pulses are generated to the detecting sensor, which is usually located external to the flowing stream. The transmitter processes the pulse signal to determine the fluid flow in both the forward and reverse flow directions.

Turbine flowmeter is very good at clean, low viscosity, mid to high velocity, and steady rate fluids. Some designs can handle slightly viscosity fluids. It has high accuracy (typically $\pm 1\%$), high turndown (20:1), high operating pressure (typically from 0 to 100 barg), and the nominal minimum/maximum flow rate can typically down/up to 5000/25000000 L/hr with a moderate cost. However, turbine flowmeter is not the best choice for steam and low-rate flow monitoring. Having moving parts is also a drawback, and they do cause a relatively high pressure drop. Figure 54 shows a turbine gas flowmeter manufactured by Honeywell. Table 32 shows the typical specifications of turbine flowmeters.

Table 32: Typical Specifications of Turbine Gas Flowmeters

| Accuracy | LRL | URL | Turndown | Overpressure | PPL |
|----------------|------------|----------------|----------|--------------|-----|
| $\pm 1\%$, FS | 5000, L/hr | 25000000, L/hr | 20:1 | 100 barg | - |

Figure 54: Honeywell Elster TRZ2 Turbine Gas Flowmeter (Honeywell)



Ultrasonic flowmeter

Ultrasonic flowmeter uses ultrasonic waves to determine the fluid flow rate in the pipe. The differential frequency between the ultrasonic wave transmitted into the pipe and its reflections from the fluid is proportional to the flowrate of the fluid due to the Doppler effect. When the flow rate increases, the frequency shift increases linearly. The transmitter processes the received signal to determine the flow rate of the fluid.

Ultrasonic flowmeter is very accurate (can be down to $\pm 0.01\%$) and commonly used for custody transfer of natural gas and petroleum liquids. It also has the pluses of high turndown (can up to 130), high maximum measuring range (can up to 34000000L/hr), high operating pressure range (0-300 bar), extreme operating temperature, repeatable (consistent), and non-invasive installation. It does not obstruct flow (no pressure drop and can be applied to any type of fluids), is low maintenance and is highly reliable. However, it has the minuses of high cost and sensitivity to stray process vibrations. The accuracy may reduce due to the change of the pipe diameter.

Figure 55 shows an ultrasonic gas flowmeter manufactured by Honeywell (RMG). Table 33 shows the typical specifications of ultrasonic flowmeters.

Table 33: Typical Specifications of Ultrasonic Gas Flowmeters

| Accuracy | LRL | URL | Turndown | Overpressure | PPL |
|-----------------|------------|--------------|-----------------|---------------------|------------|
| ±0.01%, FS | - | 34000000L/hr | 130:1 | 300 barg | - |

Figure 55: Honeywell (RMG) USM GT400 ultrasonic gas flowmeter (Honeywell)



Vortex flowmeter

Vortex flowmeter determines the flow rate using a sensor that detects the oscillations (or pressure pulses) from vortices induced by the fluid passing by a bluff body obstruction across the flow stream based upon the Coanda effect and vortex precession. The frequency of vortex precession which results in pressure pulses and oscillations is directly proportional to the flow rate of the fluid.

Vortex flowmeter has the advantages of relatively high accuracy (typically $\pm 1\%$), high turndown of (can up to 50), not being sensitive to variations in process conditions. It has no moving parts. Their maximum measuring range can be up to 90 m/s (depends on fluid density), and the maximum operating pressure can be up to 250 barg. Figure 56 shows a vortex gas flowmeter manufactured by Rosemount. Table 34 shows the typical specifications of vortex flowmeters.

Table 34: Typical Specifications of Vortex Flowmeters

| Accuracy | LRL | URL | Turndown | Overpressure | PPL |
|----------------|-----|--------|----------|--------------|-----|
| $\pm 1\%$, FS | - | 90 m/s | 50:1 | 250 barg | - |

Figure 56: Rosemount 8800DF040 Flanged Vortex Flowmeter (Rosemount)



Differential Pressure Flowmeter

Differential pressure flowmeter uses Bernoulli's equation and the changes in pressure to determine flow velocity. They introduce a constriction (orifice or laminar flow element) that creates a pressure drop between upstream and downstream of the flowmeters. When the flow rate increases, more pressure drop between upstream and downstream is created, which is proportional to the square of the flow rate and can be measured by two pressure gauges attached on each side.

Differential pressure flowmeters have the advantages of low cost, easy to be optimized for different fluids and applications, have no moving parts, and ultrafast response time. However, they have the drawback of regular accuracy (typically $\pm 2\%$), relative poor measuring range due to the non-linear processing (laminar flow elements excepted) and can deteriorate with wear and clogging. This section will not introduce the typical specification of the differential pressure flowmeters since their specifications highly depend on the selected pressure sensors and may vary dramatically according to the different applications.

Positive Displacement Flowmeter

Positive displacement (PD) flowmeter measures the volumetric flow rate of a moving fluid or gas by dividing the media into fixed, metered volumes (finite increments or volumes of the fluid). It requires the divided fluid to displace components (e.g., screw) mechanically and determines volumetric flow at the operating temperature and pressure by measuring the speed of the displaced components. The mass flow rate can be accurately determined with appropriate pressure and temperature compensation.

Positive displacement flowmeters have a long life expectancy (typically >30 yr), high accuracy (typically $\pm 0.3\%$), high turndown (typically 100:1), and relatively low cost. The nominal minimum/maximum flowrate can typically down/up to 0.03/14000 L/hr, and the maximum operating pressure may be as high as 400 barg. Some types of PD flowmeters can be used in very viscous, dirty, and corrosive fluids and essentially require no straight runs of pipe for fluid flow stream conditioning though pressure drop can be an issue. However, they require periodic maintenance due to the moving components. Figure 57 shows a positive displacement flowmeter manufactured by Max Machinery with $\pm 0.3\%$ of rate accuracy and 400 barg of maximum working pressure. Table 35 shows the typical specifications of positive displacement flowmeters.

Figure 57: Max Machinery G004 gear flowmeter (Max Machinery)



Table 35: Typical Specifications of Positive Displacement Flowmeters

| Accuracy | LRL | URL | Turndown | Overpressure | PPL |
|-----------|-----------|------------|----------|--------------|-----|
| ±0.3%, FS | 0.03 L/hr | 14000 L/hr | 100:1 | 400 barg | - |

CHAPTER 4: Conclusions

Technologies that apply to natural gas infrastructure have been detailed in this report in the categories of remote sensing, continuous monitoring, inspection technologies and leakage detection. The rapidly expanding infrastructure monitoring market has outpaced the ability of natural gas providers to keep up with the knowledge and skillset necessary to implement the latest techniques in a timely fashion. In addition, new risk models have been developed that predict damage to infrastructure caused by seismic hazards. The Open Seismic Risk Assessment (*OpenSRA*) project is compiling these risk models into a convenient application that infrastructure owners can use to assess their assets for seismic risk. Sensed information can be leveraged to inform risk models from a perspective of reducing uncertainty on the input parameters and verifying the accuracy of predicted behavior.

This report provides a thorough review of monitoring technologies that can be applied to make California's natural gas infrastructure safer and reduce the amount of methane released into the atmosphere. The technologies are presented in the context of *OpenSRA* input, intermediate and output variables, as illustrated in Tables 1-3 in Chapter 2. The descriptions of these technologies include the fundamental measurement principles, capabilities, limitations, and costs. The feasibility of these technologies in providing inputs to the *OpenSRA* tools or checking the intermediate or output parameters of the *OpenSRA* analysis is discussed.

For the monitoring data to be useful as inputs to risk assessment, the precision error of sensing systems needs to be evaluated and included in the uncertainty quantification of the estimated risk. This report describes the results of lab and field experiments that quantified the precision errors of selected sensing systems in its appendix.

GLOSSARY OR LIST OF ACRONYMS

| Term | Definition |
|-------|---|
| ADC | Analog-To-Digital Converter |
| AES | Advanced Encryption Standard |
| ALS | Airborne Laser Scanning |
| BODTA | Brillouin Optical Time Domain Analysis |
| BODTR | Brillouin Optical Time Domain Reflectometry |
| CEC | California Energy Commission |
| COTDR | Coherent Optical Time Domain Reflectometry |
| DAS | Distributed Acoustic Sensing. |
| DDM | Digital Deformation Model |
| DEM | Digital Elevation Models |
| DFOS | Distributed Fiber Optic Sensors |
| DSM | Digital Surface Model |
| DSS | Distributed Strain Sensing. |
| DSTS | Distributed Strain And Temperature Sensing. |
| DTM | Digital Terrain Model |
| DTS | Distributed Temperature Sensing. |
| EMAT | Electromagnetic Acoustic Transducer |
| FDR | Frequency Domain Reflectometry |
| FoV | Field of View |
| FS | Full Scale |
| GPS | Global Positioning System |
| GSD | Ground Sampling Distance |
| HPC | High-Performance Computing |
| IEPE | Internal Electronic Piezoelectric |
| ILI | In-Line Inspection |
| InSAR | Interferometric Synthetic Aperture Radar |
| IoT | Internet of Things |

| Term | Definition |
|----------------|--|
| IR | Infrared |
| IR-LED | Infrared Light-Emitting Diode |
| ISM | Industrial, Scientific And Medical |
| LEL | Lower Explosive Limit |
| LiDAR | Light Detection And Ranging |
| LOC | Loss of Containment |
| LoRaWAN | Long Range Wide Area Network |
| LPWAN | Low-Power Wide-Area Networks |
| LRL | Lower Range Limit |
| LTE | Long-Term Evolution |
| LVDT | Linear Variable Differential Transformer |
| MCU | Microcontroller Unit |
| MDS | Multiple Dataset |
| MEMS | Microelectromechanical Systems |
| MFL | Magnetic Flux Leakage |
| NB-IoT | Narrowband Internet of Things |
| NDIR | Nondispersive Infrared |
| NDT | Non-Destructive Testing |
| NGMs | Next Generation Meters |
| OCDR | Optical Correlation Domain Reflectometry. |
| OFDR | Optical Frequency Domain Reflectometry. |
| <i>OpenSRA</i> | Open Seismic Risk Assessment |
| OTDA | Optical Time Domain Analysis. |
| OTDR | Optical Time Domain Reflectometry. |
| PCB | Printed Circuit Boards |
| PD | Positive Displacement |
| PEER | Pacific Earthquake Engineering Research Center |
| PG&E | Pacific Gas And Electric |

| Term | Definition |
|----------|---|
| POD | Probability of Detection |
| PPL | Permanent Pressure Loss |
| RBS | Rayleigh Backscatter Spectrum |
| ROTDR | Raman-Based Optical Time Domain Reflectometry |
| RSSI | Received Signal Strength Indicator |
| RTK | Real-Time Kinematic |
| RTTM | Real-Time Transient Model |
| SAR | Synthetic Aperture Radar |
| SBS | Stimulated Brillouin Scattering |
| SCFM | Standard Cubic Feet Per Minute |
| SfM | Structure From Motion |
| SFPM | Standard Feet Per Minute |
| SIFT | Scale-Invariant Feature Transform |
| SMDs | Surface-Mount Devices |
| SMFL | Spiral Magnetic Flux Leakage |
| SoCalGas | Southern California Gas Company |
| SRTM | Shuttle Radar Topography Mission |
| SURF | Speeded-Up Robust Features |
| TAC | Technical Advisory Committee |
| TDLAS | Tunable Diode Laser Absorption Spectroscopy |
| TDOA | Time Difference of Arrival |
| TDR | Time Domain Reflectometry |
| TLS | Terrestrial Laser Scanning |
| ToF | Time of Flight |
| UAV | Unmanned Aerial Vehicle |
| UCSD | University of California San Diego |
| UNR | University of Nevada, Reno |
| URL | Upper Range Limit |

| Term | Definition |
|--------|---|
| UT | Ultrasonic Test |
| UTM | Ultrasonic Thickness Measurement |
| VCSEL | Vertical-Cavity Surface-Emitting Laser |
| WSN | Wireless Sensor Network |
| φ-OTDR | Phase Optical Time-Domain Reflectometry |
| (M)TLS | Mobile Terrestrial Laser Scanning |
| (S)TLS | Static Terrestrial Laser Scanning |

REFERENCES

- Abdelhafidh, M., Fourati, M., Fourati, L. C., & Laabidi, A. (2018). An investigation on wireless sensor networks pipeline monitoring system. *International Journal of Wireless and Mobile Computing*, 14(1), 25-46.
- Agrawal, G.P. (2007). *Nonlinear fibre optics* (5th ed.). Oxford: Academic Press.
- Ahmed, R., Siqueira, P., Hensley, S., Chapman, B., & Bergen, K. (2011). A survey of temporal decorrelation from spaceborne L-Band repeat-pass InSAR. *Remote Sensing of Environment*, 115(11), 2887-2896.
- Akyildiz, I. F., Melodia, T., & Chowdury, K. R. (2007). Wireless multimedia sensor networks: A survey. *IEEE Wireless Communications*, 14(6), 32-39.
- Ansari, F. (2007). Practical implementation of optical fiber sensors in civil structural health monitoring. *Journal of Intelligent Material Systems and Structures*, 18(8), 879–889.
- Anumalla, S., Ramamurthy, B., Gosselin, D. C., & Burbach, M. (2005, May). Ground water monitoring using smart sensors. In 2005 IEEE International Conference on Electro Information Technology (pp. 6-pp). IEEE.
- Aoudia, F. A., Gautier, M., Magno, M., Le Gentil, M., Berder, O., & Benini, L. (2018). Long-short range communication network leveraging LoRa™ and wake-up receiver. *Microprocessors and Microsystems*, 56, 184-192.
- Bao, X., & Chen, L. (2011). Recent progress in Brillouin scattering based fibre sensors. *Sensors*, 11, 4152–4187.
- Bao, X., & Chen, L. (2012). Recent progress in distributed fibre optic sensors. *Sensors*, 12, 8601–8639.
- Barbian, A., Beller, M., Hartmann, S., & Schneider, U. (2011, April). High resolution ultrasonic in-line inspection: Added value and special applications. In 6th Pipeline Technology Conference (Vol. 4).
- BenSaleh, M. S., Qasim, S. M., Obeid, A. M., & Garcia-Ortiz, A. (2013, May). A review on wireless sensor network for water pipeline monitoring applications. In 2013 International Conference on Collaboration Technologies and Systems (CTS) (pp. 128-131). IEEE.
- Boubiche, D. E., Athmani, S., Boubiche, S., & Toral-Cruz, H. (2021). Cybersecurity issues in wireless sensor networks: current challenges and solutions. *Wireless Personal Communications*, 117(1), 177-213.
- Boyd, R. (2008). *Nonlinear optics* (3rd ed.). New York, NY: Academic Press.

- Chhaya, L., Sharma, P., Bhagwatikar, G., & Kumar, A. (2017). Wireless sensor network based smart grid communications: Cyber attacks, intrusion detection system and topology control. *Electronics*, 6(1), 5.
- Cornell, C.A. (1968), Eng Seis Risk Analysis, *Bull. Seismo. Soc. Am.*, V58(5), 1583-1606, doi: 10.1785/BSSA0580051583.
- Culshaw, B., Michie, C., Gardiner, P., & McGown, A. (1996). Smart structures and applications in civil engineering. *Proceedings of the IEEE*, 84(1), 78-86.
- David, B. C., Alan, E. S. (2001). "State of the Art for Pipe and Leak Detection." US Department of Energy Report.
- de Carvalho Silva, J., Rodrigues, J. J., Alberti, A. M., Solic, P., & Aquino, A. L. (2017, July). LoRaWAN—A low power WAN protocol for Internet of Things: A review and opportunities. In 2017 2nd International Multidisciplinary Conference on Computer and Energy Science (SpliTech) (pp. 1-6). IEEE.
- Deng, L., & Cai, C.S. (2007). Applications of fiber optic sensors in civil engineering. *Structural Engineering and Mechanics*, 25(5), 577–596.
- Fowler, R., (2001). Topographic Lidar, Digital Elevation Model Technologies and Applications: The DEM Users Manual, (D. Maune, editor), American Society for Photogrammetry and Remote Sensing, Bethesda, Maryland, pp. 207–236.
- Gaddam, S. C., & Rai, M. K. (2018, July). A comparative study on various LPWAN and cellular communication technologies for IoT based smart applications. In 2018 International Conference on Emerging Trends and Innovations In Engineering And Technological Research (ICETIETR) (pp. 1-8). IEEE.
- Greenwood, W. W., Lynch, J. P., & Zekkos, D. (2019). Applications of UAVs in civil infrastructure. *Journal of Infrastructure Systems*, 25(2), 04019002.
- Gungor, V. C., & Lambert, F. C. (2006). A survey on communication networks for electric system automation. *Computer Networks*, 50(7), 877-897.
- Habel, W.R., & Krebber, K. (2011). Fiber-optic sensor applications in civil and geotechnical engineering. *Photonic Sensors*, 1(3), 268–280.
- Ho, M., El-Borgi, S., Patil, D., & Song, G. (2020). Inspection and monitoring systems subsea pipelines: A review paper. *Structural Health Monitoring*, 19(2), 606-645.
- Hough, J. E. (1988). Leak testing of pipelines uses pressure and acoustic velocity. *Oil Gas J.:(United States)*, 86(47).
- Kayen, R. (2021, May 20–21). SHORT COURSE on New Technologies for Geotechnical Infrastructure Sensing and Monitoring [Terrestrial Laser Scanning]. 2021, Berkeley, CA, United States.

- Kayen, R., Stewart, J. P., & Collins, B. (2010, May). Recent advances in terrestrial LIDAR applications in geotechnical earthquake engineering. In 5th Int. Conf. on Recent Advances in Geotechnical Earthquake Engrg and Soil Dynamics.
- Klein W. R. (1993). Acoustic leak detection, American Society of Mechanical Engineers, Petroleum Division, 1993, Vol.55, p57-61
- Kurmer, J. P., Kingsley, S. A., Laudo, J. S., & Krak, S. J. (1993, March). Applicability of a novel distributed fiber optic acoustic sensor for leak detection. In Distributed and Multiplexed Fiber Optic Sensors II (Vol. 1797, pp. 63-71). International Society for Optics and Photonics.
- Mekki, K., Bajic, E., Chaxel, F., & Meyer, F. (2019). A comparative study of LPWAN technologies for large-scale IoT deployment. *ICT express*, 5(1), 1-7.
- Oh, S., Shin, J. (2017). "Efficient Small Data Transmission Scheme in 3GPP NB-IoT System", *IEEE Communications Letters*, Vol. 21, 2017, pp. 660- 663
- Pipeline Operators (2021). Specifications and requirements for in-line inspection of pipelines: Standard Practice POF 100. <https://ucarecdn.com/276341a3-f5e6-49cf-9897-de6ab41bdd5a/POF%20100%20Specifications%20and%20requirements%20for%20ILI%20-%20Nov%202021.pdf>
- Radmand, P., Talevski, A., Petersen, S., & Carlsen, S. (2010, April). Taxonomy of wireless sensor network cyber security attacks in the oil and gas industries. In 2010 24th IEEE International Conference on Advanced Information Networking and Applications (pp. 949-957). IEEE.
- Silva-López, M., Fender, A., MacPherson, W. N., Barton, J. S., Jones, J. D., Zhao, D., ... & Bennion, I. (2005). Strain and temperature sensitivity of a single-mode polymer optical fiber. *Optics letters*, 30(23), 3129-3131.
- Soga, K., & Luo, L. (2018). Distributed fiber optics sensors for civil engineering infrastructure sensing. *Journal of Structural Integrity and Maintenance*, 3(1), 1-21.
- Sperl, J. L. (1991). System pinpoints leaks on Point Arguello offshore line. *Oil and Gas Journal*;(United States), 89(36).
- Sun, Z., Wang, P., Vuran, M. C., Al-Rodhaan, M. A., Al-Dhelaan, A. M., & Akyildiz, I. F. (2011). MISE-PIPE: Magnetic induction-based wireless sensor networks for underground pipeline monitoring. *Ad Hoc Networks*, 9(3), 218-227.
- Turner, N. C. (1991, September). Hardware and software techniques for pipeline integrity and leak detection monitoring. In SPE Offshore Europe. OnePetro.
- Vanaei, H. R., Eslami, A., & Egbewande, A. (2017). A review on pipeline corrosion, in-line inspection (ILI), and corrosion growth rate models. *International Journal of Pressure Vessels and Piping*, 149, 43-54.

- Weil, G. J. (1993, May). Non contact, remote sensing of buried water pipeline leaks using infrared thermography. In *Water Management in the'90s: a Time for Innovation* (pp. 404-407). ASCE.
- Zekkos, D. (2021, May 20–21). SHORT COURSE on New Technologies for Geotechnical Infrastructure Sensing and Monitoring [Optical Data Collection & Structure from Motion]. 2021, Berkeley, CA, United States.
- Zekkos, D., Greenwood, W., Lynch, J., Manousakis, J., Athanasopoulos-Zekkos, A., Clark, M., & Saroglou, C. (2018). Lessons learned from the application of UAV-enabled structure-from-motion photogrammetry in geotechnical engineering. *Int. J. Geoenviron. Eng.*, 4(4), 254-274.
- Zhang, J. (1997). Designing a cost-effective and reliable pipeline leak-detection system. *Pipes and Pipelines International*, 42(1), 20-26.

APPENDIX A:

Technology demonstrations

Sensing of High-density Polyethylene Pipeline Deformation using Distributed Strain Sensing

Introduction

This section reports the results of a set of laboratory tests when distributed strain sensing (DSS) is used to monitor the deformation of HDPE pipelines subject to bending. The type of DSS used was Brillouin optical time-domain reflectometry (BOTDR). The main purpose of this work was to develop a practical method to attach sensing fiber reliably and reasonably to HDPE pipes in a construction setting for monitoring over the life of the asset. Several different attachment methods were tested before selecting the best one. A final test using the selected attachment method is presented with its associated data analysis and potential for monitoring HDPE pipes.

Objective

The objective of this set of tests was to develop an effective and practical deployment method for DSS on HDPE pipelines, including cable design, attachment materials, and processes. This development aims to be a suitable technique for monitoring pipelines of particular risk because of their proximity to geohazards or their elevated risk as determined by *OpenSRA*. Continuous or intermittent monitoring of these pipes using DSS would provide information to the owner/operators as to the actual performance of the pipelines and make preventative maintenance based on actual deformation data possible.

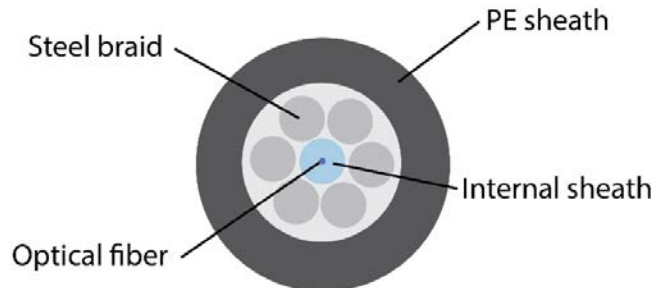
Technology

Distributed strain sensing is a distributed fiber optic sensing technology that measures the strain of an optical fiber in a distributed fashion over the fiber's length. The technique has a readout interval and spatial resolution. The readout interval is the spatial distance between where strain values are reported along a sensing fiber. The spatial resolution is the length of fiber that influences a strain measurement. So, readout intervals can be, and often are, smaller than the spatial resolution of a sensing system. For this set of tests, a technique called Brillouin optical time-domain reflectometry (BOTDR) was used. BOTDR examines the light frequency of a phenomenon called Brillouin backscatter. Brillouin backscatter occurs at different frequencies than the incident (laser) light. The frequency shift is proportional to strain and temperature change on the sensing fiber.

Since strain is sensed using an optical fiber, the fiber itself must be coupled to the pipeline. This is achieved using a tightly buffered fiber optic cable intended explicitly for use in strain sensing. The cable tightly bonds the fiber to the reinforcing elements within the cable and then to the cable's coating. From extensive experience using DSS to monitor infrastructure such as pile foundations, tunnels, roadways, wind turbine towers and retaining walls, the

researchers selected an internally steel armored sensing cable from NanZee Sensing called NZS-DSS-C02. The selected cable's cross-section is shown in Figure A-1. After cable selection, the next step was to attach the cable's coating adequately to the pipeline so that strain is transferred.

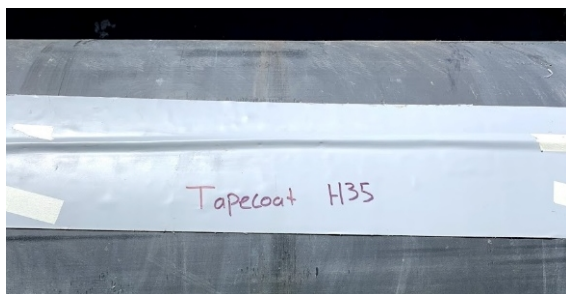
Figure A-1: Cross-section of NZS-DSS-C02 Sensing Cable (Hubbard et al., 2021)



Testing of attachment materials and preliminary bending test

The first test that was conducted was a simple comparison of attachment materials for effectiveness and ease of use. Four materials were selected for trial, including two pipe-wrapping materials and two epoxies. Due to commercial fairness to the materials not selected, only the selected materials are shown here. Figure A-2 shows the evaluation of Tapecoat H35 and 3M DP8010 at the time of application.

Figure A-2: Application of Tapecoat H35 and 3M DP8010 to an HDPE Pipeline for Initial Evaluation



The Tapecoat and DP8010 epoxy both performed well during application. They were simple to apply and provided an initial hold of the cable keeping it in place quickly. This initial hold was instant for the Tapecoat H35 and after about 10 minutes for the DP8010. The pipes and attachment were examined after one week of being kept in an outdoor storage yard. After one week the both the Tapecoat H35 and DP8010 provided a strong bond between the sensing cable and the pipe based on manual examination.

The next step was to attach a DSS sensing cable to a length of HDPE pipe and conduct a bending test. It was elected to only use Tapecoat H35 for this initial test because of its ease of use and performance during the first assessment. The bending test was conducted using forklift and fabric straps to vertically lift the 40-foot-long, 20-inch-diameter HDPE pipe.

Figure A-3 shows a photograph of the NZS-DSS-C02 cable attached to a test pipe before and during the bending test.

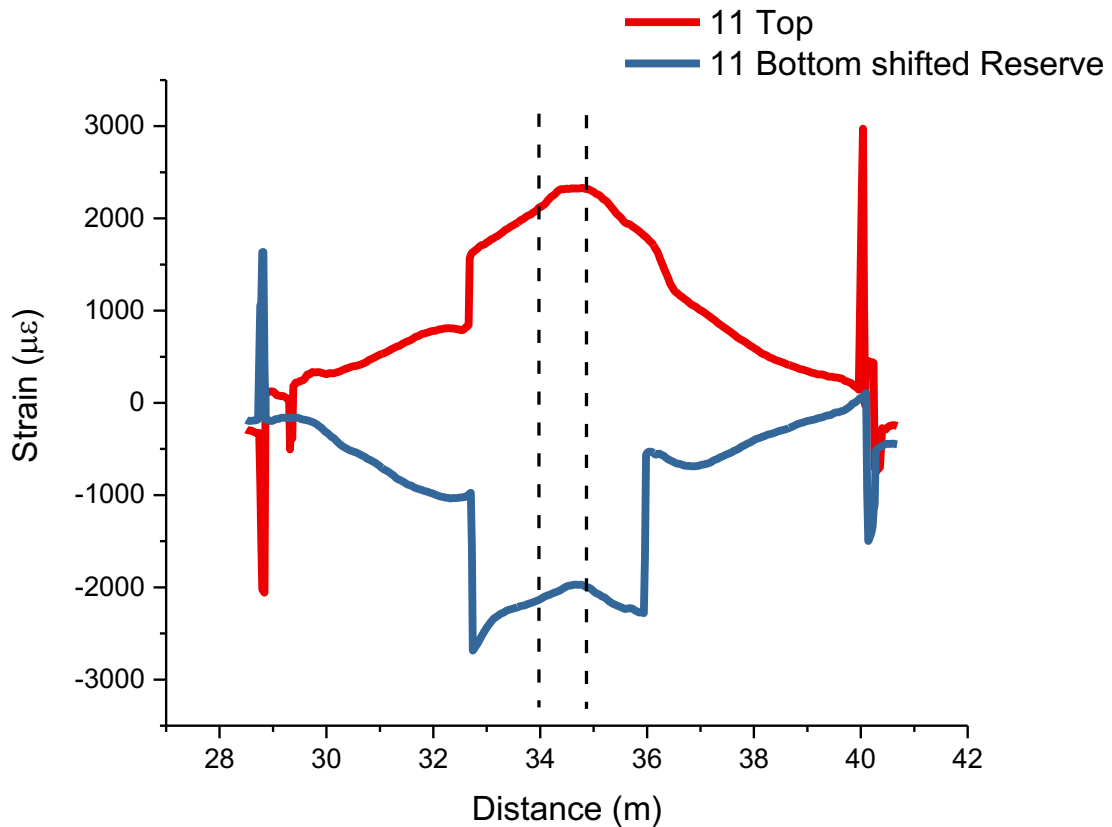
Figure A-3: Sensing Cable Attached to an HDPE Pipe



(A) Before and (B) During the bending test

This initial test revealed that the cable experienced slippage between the Tapecoat and pipe surface. The strain results are shown in Figure A-4. Both the cable running along the top and the bottom of the pipe experienced an abrupt jump in strain.

Figure A-4: Strain Measurements Made During the First Bending Test



It was possible that the lifting straps played a role in the slippage by placing additional friction on the sensing cables. However, this was refuted likely not the case because the lifting straps did not come in contact with the sensing cables at the top of the pipe, as shown in

Figure A-3(B). It was determined that additional coupling was needed other than the Tapecoat H35 alone.

Finalized Attachment Method and Second Bending Test

It was next attempted to combine the Tapecoat H35 and the DP8010 epoxy into one attachment method. The scheme designed was to first apply the Tapecoat H35 to hold the sensing cable in place on the pipe and then to inject the DP8010 underneath the Tapecoat H35 at intervals of 5 ft to improve the coupling. A test was conducted at the UC Berkeley's Center for Smart Infrastructure (CSI) to evaluate this testing method and determine the optimal radial configuration of sensing cables for sensing bending deformation.

Figure A-5 shows the test configuration and attachment method tested.

Figure A-5: Test Configuration and Attachment Method Tested



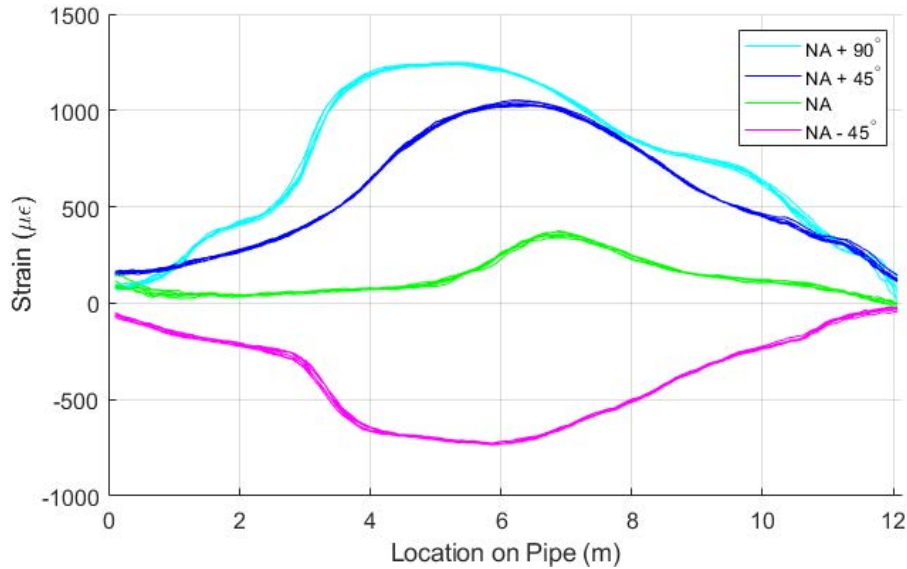
(A) The instrumented HDPE prior to the vertical bending test, (B) The tools used for DP8010 epoxy injection, (C) Injection sited for DP8010 epoxy and (D) the bending test in progress (Hubbard et al., 2021)

During this bending test, cables were placed at radial locations of 0° , 45° , 90° , and 135° from the crown of the pipe. The pipe was lifted vertically using a forklift, as shown in

Figure A-5(D). The BOTDR system was then used to make measurements along the sensing cables at a readout of 2cm and a spatial resolution of 1m. The raw strain results are shown in

Figure A-6. The neutral axis (NA) of bending is considered the 90° cable position.

Figure A-6: Raw Strain Measurements During the Second Bending Test. The cable locations are denoted relative the NA position (Hubbard et al., 2021).



The raw strain data was then further processed by separating the axial and bending strain according to the expressions:

Equation A-1

$$\varepsilon_a(x) = \frac{1}{3} (\varepsilon_{NA}(x) + \varepsilon_{NA+45^\circ}(x) + \varepsilon_{NA-45^\circ}(x))$$

Equation A-2

$$\varepsilon_{b_{NA+45^\circ}}(x) = \varepsilon_{NA+45^\circ}(x) - \varepsilon_a(x)$$

Equation A-3

$$\varepsilon_{b_{NA-45^\circ}}(x) = \varepsilon_{NA-45^\circ}(x) - \varepsilon_a(x)$$

Equation A-4

$$\varepsilon_{b,max}(x) = \frac{\sqrt{2}}{2} (|\varepsilon_{b_{NA+45^\circ}}(x)| + |\varepsilon_{b_{NA-45^\circ}}(x)|)$$

Where:

x is the location along the pipe

ε_a is the axial strain

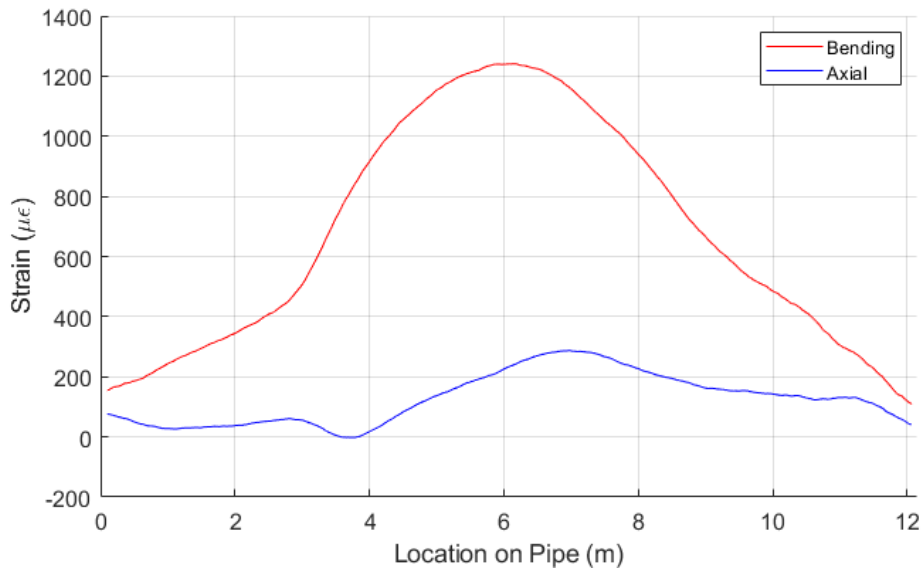
$\varepsilon_{b_{NA+45^\circ}}$ is the bending strain at the location NA + 45°

$\varepsilon_{b_{NA-45^\circ}}$ is the bending strain at the location NA – 45°

$\varepsilon_{b,max}$ is the maximum bending strain in the pipe

As shown by Equation A-1 to Equation A-4, the bending and axial strain in the pipe can be determined by only the NA, NA – 45° and NA + 45° cable positions. This is convenient because in a practical installation only the opt half of the pipe needs to be instrumented if horizontal bending is the primary deformation mechanism of interest. The calculated axial and bending strain profiles are shown in Figure A-7.

Figure A-7: Bending and axial strain in the pipe during bending as determined by the NA, NA – 45° and NA + 45° cable positions (Hubbard et al., 2021).



Finally, the deformation of the pipe can be determined by integrating the strain measurements away from the fixed boundary condition at the center of the pipe according to:

Equation A-5

$$\kappa(x) = \frac{\varepsilon_{b-max}(x)}{c}$$

Equation A-6

$$\theta(x) = \int_{\frac{L}{2}}^L \kappa(x) dx + \int_{\frac{L}{2}}^L \kappa(-x) dx$$

Equation A-7

$$v_b(x) = \int_{\frac{L}{2}}^L \theta(x) dx + \int_{\frac{L}{2}}^L \theta(-x) dx$$

The deflection due to axial strain is then:

Equation A-8

$$v_a(x) = \left[\int_{\frac{L}{2}}^L \varepsilon_a(x) dx + \int_{\frac{L}{2}}^L \varepsilon_a(-x) dx \right] \theta(x)$$

The total deflection is the sum of the contribution of bending and axial strain.

Equation A-9

$$v_t(x) = v_a(x) + v_b(x)$$

Where:

κ is the curvature of the pipe

θ is the rotation of the pipe

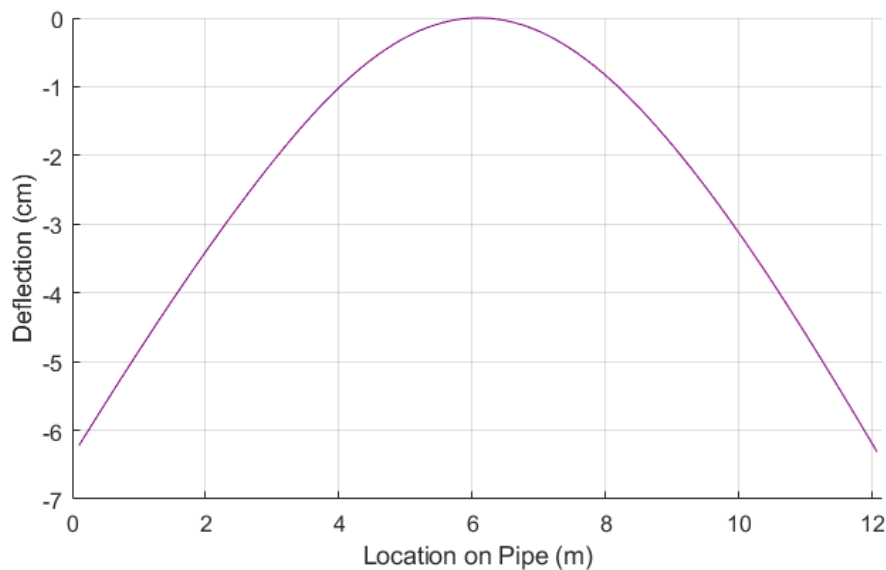
L is the total length of the pipe

v_b is the deflection due to bending

v_a is the deflection due to axial strain

Figure A-8 shows the calculated deflection from the strain measurements.

Figure A-8: Deflection of the pipe calculated from the strain measurements made by the NA, NA – 45° and NA + 45° cable positions (Hubbard et al., 2021).



The deflection at the end of the pipes was compared with physical measurements made during the bending tests using a tape measure. It was manually measured that the deflection was 6.5 and 6.8 cm at the $x = 0$ and $x = 12$ m locations, and the calculated values using the strain measurements are 6.1 and 6.3 cm, respectively.

Implication

It has been shown that DSS can be adequately attached to HDPE pipes to measure strain over their length. The measurements can then be used to determine a deformed shape assuming a consistent cross-section and elastic behavior. Though these assumptions may not be adequate for severe deformation situations, it provides a continuous monitoring tool that would give owner/operators a method to track cumulative pipe deformation and make decisions based

upon estimated pipe deformation and risk as calculated using *OpenSRA*. The technology has been demonstrated successfully and is ready to be deployed in the field.

High Pressure Test of Corroded Gas Well Tubing

Introduction

Corrosion in oil and gas well systems can bring economic losses and safety problems. Both internal corrosion and external corrosion are a huge threat to the well integrity. The occurrence of corrosion is very common on the inner tubing and outer casing. However, it's often difficult to identify and locate the corrosion areas until the corrosion leads to disastrous consequences. Therefore, how to detect the corrosion area becomes a challenging problem. The development of distributed fiber optic sensing (DFOS) provides new possibilities for detecting and locating the corrosion. Monitoring the strain of the well may help to determine whether there is corrosion happening at a certain location.

To study the feasibility of that, an experiment based on DFOS was designed and carried out at PEER Lab at Richmond Field Station. Fiber optic cables for strain and temperature were attached to a gas well tubing for monitoring. The tubing was then pressurized to normal working pressure gradually and its strains at different locations were measured in real time. The measured data was evaluated to find if there's an obvious strain difference to help to determine the corrosion area.

Technology

DFOS is gradually applied to the monitoring of civil structures and infrastructure. It makes it possible to measure different physical quantities dynamically and continuously. For this test, distributed strain sensing (DSS), and distributed temperature sensing (DTS) were used. Based on the Rayleigh backscatter, they can deliver a virtually continuous line of strain and temperature measurements with sub-millimeter spatial resolution. And this test used optical frequency domain reflectometry (OFDR) based technique to complete the DTS and DSS jobs. With OFDR, a tunable laser is swept through an optical frequency range, generating interference fringe data that is collected and analyzed with an interferometer-based system, producing a record of reflection events observed as a function of the optical time delay which occurs when light propagates from the instrument to the reflection event and back.

Test setup

The steel tubing sample (shown in Figure A-9) is 120 inches long with an inner diameter of 4.25 inches and an outer diameter of 4.5 inches. Before the test, caps were weld to seal the tubing at both ends. Valves, pressure transmitters and pressure gauges were installed on both ends to control the pressure.

As Figure A-10 shows, fiber optic cables were installed at 4 locations of the tubing: crown, invert, and spring lines. The tubing was completely polished before cable attachment. The NanZee strain cables were first attached to the tubing with 3M Scotch-Weld DP8010 amber two-part methacrylate adhesive. And then the Belden temperature cables were attached to the tubing (next to the strain cables) with duct tapes. The LUNA ODISI 6000 Series Interrogator was used to measure the real-time data with 2 channels.

The tubing was ground in the middle to simulate the actual corrosion area. To find out how the corrosion area affect the detecting performance, different grinding areas with different

depths were tested (shown in Table A-1). And for each case, 2 cycles of pressurization and depressurization were done with an interval of 30 minutes.

Nitrogen was used to pressurize the tubing. During the pressurization stage, the pressure was increased by 100 psi at each step and held for 1 minute. Then the next step was started. During the depressurization stage, the pressure was decreased by 400 psi at each step and held for 30 seconds. Then the next step was started until reaching 0 pressure finally.

Figure A-9: test setup overview



Figure A-10: Cable layout

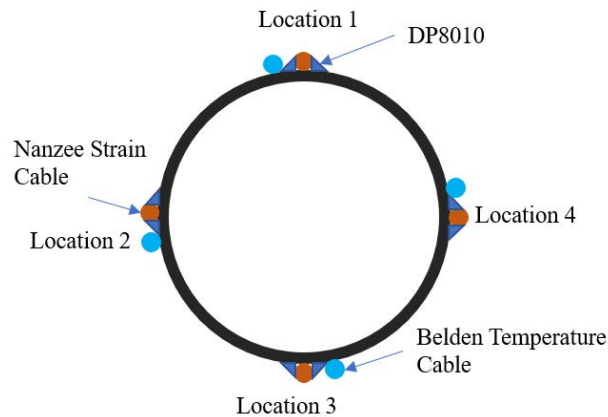


Table A-1: Different testing cases for the experiment

| Case | Grinding Area (inch by inch) | Grinding Depth (inch) | Peak Pressure (psi) |
|------|------------------------------|-----------------------|---------------------|
| 1 | 0 | 0 | 1600 |
| 2 | 2 * 1 | 1/16 | 1600 |
| 3 | 2 * 1 | 1/8 | 1600 |
| 4 | 2 * 2 | 1/8 | 1600 |
| 5 | 2 * 2 | 3/16 | 1600 |
| 6 | 2 * 2 | 3/16 | 2300 |

Results

The measured axial strain results using DFOS after temperature compensation and baseline correction are as Figure A-11. All the results are at peak pressure. The X-axis is the length of the cable (unit in foot). The Y-axis is the axial strain of the tubing (unit in $\mu\epsilon$).

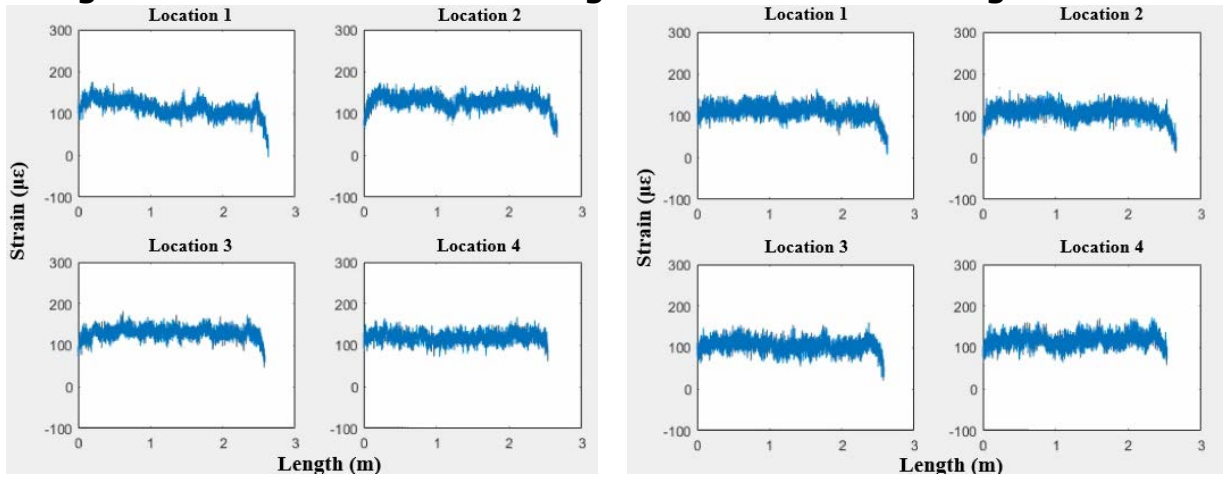
For the first few cases where the grinding area and depth were small, the strain difference is not obvious (about 10-20 $\mu\epsilon$). As the grinding area and depth increases, the strain difference becomes larger around the grinding area and finally reaches to about 50-60 $\mu\epsilon$. And this difference is clearer at cable location 1 and 2, where the grinding area was in between.

It is worth noting that the strain measured at two spring lines are similar to each other, but there's a difference for that at crown and at invert. This may be due to the way of placing the tubing. It was placed on two steel stands and addition wedges were inserted underneath. Therefore, additional forces from the stands and wedges generated could cause this bending behavior.

Implication

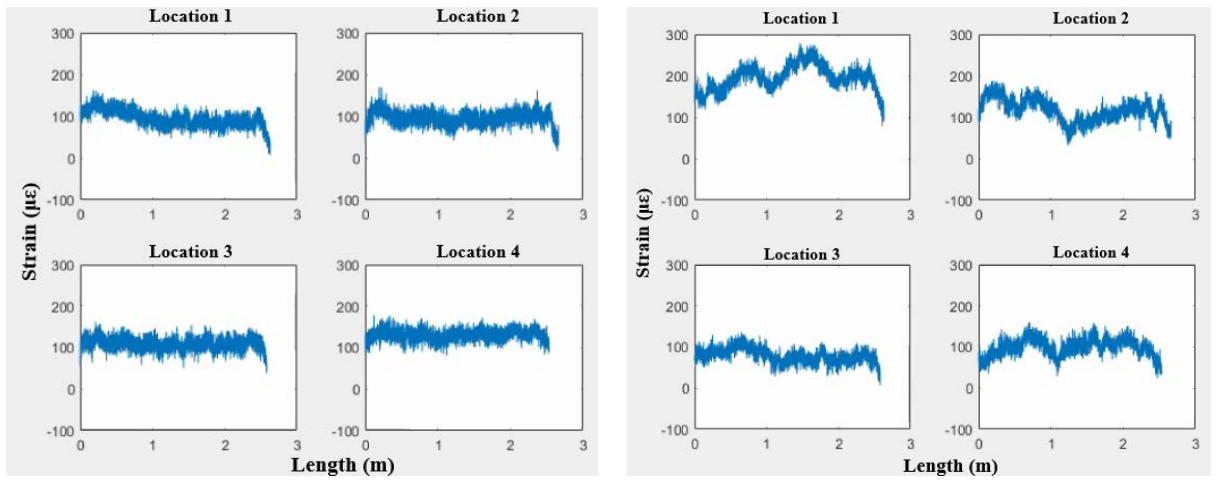
This result indicates that DFOS can be a potential way of monitoring the oil and gas wells to detect if a corrosion happens on the inner tubing or outer casing. Traditional sensors can only assist in judging whether there is potential corrosion around their installation locations. With distributed optical fiber, any position can be analyzed. But to achieve an accurate monitoring result, there are certain requirements for the layout of the cables. In order to better capture the temperature changes caused by pressure changes, the temperature fiber needs to be close to the tubing wall and firmly connected. Considering that the potential corrosion area may be very small, the increase in the number of cables in the circumferential direction will be more conducive to detecting the corrosion area. In addition, this test result shows that the contact between the two supports and the tubing greatly affects the strain results. Therefore, the monitored strain results cannot be used as the only criterion for the occurrence of corrosion.

Figure A-11: Axial Strain of Tubing at 4 Locations under High Pressure



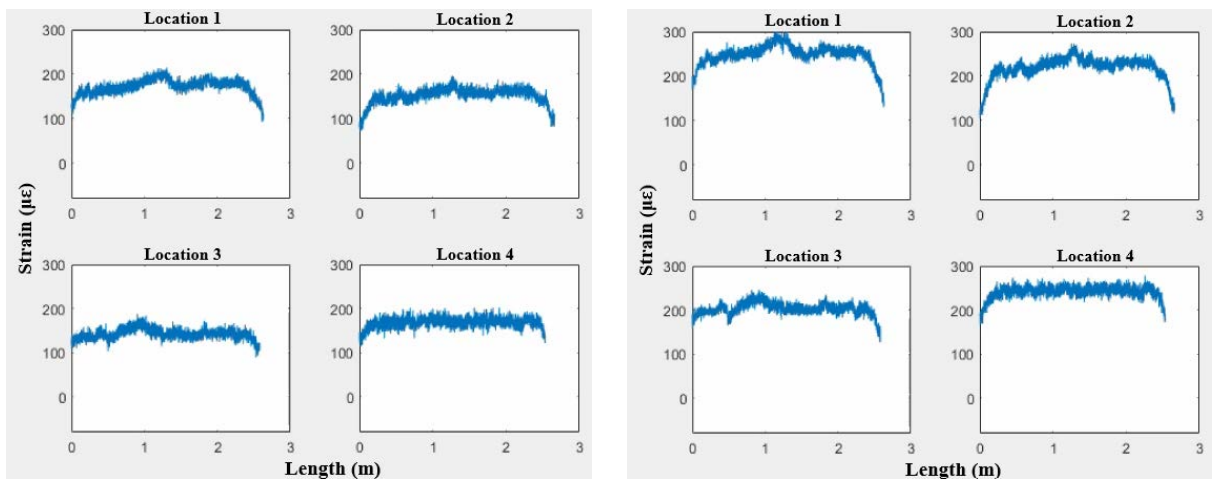
a) Measured results of Case 1

b) Measured results of Case 2



c) Measured results of Case 3

d) Measured results of Case 4



e) Measured results of Case 5

f) Measured results of Case 6

Detection of Water Table Depth using P-Wave Refraction with Geophones and Distributed Acoustic Sensing

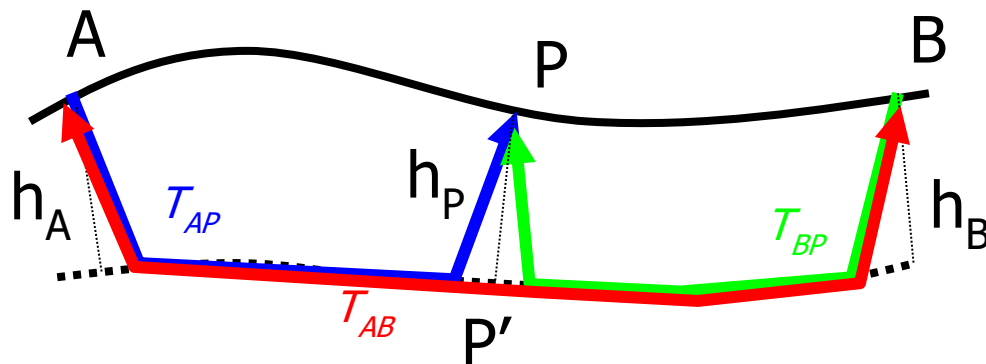
Introduction

Pressure wave (p-wave) refraction is a technique for imaging the subsurface based on abrupt changes in the P-wave velocity profile. Due to Snell's Law, p-waves propagating through a low velocity material into a material with higher velocity will refract. Rays that intersect with the higher velocity material at the critical angle (i_c) are refracted along the boundary between the two materials. Huygen's principle states that wavefronts may be represented as a summation of new energy sources (p-wave in this case) along the wavefront. Because of this principle, the critically refracted ray returns to the surface as what is known as a head wave. Detecting both the head wave and the direct arrival of p-waves traveling in the surface medium makes the p-wave refraction method possible.

Since many geologic settings are comprised of a highly weathered, unsaturated (soil) layer at the surface underlain by a saturated zone of the same or similar material, the direct arrival and refraction of p-waves off the top of the saturated zone make deducing the depth of the water table possible (Dugid, 1968; Wallace, 1970; Haeni, 1986; Desper et al., 2015).

The specific method employed in this chapter is called the reciprocal method. The reciprocal method uses several (three or more) refractions at different positions to resolve varying water table depth with changing topography. Figure A-12 shows this method using three different shot positions on an undulating terrain with varying refractor (watertable depth).

Figure A-12: Schematic of p-wave refraction reciprocal method (Geometrics, 2021)



Using this method, the p-waves travel time from A to B (T_{AB}), A to P (T_{AP}) and B to P (T_{BP}) can be used to estimate the depth at position P. The sum of T_{AP} and T_{BP} minus T_{AB} is proportional to the depth at position P. This method was used with the seismograph data to estimate the water table depth at the test site and then compared with the data obtained using distributed acoustic sensing (DAS).

Objective

In this field test, it was desired to estimate the depth of the water table with the p-wave refraction technique using seismographs, which is a standard technique. Measurements made with the seismographs were then compared with measurements made using a buried fiber optic cable being interrogated with a technique called distributed acoustic sensing (DAS).

The data acquisition using geophones and analysis is a commercial offering of Geometrics Inc. It is desired to see if a comparable process can be conducted using DAS because a buried fiber optic cable can easily be installed at sites that will be repeatedly surveyed for their water table depth. The cost of fiber optic cable is very low (<\$5/m), and installation can be conducted in conjunction with construction of an asset such as a pipeline.

Technology

Distributed acoustic sensing (DAS) is a technology within the large family of distributed fiber optic sensing technologies. DAS uses the natural Rayleigh scattering of light within an optical fiber to make a distributed interferometer. Light from separate scattering locations within a fiber are combined and the light phase difference is calculated. This difference in light phase changes proportionally to external strain on the fiber. The distance between the scattering locations is called the gauge length. The gauge length plays an important role in determining what wavelengths of seismic signals can be detected with DAS. In this field test, an Optasense Inc. ODH-4 DAS interrogator unit was used with an acquisition rate of 10kHz and a cable length of 100m. The optical phase measurements are reported every 1m along the cable length

Geometrics Atom seismographs were used for comparison with the DAS array since they are a commercial and widely accepted sensor for the p-wave refraction technique.

Test setup

A field test was conducted at the UC Berkeley Center for Smart Infrastructure (CSI) to compare geophones with DAS for locating the water table using p-wave refraction. 100m of tightly buffered fiber optic cable were installed within a trench and then backfilled 8cm deep. The Atom seismographs were then placed on the ground surface above the trenched cable at a spacing of 2m. A sledgehammer was then used as an active source to create p-wave energy. The hammer was used to strike the strike plate vertically all along the array of DAS and seismographs at intervals of 5m. For brevity, only the strikes at 3, 47 and 95 m along the array are used for the p-wave refraction technique. The test setup is shown in

Figure A-13.

Figure A-13: P-wave Refraction Test Configuration



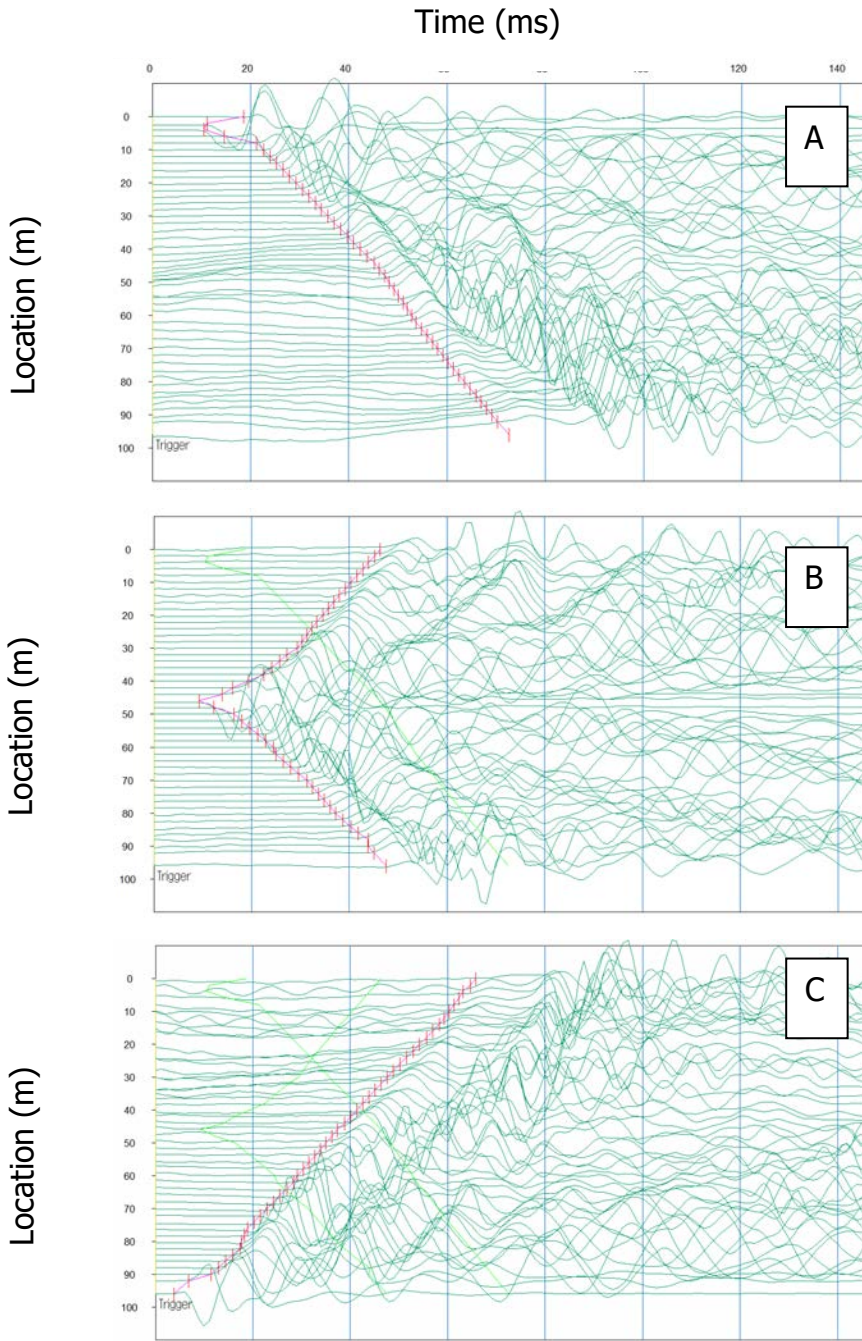
Results using Atom seismographs

The seismograph data was processed using Geometrics Seisimager™ software. The direct and refracted p-wave arrivals are selected from the data as first arrivals. Automatically picking the first arrivals is possible within the Seisimager software, and the resulting data and first arrival picks are shown in

Figure A-14 for the shots created at 3m, 47m and 95m along the array. For each shot location five sledgehammer strikes were stacked to improve the signal to noise ratio. Each shot location produces a travel time curve of the first arrival. The travel time curves for the test site generated from the three shot locations are shown in

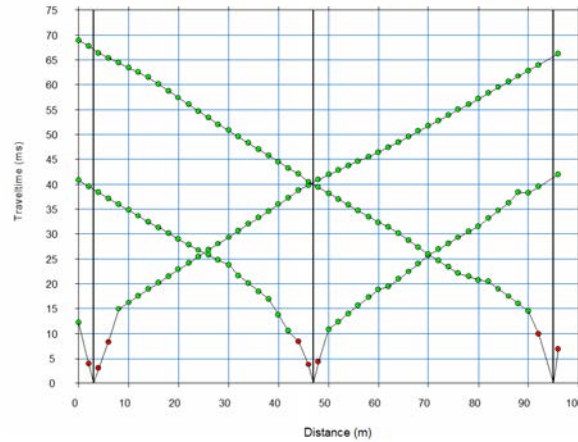
Figure A-15.

Figure A-14: Atom Seismograph Data and First Arrival Picks



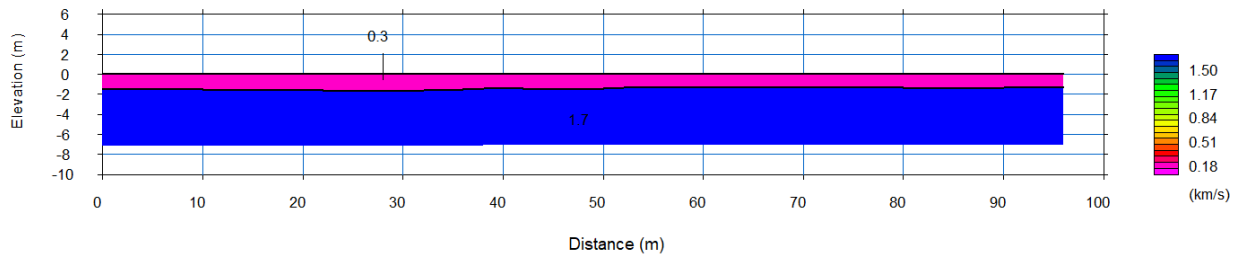
from the shot located at (A) 3m, (B) 47m and (C) 95m along the array, traces are stacks of five sledgehammer strikes

Figure A-15: Travel Time Curves from the 3m, 47m and 95m Shot Locations



Finally, using a reciprocal method analysis procedure of the refracted p-waves, a ground model is generated. The two-layer ground model for the test site is shown in Figure A-16. The p-wave velocity of the near surface (unsaturated) zone is estimated as 300 m/s, while the saturated zone is estimated as 1700 m/s. The analysis indicates that the water table in this location is fairly level, with an average depth of 1.7m below the ground surface.

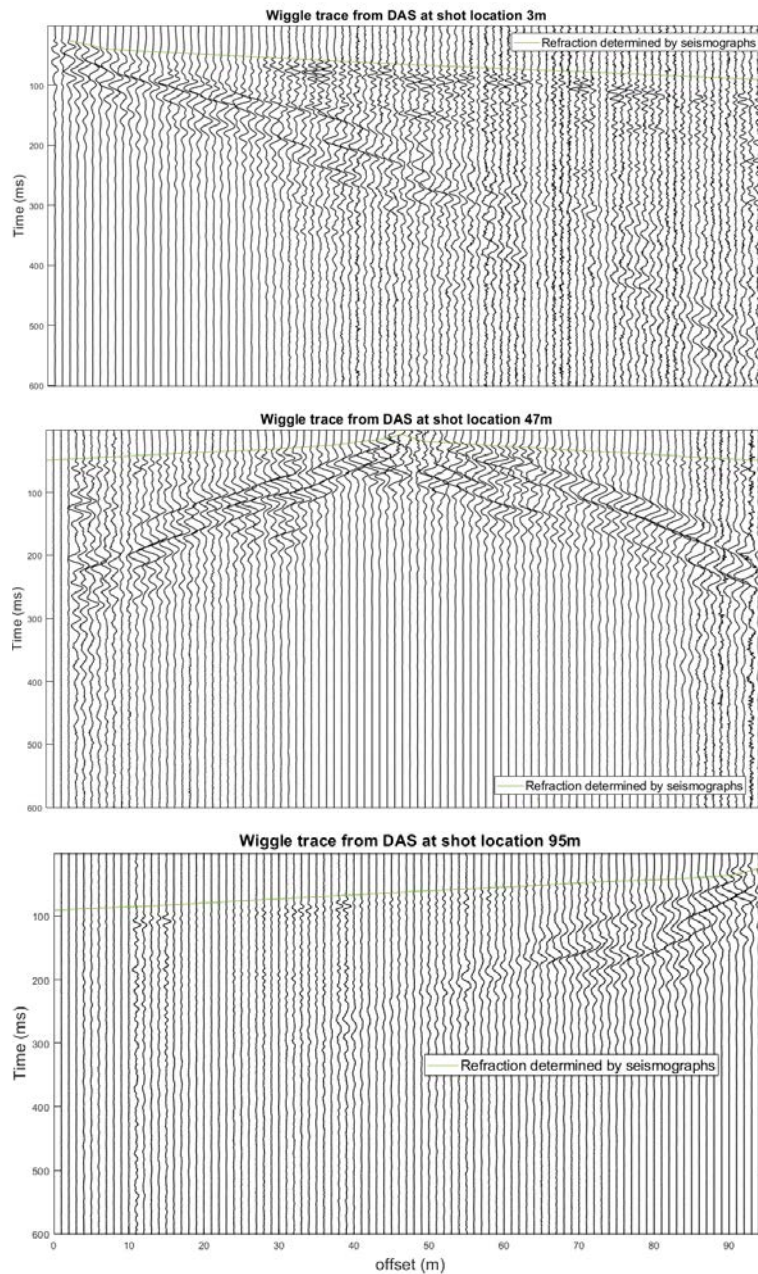
Figure A-16: Two-layer P-wave Velocity Model of the Test Site Using the Reciprocal P-wave Refraction Technique



Comparison of Travel Time Curves to DAS Data

The picked travel times from the Atom seismograph data was compared to the recorded DAS data at the site. The DAS data sampled at 1m spacing and 10kHz is shown with the geophone travel time curves in Figure A-17. As shown in Figure A-17, the refraction of the seismic waves is recorded in the DAS data. The DAS records vibration in the horizontal inline direction, while the seismographs recorded vibration in the vertical direction. This caused the DAS recording to have slightly worse signal to noise ratio than the seismographs, however the refraction is still discernable over the entire 95m array length.

Figure A-17: DAS Data Plotted with the Travel Time Curves of the Arrivals Determined from the Seismograph Data



Implication

P-wave refraction is a potential method for estimating the water table depth in areas where the water table depth is an input for *OpenSRA*. In the case of pipelines, it is possible to bury a fiber optic cable at the time of installation or trench it in later to have a continuous seismic receiver for water table depth monitoring using p-wave refraction. More field-testing using DAS needs to be conducted to validate the technique using different geology and aquifer depth, however this proof of concept is ready to be pilot tested by utility companies using *OpenSRA* to better constrain the water table depth inputs to the risk analyses.

Sensing of Steel Pipeline Deformation using Distributed Strain Sensing

Introduction

This section reports the results of a laboratory test where distributed strain sensing (DSS) was used to instrument a pressurized steel pipeline section subject to four-point bending. The test was in cooperation with Pacific Gas and Electric (PG&E) and Paulsson, Inc. on December 14, 2020 at ADV Integrity in Waller, TX.

Objective

The objective of this bending test was to validate that DSS can be used to monitor pressurized steel pipes during bending and to validate an attachment method for field implementation at one of PG&E's critical natural gas pipeline sites.

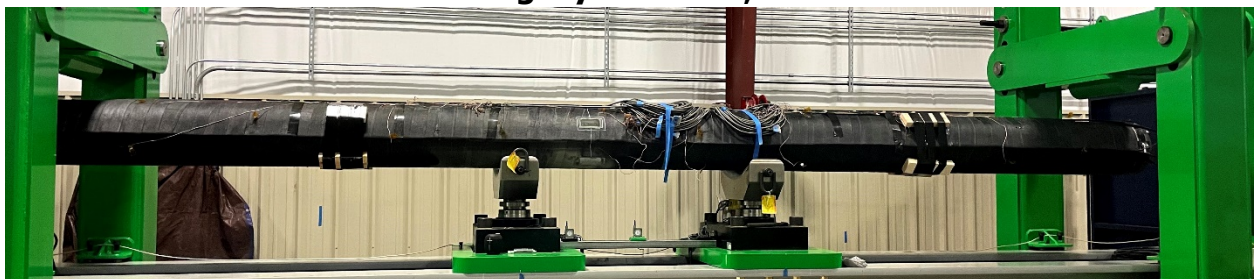
Technology

The technology used was distributed strain sensing using Brillouin optical frequency domain analysis (BOTDA). BOTDA is similar to BOTDR discussed in the previous chapter, with the main difference being that light is sent down both ends of an optical fiber. The counter-propagating light interacts to create stimulated Brillouin scattering. This type of scattering has higher signal strength than the spontaneous scattering that occurs in BOTDR. Thus, BOTDA is associated with better measurement precision. The downfall is that both ends of the sensing fiber must be accessible for measurement. See chapter 3 for more on the fiber optic sensing technologies.

Test setup

The test consisted of a section of pipe made of X52 steel with a nominal size of 1in. The outside diameter was 12.7in. with a wall thickness of 0.188in. The section was 20 ft long and was pressurized to 72% of the specified minimum yield stress (SMYS), 1106 psi. The test apparatus is shown in Figure A-18.

Figure A-18: Pressurized steel pipe specimen before four-point bending at ADV Integrity in Waller, TX



The pipe was instrumented with fiber optic cables that have a tightly bonded internal construction to prevent any internal slippage between the optical fiber core and the outer cable sheath. The specific cable used is the same as the one used in for the HDPE pipe test discussed in the previous chapter. The cable was placed on the pipe using a three-stage

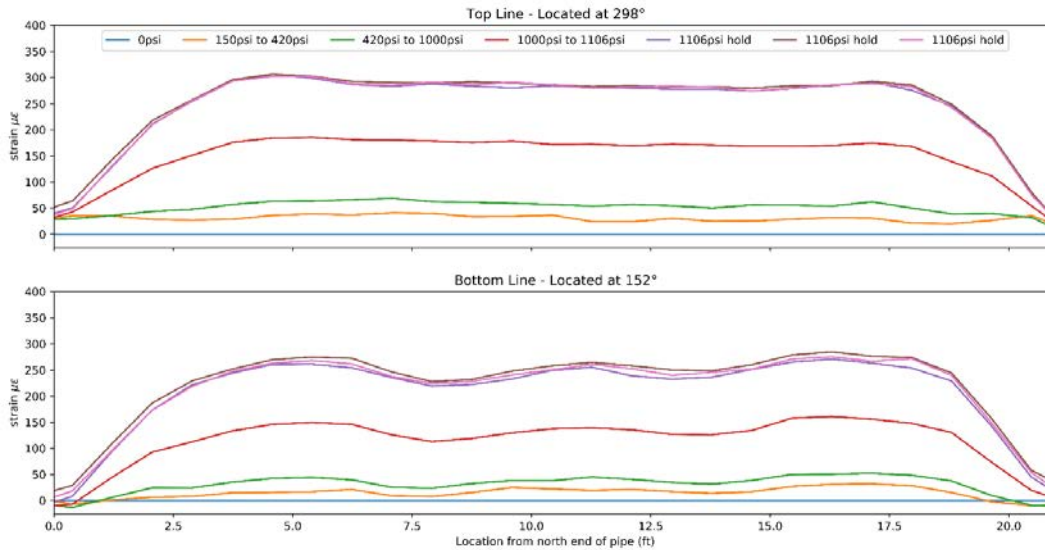
attachment method. First, the cable was directly epoxied to the bare steel using 3M DP8010 epoxy. Next, the cables and pipe were wrapped circumferentially with Trenton WAX-TAPE to help prevent corrosion. Finally, Trenton MCO outer wrap was used to create a hard protective layer on top of the WAX-TAPE. The three-stage attachment method was applied to the pipe and then allowed to cure for 6 weeks, which is recommended for the Trenton MCO outer wrap. The cables were attached at 28° from the springlines of the pipe to accommodate the expected deformation around the vertical actuators and not be pinched during the test, while still measuring bending strain.

The test had two phases. First, the pipe was pressure tested up to 1106psi, where it was held for 15 minutes. After the pressure test, the pipe was bent in a strain-controlled fashion. The strain measured by a vibrating wire strain gauge at the center top of the pipe was used for control. The strain was applied incrementally and held for 20 minutes. The steps were 1000µε, 1500µε, 2000µε, 3000µε, 4000µε, 5000µε, 6000µε, 7000µε, 7500µε, 8000µε, 9000µε, and 10000µε.

Results

The results of the pressurization phase of the test are shown in Figure A-19. As shown, the strain increases in a uniform fashion along the entire length of the pipe as pressure increases.

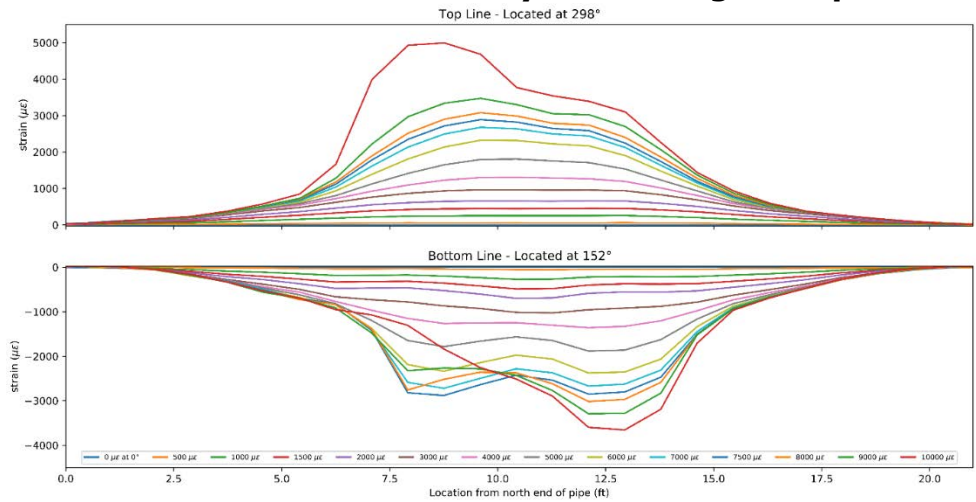
Figure A-19: Strain Measurements Made by DSS During the Pipeline Pressurization Test



The measurements made during the bending test are shown in Figure A-20

Figure A-20. The strain increases with bending in a uniform fashion until it begins to localize on the top of the pipe around the actuator located at 8 ft from the north end of the pipe. On the bottom of the pipe, the strain localizes at the other actuator located 12 ft from the north end of the pipe. This is consistent with the deformation mechanism that was observed.

Figure A-20: Strain Measurements Made by DSS During the Pipeline Bending Test



Implication

It has been demonstrated that DSS can be effectively attached to steel pipelines and monitor strain from both pressurization and bending. The pipeline bending test was a showcase to PG&E, who have now moved forward with a full-scale deployment on a critical large-diameter natural gas pipeline in the bay area, California that crosses an active earthquake fault.

Pipeline Component Laboratory Cyclic Bending Test using Distributed Fiber Optic Sensing

Introduction

This section introduces the demonstration of using Distributed Strain Sensing (DSS) for pipe components monitoring. A series of laboratory cyclic bending experiments of selected pipe components have been carried out by Task Group D. An 8" Tee joint cyclic bending test is selected for the demonstration. The tested pipe Tee joint is shown as Figure A-21. Both the top and bottom ends of vertical section are fixed (right side of the photo). The outlet of the horizontal section which towards east is connected to the actuator through a hinge (left side of the photo). A cyclic load was applied in the horizontal north-south direction on the vertical section of Tee joint by the actuator.

Figure A-21: Experiment setup



Figure A-22 shows the instrumentation of the fiber optical strain sensing cables, whereas Figure A-23 shows a close-up photo of the two different attachments.

Figure A-22: The instrumentation of the DSS sensors (modified from Task D)

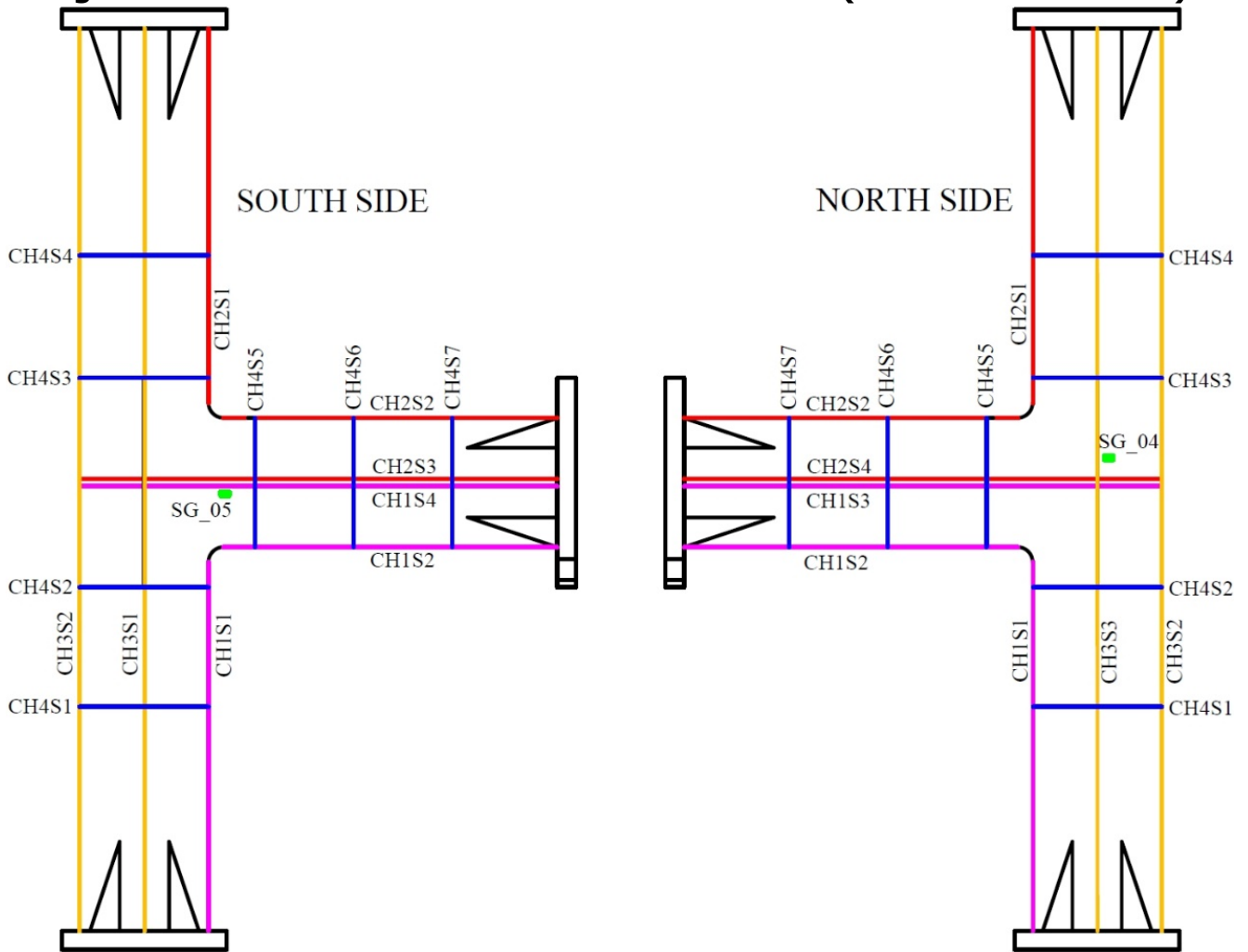


Figure A-23: Close-up photo of attachments



Technology

Four fiber optical strain sensing cables are attached to the specimen, three along the longitudinal directions on each pipe surface to measure the pipe longitudinal bending strain, and one wraps the pipe circumferentially to measure the ovalization of the pipe. A selected four channels short-range high-resolution (OFDR) has been used to measure four strain sensors simultaneously. The strain distributions measured by DSS are compared to the adjacent conventional strain gauges to verify the performance of selected DSS analyzer and sensors.

Rayleigh backscatter-based interrogators measure the strain and temperature distributed along the fiber by comparing the phase or Rayleigh backscatter spectrum (RBS). A Rayleigh-based optical frequency domain reflectometry (OFDR), Luna ODiSI 6100 (Figure A-24) is used in this experiment, which can take measurement every 0.65mm with an accuracy less than $\pm 1\mu\epsilon$ and can measure up to 50m long sensor cable.

Figure A-24: Luna Odisi 6100 High-Definition Fiber Optic Sensing Interrogator



Table A-2 shows the schematics of the selected strain sensing cables tested in this experiment. Both cables are tightly bonded and are able to sense the strain distributed on its protection jacket. The 2mm cable doesn't have metal-reinforcement, which gives a better sensitivity and is good for measuring small strain such as the strain induced by the pipe ovalization. The 5mm metal-reinforced cable is robust and can be used in the field for real application.

Table A-2: Schematic illustration of the selected strain sensing fibers structures (Wu et al., 2015)

| Brand | NanZee Sensing | NanZee Sensing |
|---------------|----------------|----------------|
| Model | NZS-DSS-C07 | NZS-DSS-C02 |
| Cross section | | |
| Side view | | |

Result

As an example, Figure A-25 shows the strain distribution profiles on the north and south sides of the horizontal Tee joint outlet at the 13th load cycle (Line CH1S3/4 and CH2S3/4 in Figure A-22). The distributed strain profiles show significant asymmetry. The maximum strain in compression is founded at 27cm, where is right beneath SG05 (see Figure A-22), close to the expected maximum strain location. However, the maximum strain in tension is founded at 40cm, where is 24cm away from SG04 (see Figure A-22) and 13cm away from the expected maximum strain location.

Figure A-26 show an example of the maximal and minimal strain measured during each loading cycle along Line CH1S3/4 and CH2S3/4. A faster strain development is observed in the compression zone compared to the tension zone. The specimen starts to yield after the 13th load cycle. Figure A-27 shows the maximal strain measured along Line CH1S3/4 and CH2S3/4 versus the displacement of actuator. An obvious plastic deformation is observed at the last four cycles, where the loading amplitudes are greater than ± 4 cm.

This demonstration shows the ability of distributed strain sensing to detect the magnitude and location of the large permanent deformation occurring on the pipeline components induced by cyclic loading.

Figure A-25: Strain distribution profile on north and south sides of the horizontal Tee joint outlet at 1st maximum magnitude of 13th load cycle

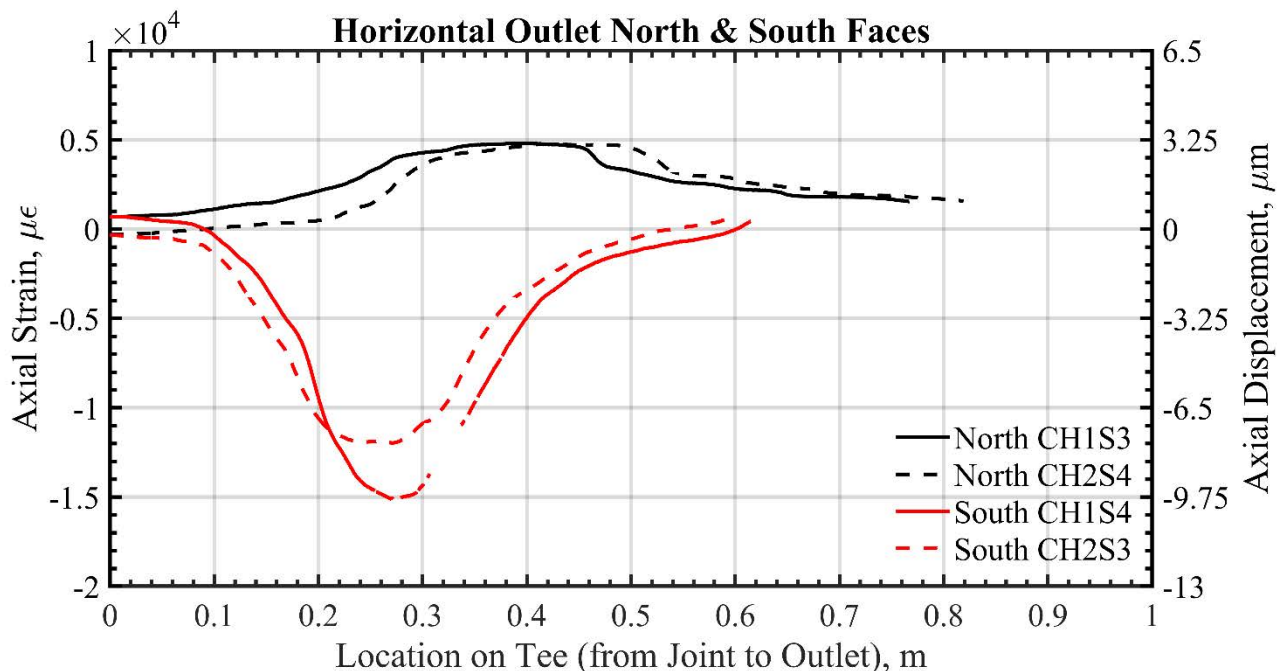


Figure A-26: Maximal and minimal strain measured on north and south sides of horizontal section

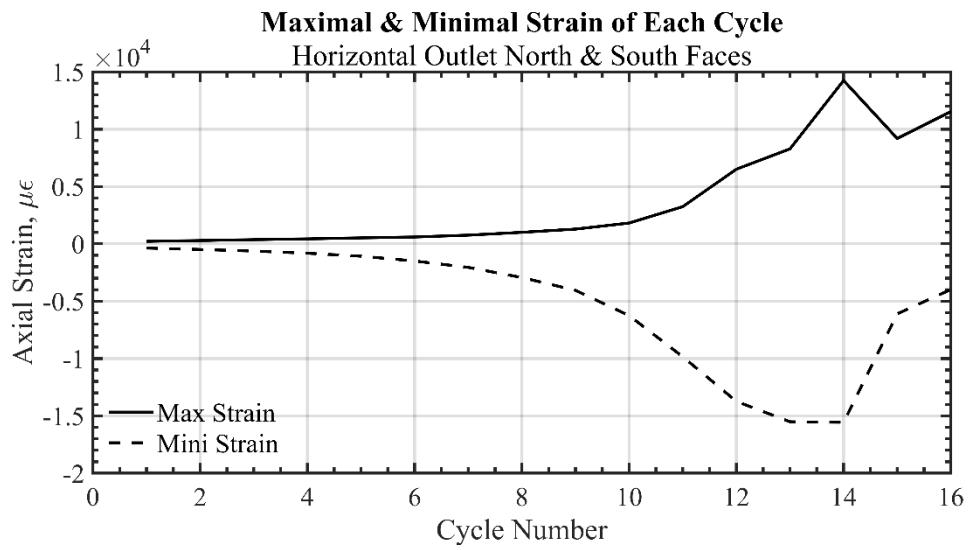
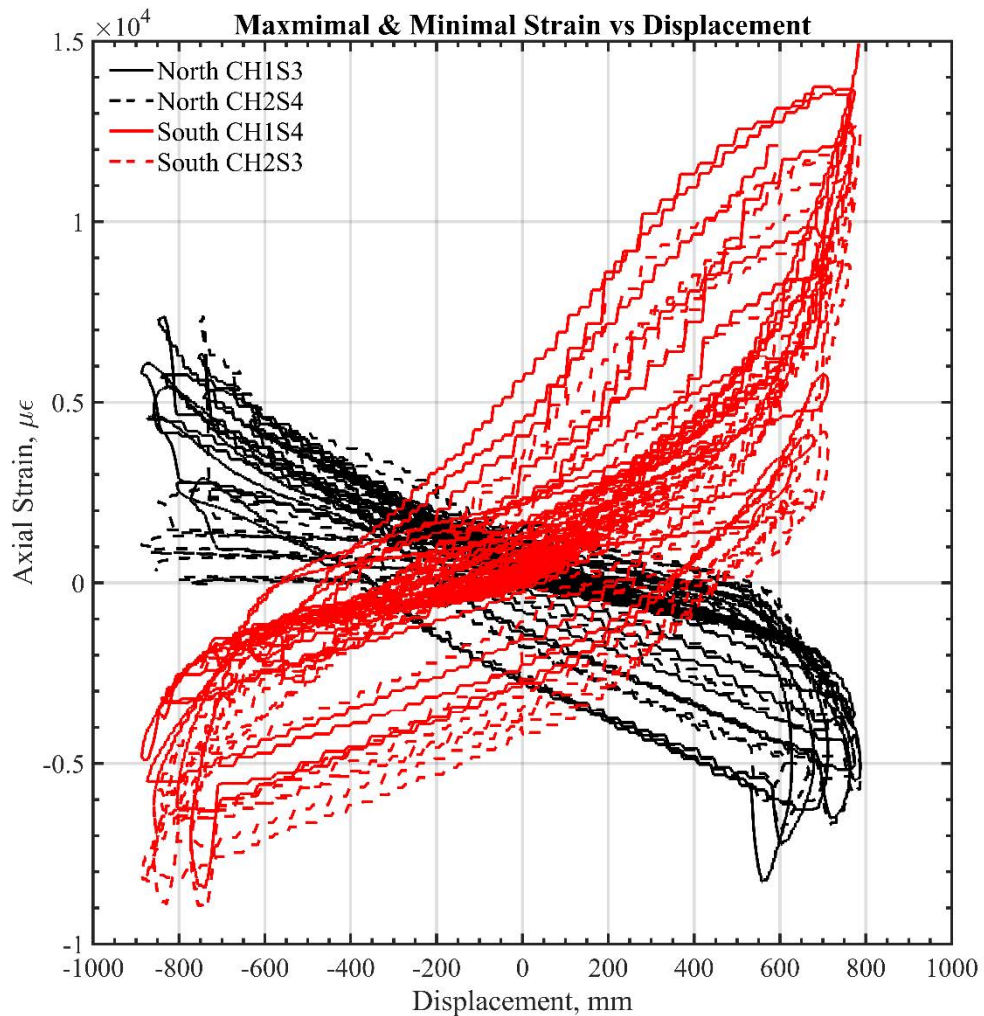


Figure A-27: Maximal and minimal strain versus actuator's displacement



Pipeline Subsystem Laboratory Shaking Table Test using Distributed Fiber Optic Sensing

Introduction

This section introduces a demonstration of using Distributed Strain Sensing (DSS) for pipeline system monitoring. A laboratory shaking table experiment on a pipeline subsystem was carried out by Task Group D. The tested pipeline subsystem was built horizontally on two shaking tables located on west (right) and east (left), as shown in Figure A-28. It includes 4" and 8" pipes, a pigtail connected with a Tee joint and a vertical gas tank connected to the pigtail. The subsystem is connecting with the tables by clamping (not tight) onto five concrete supports that fixed to the tables (two on the left and three on the right). Three 90-degree elbows are fixed to the tables (two 8" on the left and one 4" on the right) and the bottom of the tank. In this experiment, the shaking tables applied relative cyclic displacements in the north-south direction.

Figure A-28: Experiment setup



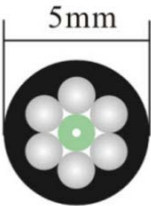
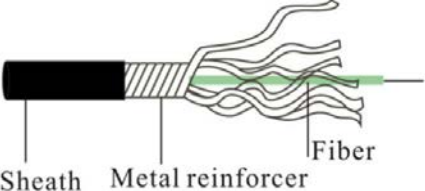
Strain sensing fiber cables were attached onto the pipeline specimen along the longitudinal directions of the pipeline to measure the permanent strain distribution changes after each shaking cycle. A Brillouin Optical Time Domain Reflectometry (BOTDR) based analyzer was used for strain measurements. The specification of the analyzer is given in Table A-3. The distributed strain data was also used for calculating bending curvature and deformation.

NZS-DSS-C02 metal-reinforced strain sensor cable was used in this demonstration. Its schematic and information are given in Table A-4. The fiber is protected by a sheath layer and six metal reinforcement wires. The cable sheath, metal reinforcer and fiber are tightly bonded together, which allows the strain to be transmitted from its surface to the fiber. The protection jacket and metal reinforcement make NanZee 5mm strain sensor cable very robust and can be deployed in the field.

Table A-3: Specification of the demonstrated BOTDR

| | |
|---------------------------|------------------|
| Maximum sensor length | 10 km |
| Spatial resolution | 1 m |
| Minimum readout interval | 2 cm |
| Minimum strain resolution | 20 $\mu\epsilon$ |

Table A-4: Schematic illustration of the selected strain sensor cable (Wu et al., 2015)

| | |
|---------------|--|
| Brand | NanZee Sensing |
| Model | NZS-DSS-C02 |
| Cross section |  |
| Side view |  |

Instrumentation

Figure A-29 shows the instrumentation of the optical fiber strain sensing cable. One 250m long 5mm in diameter strain sensor cable is attached to the specimen by using 3M DP8010 blue epoxy. The cable was attached along the longitudinal directions on both sides of the pipes, elbows and flanges horizontally, both sides of the pigtail vertically and four faces of the tank vertically, as shown in the figure. Figure A-30 shows a close-up photo of the optical fiber strain sensor cable attachment.

Figure A-29: The instrumentation of the DSS sensor (modified from Task D)

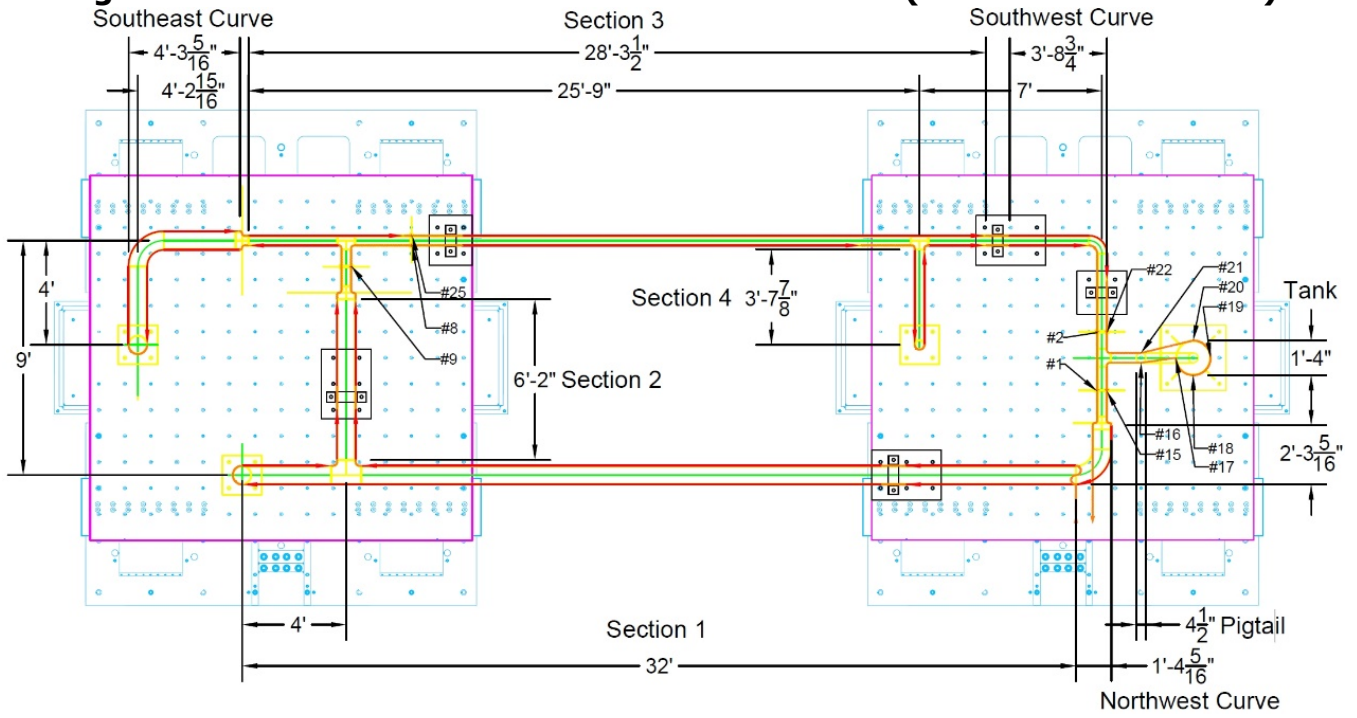


Figure A-30: Close-up photo of attachments

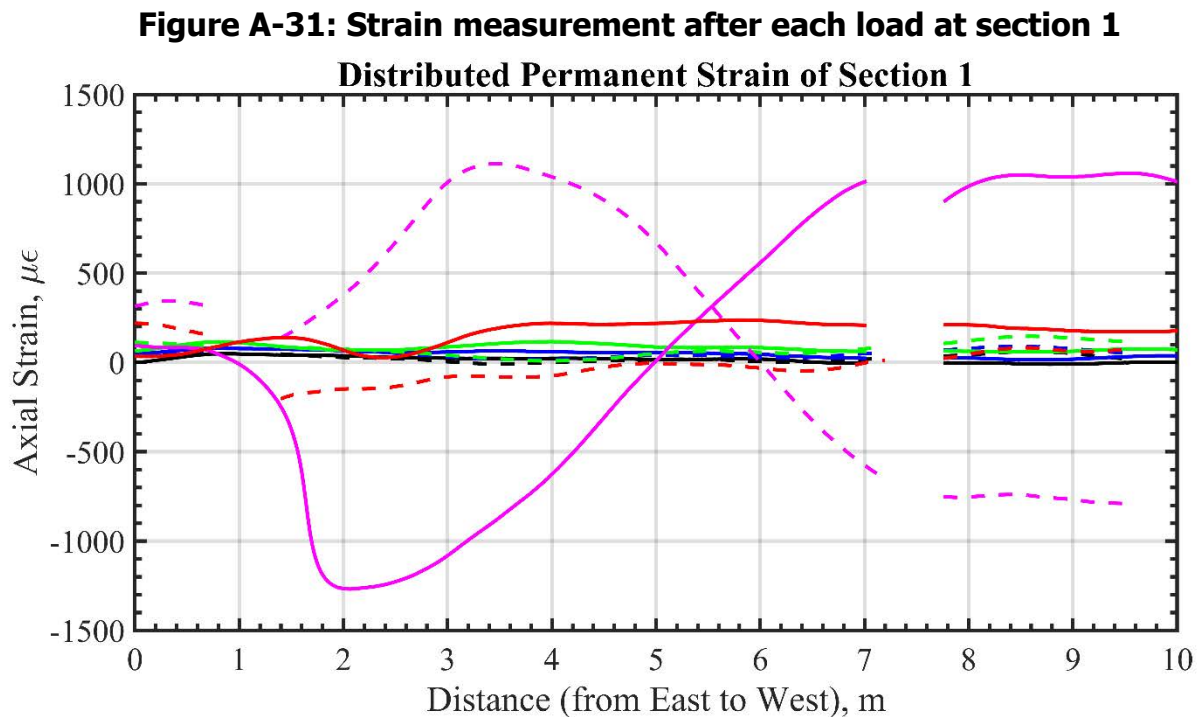


Result

As an example of distributed strain data, Figure A-31 shows the distributed strain profiles measured after load cycles at Section 1. The plots are divided by two at 7.5m where the concrete support located. The sensor cable around the clamp is unattached and its measurement has been removed from the plot. The strain measured at 1m remains zero because of the nearby Tee joint on the south, which is clamped to the concrete pipe support and giving a higher rigidity. The strain measured around 7.5m, where the pipe clamped to the concrete pipe support, remains constant before the 1st 17" motion. But strains develop from the 2nd 17" motion because of the concrete pipe support was damaged during the 1st 17" motion, which was confirmed by an obvious crack. Therefore, the strain measured at that location changed significantly after the 1st 17" motion. Results show that the section bended to north on the east side and to south on the west side.

The lateral displacement induced by the bending can then be calculated by multiplying curvature with the gauge pitch. For example, Figure A-32 shows the estimated accumulation of the lateral displacement of the tank in the north-south direction. The 5" (black plot), 8" (blue plot), 12" (green plot) and 1st 17" (magenta plot) motions gave the same trend and the tank bent to north gradually. A permanent bending at the bottom of the tank was founded after the 1st 17" motion as shown as the shift at the bottom of the plot. The trend of the bending changed after the 2nd 17" (red plot) motion, which bent the tank back to south.

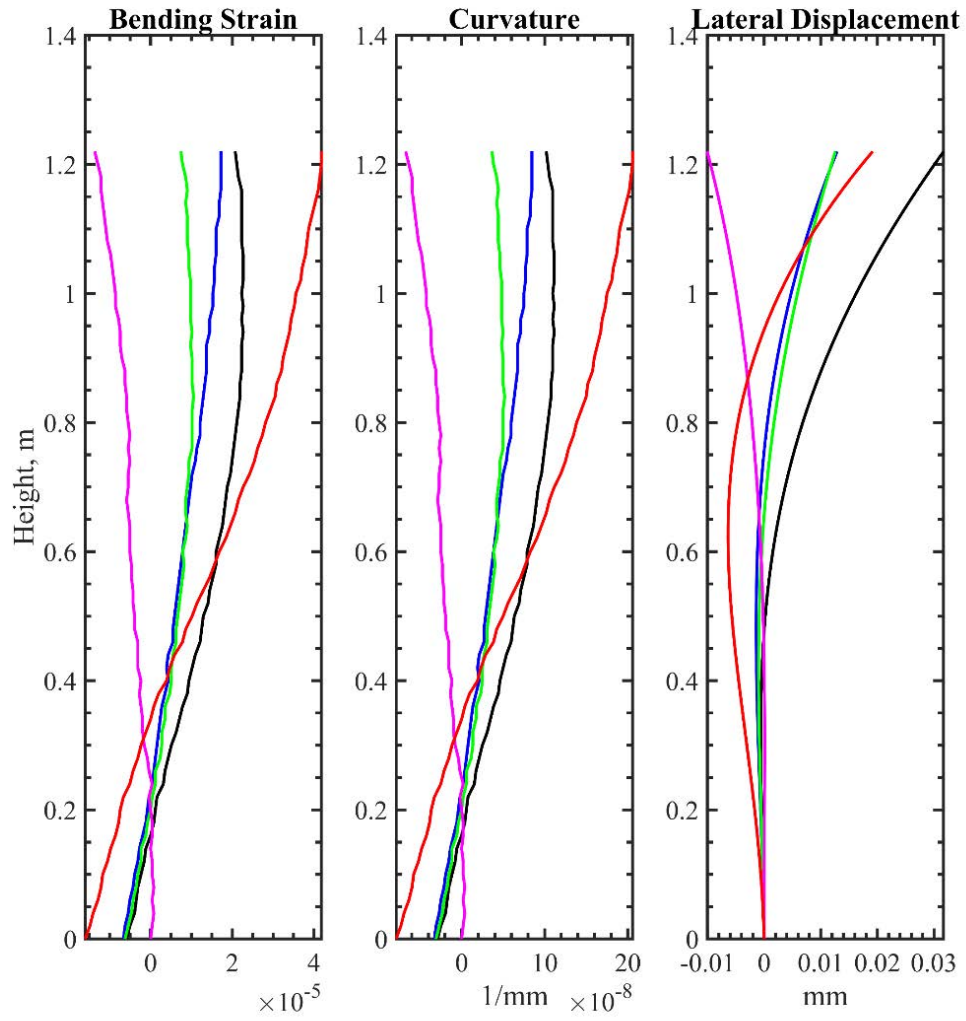
This demonstration shows the ability of DSS system for detecting the pipeline damage induced by a seismic event.



Solid-line: northside; dot-line: southside

Black: after D=5"; blue: after D=8"; green: after D=12"; magenta: after 1st D=17"; red: after 2nd D=17"

Figure A-32: Measured bending of the tank on north-south direction (positive to south)



Black: after D=5"; blue: after D=8"; green: after D=12"; magenta: after 1st D=17"; red: after 2nd D=17"

APPENDIX REFERENCES

- Desper, D. B., Link, C. A., Nelson, P. N., (2015) "Accurate water - table depth estimation using seismic refraction in areas of rapidly varying subsurface conditions," *Near Surface Geophysics*, 13(5), 455-467. doi: 10.3997/1873-0604.2015039
- Duguid, J. O. (1968) "Refraction Determination of Water Table Depth and Alluvium Thickness," *Geophysics*, 33(3):481, doi:10.1190/1.1439945
- Haeni, F. P. (1986) "Application of seismic refraction methods in groundwater modeling studies in new england (USA)," *Geophysics*, 51(2), 236-249. doi:10.1190/1.1442083
- Hubbard, P.G., Luo, L., Yeskoo, A., Soga, K., Araica., K., Cicala, G., Mcleod, M., (2021) "Design of a Distributed Strain Monitoring System for HDPE Water Pipelines Crossing an Earthquake Fault," *Proceedings of the 20th International Plastic Pipes Conference*, Amsterdam, Netherlands.
- Wallace, D. E. (1970) "Some limitations of seismic refraction methods in geohydrological surveys of deep alluvial basins." *Groundwater*, 8(6), 8-13. doi:10.1111/j.1745-6584.1970.tb03675.x
- Wu, J., Jiang, H., Su, J., Shi, B., Jiang, Y., & Gu, K. (2015). Application of distributed fiber optic sensing technique in land subsidence monitoring. *Journal of Civil Structural Health Monitoring*, 5(5), 587-597.